Master's thesis

NTNU
Norwegian University of Science and Technology
Faculty of Natural Sciences
Department of Materials Science and Engineering

Marcus Oskar Heggen Solum

Development of piezoelectric coatings on metal substrates for biomedical applications

The effect of substrate surface texturing on coating properties

Master's thesis in Chemical Engineering and Biotechnology
Supervisor: Julia Glaum
Co-Supervisor: Magnus Rotan
July 2020

NTNU
Norwegian University of
Science and Technology

Marcus Oskar Heggen Solum

Development of piezoelectric coatings on metal substrates for biomedical applications

The effect of substrate surface texturing on coating properties

Master's thesis in Chemical Engineering and Biotechnology
Supervisor: Julia Glaum
Co-Supervisor: Magnus Rotan
July 2020

Norwegian University of Science and Technology
Faculty of Natural Sciences
Department of Materials Science and Engineering

NTNU
Norwegian University of
Science and Technology

Preface

This thesis is prepared for the course TMT4900 - Materials Chemistry and Energy Technology, Master's thesis, at the Norwegian University of Science and Technology (NTNU). The thesis work, performed from January to July 2020, builds on a specialization project carried out by the author in the course TMT4500 from August to December 2019. The supervisor for this work has been Assosciate Professor Julia Glaum, with Dr. Magnus Rotan as co-supervisor.

The experimental work has been carried out at the Department of Materials Science and Engineering (IMA) at NTNU, as well as at NTNU NanoLab. All of the experimental work has been performed by the author, according to rules and regulations at the facilities in question.

As the topic and activities of this Master's thesis to a large degree overlap with the preceding specialization project, major parts of Chapters 1, 2, and 3 have been directly reused from this specialization project, occasionally with some modifications. This will clearly be stated at the beginning of the relevant sections.

The Research Council of Norway is acknowledged for the support to the Norwegian Micro- and Nano-Fabrication Facility, NorFab, project number 245963/F50, which has made it possible to use the NTNU NanoLab for carrying out the entire spin-coating and FIB-imaging procedure in a clean and controlled environment.

Trondheim, 07 July 2020

Marcus Oskar Heggen Solum

Acknowledgements

I would first like to extend my sincere gratitude to my supervisors Julia Glaum and Magnus Rotan for their guidance, feedback and support during this Master's thesis. Especially Magnus' close and detalied guidance in the experimental work has been essential; without him I would probably still be struggling to get started. In addition to my supervisors, I would also like to thank the rest of Julia's students and PhD candidates. The digital meetings we have had twice a week, where both scientific and non-scientific matters have been discussed, have truly helped me keep my sanity during the months of home office and self isolation. I would also like to express my thanks to the members of the Ferro-Bio FACET-group at NTNU, who have given me feedback and help during this semester. Of these, I am especially grateful for the help I have received and the good discussions I have had with Dr. Kara Poon and Dr. Kristine Bakken, on EDS and aqueous chemical solution deposition of barium titanate, respectively. Additionally, I would like to thank all engineers and staff, both in K2 and at the NTNU NanoLab, who have trained me on the laboratory instruments and otherwise helped me during my laboratory work.

An unforeseen challenge during this Master's thesis work has been the outbreak of the CoViD-19 pandemic. Not only prevented this me from accessing the laboratories for 6 weeks, but it has also impacted my everyday life. The risk of physical and psychological decay has been real, and I would therefore like to thank everybody who has taken time off their own writing to go for a walk or to do something fun. Of these, I am especially grateful to two of my regular training-buddies, Signe and Julie, who have dragged me out of the sofa to go for both high-intensity runs or relaxed walks in the city. During our walks, all worries and thoughts – big or small – have been up for discussion, and these conversations have been essential for my well-being.

I would also like to extend a big thanks to my fellow students at the study hall in the fourth floor of K2, with whom I have spent more time than anybody else this past year. Our lunch- and coffee-breaks are always entertaining, and our social gatherings have been an extra motivation to work harder during the weekdays. Finally, I would like to express my deepest gratitude to my friends and family, who have always supported me and pretended to be interested in what I am doing. Thanks to you, the darker days have been less dark, while the happy days have been even happier!

Abstract

The aim of this Master's thesis was to investigate how the surface texturing of Ti6Al4V substrates affected the properties of spin-coated piezoelectric $BaTiO_3$ thin films. This is important from a biomedical point of view, where these coatings can be used to improve the existing bone replacement materials used in for example hip implants. Today, the most commonly used implant materials are based on metals such as stainless steels and titanium alloys. These metals have good mechanical compatibility with the body, and are also inert, with good corrosion and wear properties, which is crucial for their biomedical applications. Despite this, these materials are not bioactive, and are thus unable to cause beneficial interactions between the implant and the body tissue. As a consequence of this, the fixation between the implant and the host bone is not as strong as it should be, resulting in an implant lifetime that is shorter than desired.

This thesis work combines two possible methods that can improve this fixation, namely piezoelectric coatings and textured substrates. Firstly, when coating the metal implants with a piezoelectric material, electrical charges will develop on the implant surface when exposed to a pressure. Such charges are known to interact with the surrounding tissue, encouraging amongst other things bone cell adhesion and growth. In that way, the mechanical properties of the metal can be combined with the functional properties of the piezoelectric coating, while at the same time improving the bone fixation. Secondly, if the implant surface is textured, the bone will be able to grow into these rough features on the surface. This results in a mechanical interlocking between bone and implant, which in turn improves bone fixation. Additionally, it is known that cells prefer to attach to rough features compared to smooth surfaces, providing another method for improved fixation. Thus, if a piezoelectric coating can be applied to a textured metal implant, where the texture is retained even after coating, the bone fixation, and thereby also the quality and lifetime of the implant, can be improved.

In this Master's thesis, aqueous chemical solution deposition and spin-coating was used to deposit $BaTiO_3$ thin films on Ti6Al4V substrates. As cells are known to adhere differently to different structures on different length scales, laser-patterned substrates with a large variation in surface texture, ranging from nanosized laser-induced periodic surface structures (LIPSS) to macroscale grid-patterns, were coated and investigated. Preliminary investigations of polished substrates were made to optimize the temperature treatment of the coating layers, and it was found that heating of each ceramic layer to a maximum temperature of 700 °C in air resulted in the best coating properties. Grazing incidence X-ray diffraction was carried out on the samples, and revealed both a $BaTiO_3$ phase and a rutile phase, which was confirmed upon investigation of electron microscopy images of cross-sections made by a focused ion beam. The same images revealed a good coating adhesion, which might be weakened by the presence of a highly porous oxide-substrate interface region. Additionally, electron microscopy images of the sample surfaces revealed a highly thickness-dependent microstructure, in which the surface texture of the substrates played a crucial role. Finally, dielectric measurements of the samples indicated that the coatings were dielectric, but not ferroelectric, explained by the small crystallite size of the coating layer.

The experimental work was successful in producing coatings with good adhesion that retained the surface texture of the substrate, but more investigations must be done to understand the chemistry and interactions at the coating-substrate interface.

Samandrag

Formålet med denne mastergradsavhandlinga var å undersøke korleis overflateteksturen til Ti6Al4V-substrat påverkar eigenskapane til spinnbelagte, piezoelektiske tynnfilmar av $BaTiO_3$. Dette er viktig frå eit biomedisinsk synspunkt, der desse belegga kan nyttast til å forbetre dei eksisterande beinimplantata som til dømes er nytta i hofter. I dag er desse implantatmateriala ofte basert på metall som rustfrie stål og titanlegeringar. Desse metalla har god mekanisk kompatiblitet med kroppen, og er også inerte, med gode korrosjons- og slitasjeeigenskapar, noko som er viktig for biomedisinsk bruk. Trass i dette, er ikkje dei nytta metalla bioaktive, og kan dermed ikkje skape gunstige interaksjonar mellom implantatet og beinvevet i kroppen. Ein konsekvens av dette er at festet mellom implantatet og beinet vert svakare enn det bør vere, og levetida til implantatet vert såleis kortare enn ønskt.

Denne avhandlinga kombinerer to moglege metodar som kan forbetre dette festet, nemleg piezoelektriske belegg og teksturerte substrat. Dersom eit metallimplantat vert belagt med eit piezoelektrisk material, vil elektriske ladningar opparbeide seg på implantatoverflata under belasting. Desse ladningane vil interagere med celler og vev i nærleiken av overflata, og oppmuntre beinceller til å feste seg til implantatet og vekse. På denne måten kan dei mekaniske eigenskapane til metallet kombinerast med dei funksjonelle eigenskapane til det piezoelektriske belegget, og samtidig forbetre festet mellom bein og implantat. Dersom i tillegg implantatoverflata er teksturert, vil det nye beinet kunne vekse inn i ujamnskapane på overflata, og på denne måten vil det vere vanskelegare å løyse beinet frå implantatet. Ei slik teksturering vil også påverke celler til å binde seg til implantata og gi eit betre feste, då det er kjent at celler heller ønsker å binde seg til rue overflater samanlikna med glatte. Dermed, viss eit piezoelektrisk belegg kan påførast eit implantat med overflatetekstur, der teksturen er intakt sjølv etter belegging, vil festet mellom bein og implantat, og dermed også kvaliteten og levetida til implantatet, forbetrast.

I denne mastergradsavhandlinga vart vassbasert kjemisk løysningsavsetting og spinnbelegging brukt til å avsette tynnfilmar av $BaTiO_3$ på Ti6Al4V-substrat. Då celler bind seg ulikt til ulike strukturar på ulike lengdeskalaar, vart laser-mønstra substrat med store variasjonar i overflatetekstur, frå laser-induserte periodiske overflateteksturar (LIPSS) på nanoskala til makroskopiske rutenettmønster, belagt og undersøkt. Innleiande undersøkingar av polerte substrat vart gjennomført for å optimere temperaturbehandlinga av belegglaga, og det vart funne at varmebehandling av kvart belegglag ved ein maksimumstemperatur på 700 °C i luft resulterte i dei beste beleggeigenskapane. Røntgendiffraksjon med låg innfallsvinkel (GI-XRD) vart gjennomført på dei teksturerte prøvene, og viste at både $BaTiO_3$- og rutilfasar vart danna i løpet av varmebehandlinga. Dette vart stadfesta ved undersøking av elektronmikroskopbilete tatt av tverrsnitt laga ved bruk av ein fokusert elektronstråle (FIB). Dei same bileta viste at adhesjonen mellom belegget og overflata var god, men at denne kunne bli svekka av det porøse området ved grensesjiktet mellom oksidlaget og substratet. Vidare avslørte elektronmikroskopbilete av prøveoverflatene ein mikrostruktur som var svært avhengig av beleggtjukkleiken, som i sin tur var avhengig av overflateteksturen. Til slutt indikerte dielektriske målingar av prøvene at belegga var dielektriske, men ikkje ferroelektriske, då belegglaget bestod av svært små krystallittar.

Det eksperimentelle arbeidet var vellykka i å produsere belegg med god adhesjon, og som bevarte overflatetekstureringa til substratet, men meir detaljerte undersøkingar må utførast for å forstå kjemien og interaksjonane ved grensesjiktet mellom belegg og substrat.

Table of Contents

List of Figures

List of Tables

1 Introduction

As the broad aim and motivation for this Master's thesis overlaps with that of its preceding specialization project [1], Section 1.1 has to a large degree been reused from this project. Furthermore, major parts of Section 1.2 have also been reused, but some changes have been made to emphasize the differences in terms of primary goals and activities.

1.1 Aim and motivation

This Master's thesis is a continuation of a project work carried out during the autumn of 2019 [1]. However, while the project work aimed to develop a reliable route for applying piezoelectric barium titanate ($BaTiO_3$) coatings on Ti6Al4V substrates, to improve the lifetime and quality of current bone replacement materials, the main aims of this master thesis are to refine the coating routine, and ultimately investigate how substrate surface texturing affects the coatability of the substrate. Until now, the common bone replacement materials have typically been based on stainless steels, Co-based alloys, and Ti-based alloys, all of which are strong and corrosion resistant materials. Their applications are varied, and are used in common procedures such as hip joint replacements and dental implants [2]. Despite being so-called biomaterials, meaning that they are designed to direct medical treatment by interacting with components of living systems [3], these materials are not bioactive [4]. This means that the metal implants do not cause any response when brought into contact with biological tissue [5], which in this case means that they do not contribute to new bone tissue formation. As a result, implant-bone-bonding is only achieved by the bone attaching to surface irregularities, which results in a rather weak fixation compared to when the attachment occurs by e.g. bone ingrowth [6]. After several years of stress, during which corrosion and wear also have affected the quality of the implants [7][8], this kind of weak attachment might result in failure of the implant, which then must be replaced. One of the most common ways to prevent this weak attachment is to use bone cements to give the required stability [9]. However, this is an irreversible process, and if the implant needs replacement, all of the cemented parts would have to be cut out. Therefore, by keeping in mind that the amount of elderlies in the world is increasing due to an increasing life expectancy, and that elderlies are especially vulnerable to breaking bones, new kinds of bone implants with improved bone fixation, as well as good corrosion and wear properties, will gain more and more importance in the years to come.

One way to ensure a better fixation, and thus a longer lifetime of the implants, is to improve the implant bioactivity. This can be done by utilizing the fact that it is the implant surface that is in direct contact with the surroundings, and thus, by manipulating the implant surface, the implant bioactivity can be increased. One such surface manipulation could be to deposit a piezoelectric coating on top of the metal implant. When inserted into the body, the piezoelectric coating will be stressed, and surface charges will develop according to the piezoelectric effect. This technique has been shown to have a positive effect on bone growth [10][11], and could result in the desired improvement in fixation. In this way, the lifetime of the implants can be improved, resulting in fewer surgeries and less expenses for patients who need these implants. Research into this topic is therefore important, both for improved health benefits, and from an economical point of view.

1.2 Scope of project

The principle of this Master's thesis builds on the idea of applying a piezoelectric $BaTiO_3$ coating on substrates made of Ti6Al4V, which is an alloy commonly used in bone implants, in order to improve its bioactivity. While an important part of the work is to improve the coating procedure itself, this thesis mainly aims to investigate how different substrate textures affect their coatability. This is of interest because it is known that surface texture significantly influences the bone remodeling cells' preference to bond to surfaces [12][13]. The textured samples investigated in this thesis were made by laser-patterning, and were combinations of grid-structures, with a separation of approximately 100 µm between the grid lines, and nanotextured structures, resulting in a broad range of textures. Additionally, it is known that rough implant surfaces in their own right result in a better fixation [14][15], and it would therefore be favourable to make the implant material surfaces rough. However, a different surface structure will affect the adhesion and wetting properties between coating and substrate, which in turn would affect the overall quality of the implant. Thus, closer investigations into the effect of texturing on the coating procedure are needed, and the results of this Master's thesis might shed some light on this topic.

At elevated temperatures, metals have a tendency to oxidize, resulting in the deterioration of mechanical properties, and a low-temperature deposition method is therefore desired to make the coatings. Thus, spin-coating of a $BaTiO_3$ precursor solution onto Ti6Al4V-substrates with different types of texturing was used to produce the thin films. This method was based on the work of Ræder et al., who successfully produced $BaTiO_3$ thin films on $SrTiO_3$ substrates based on an alcohol-free modified Pechini process [16]. To account for the differences in substrate texturing, the substrates were analyzed in terms of wettability prior to the coating, and in terms of surface texture both prior and after coating. Furthermore, the coated and fired samples were analyzed by Grazing Incidence X-Ray Diffraction (GI-XRD) to investigate if $BaTiO_3$ actually formed, and whether secondary phases were created during the heat treatment as well. These kinds of residual phases affect the properties of the coating, and would have to be investigated closer in terms of their impact on the film quality. In addition to this, the coated samples were analyzed by Focused Ion Beam (FIB) imaging to investigate their surfaces and their coating-substrate interfaces. This made it possible to evaluate the adhesion between coating and substrate, which is essential for the practical application of the coating. Also scratch testing was carried out as a part of determining the coating adhesion, but due to the roughness of the textured samples, this was only done on the polished samples used in the optimization of the heating procedure. After the cross-sections were made, a low-resolution energy-dispersive X-ray spectroscopy (EDS) analysis was carried out, in order to get an overview of the elemental composition at the interface. Finally, the dielectric properties of the coated samples were investigated, as these properties are crucial for improving the implant bioactivity. To broadly summarize the activities that were carried out during this project, a simplified flow-chart of the process is shown in Figure 1.1. It should be noted that nanoindentation and nanoscratching to further assess the adhesion between coating and substrate was planned to do, but the required training and help was not possible to get due to the unforeseen CoViD-19 pandemic, and its corresponding restrictions. Also high-resolution EDS-mapping of the coating-substrate interface in the FIB, to get a better understanding of the interface chemistry, was planned, but once again, the CoViD-19 situation made this impossible to carry out.

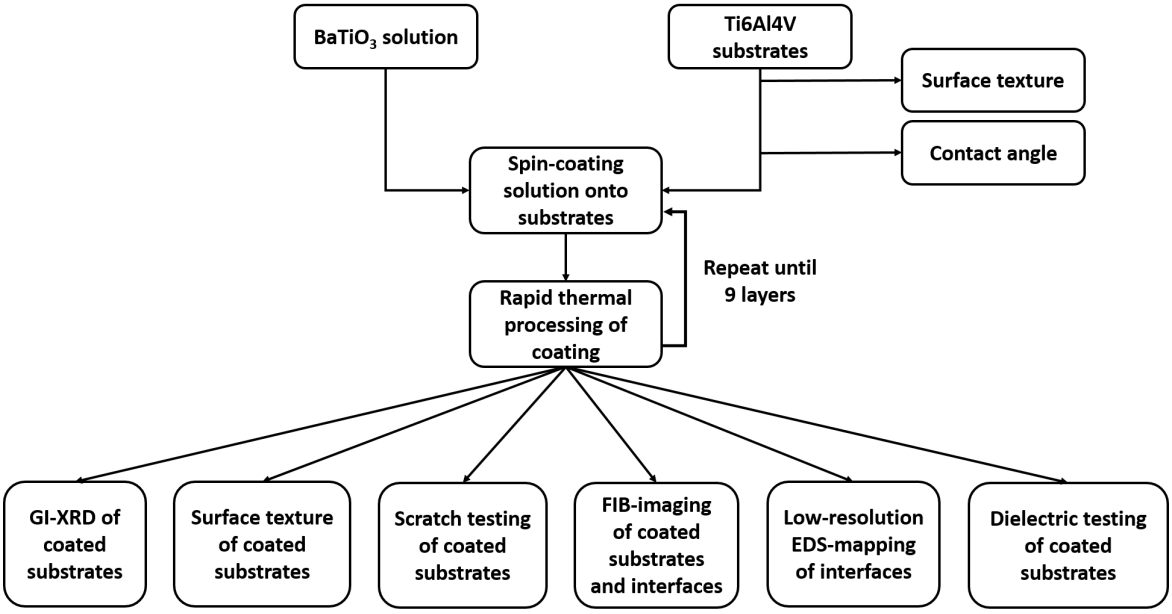

Figure 1.1: Simplified flow-chart for the activities during the project work.

2 Theory

Major parts of this thesis' activities are similar to the activities carried out during its preceding project work, and are covered by much of the same theory. Therefore, large parts of this chapter are directly re-used from the project report [1]. However, some new theory has been added, and some sections have been revised and rewritten. In order to keep track of these changes, Table 2.1 provides an overview of the different sections, and comments on whether they are re-used, rewritten, or entirely new.

Table 2.1: Overview of which parts of Chapter 2 that have been re-used from the preceding project report [1], and which parts that are altered or new.

Section	Comment
2.1.1	Re-used with slight changes
2.1.2	New
2.1.3	Re-used with slight changes
2.2.1	Re-used with slight changes
2.2.2	Re-used with slight changes
2.2.3	Re-used with slight changes
2.3.1	Re-used with slight changes
2.3.2	Revised and partially re-written
2.3.3	Revised and partially re-written
2.4	New, but paragraph on Wenzel type of wetting re-used
2.5	New
2.6	New

2.1 Electromechanical effects

2.1.1 Piezoelectricity in ceramic materials

The direct piezoelectric effect can be described by the development of a surface electric charge, or a polarization, when a mechanical stress is applied to the material in the absence of an electric field. This effect is reversible, meaning that if a voltage is applied to the material, the material will change its shape, giving the inverse piezoelectric effect [17], as shown in Figure 2.1. On a microscopic level, the polarization is a result of internal dipoles, arising when the centers of positive and negative charge within the crystal structure do not overlap, and where the separation of the charge centers changes when a stress is applied to the material. Due to this requirement, the piezoelectric effect is only found in solids with non-centrosymmetric crystal structures [18].

However, when talking about piezoelectric ceramics, the crystal structure requirement is even stricter. A typical ceramic material will have grains oriented in random directions, meaning that the polarization that occurs during stressing also is randomly oriented. Overall, this would result in a net zero total polarization for the material, and a non-observable piezoelectric response. Therefore, to obtain a net macroscopic piezoelectric response, the randomly oriented dipoles have to be aligned somehow. This is only possible for ferroelectric ceramics, where the orientation of polarization can be altered by the

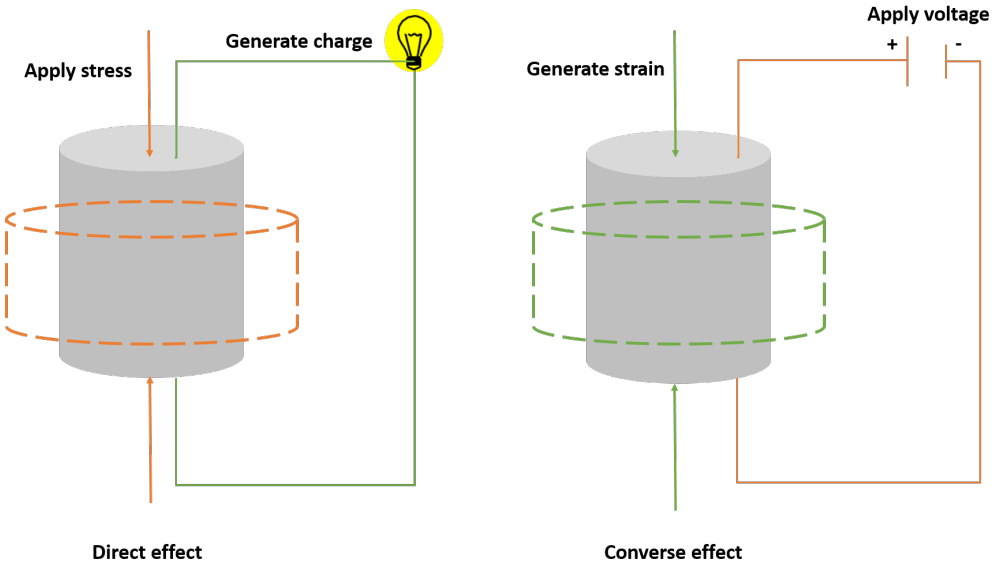

Figure 2.1: An illustration of the direct and converse piezoelectric effects, respectively the generation of power by applying a stress, and the generation of stress by applying a voltage.

application of an electric field, in a process called poling. As a consequence of this added requirement, there are only ten candidate crystallographic point groups for piezoelectric ceramics, where the perovskite structures, due to their versatile crystal structures, seems most promising [11][19][20]. These kind of ABO_3 structures can be described as BO_6 corner-sharing octahedra, with the A-cations in 12-coordinated positions between the octahedra, as shown in Figure 2.2. In a perfectly cubic perovskite, the crystal structure will be centrosymmetric, giving no possibility for piezoelectricity. However, depending on the cation sizes, the crystal structure can be distorted, and the B-site cation will move to an off-centered position. This results in a breaking of inversion symmetry, and the material can now become piezoelectric. By introducing the Goldschmidt tolerance factor,

$$t = \frac{R_A + R_O}{\sqrt{2}(R_B + R_O)}, \tag{2.1}$$

where R_i is the radius of atom i [21], the type of distortion can be predicted. For $t > 1$, the tetragonal distortion is most common, while $t < 1$ usually results in orthorhombic or rhombohedral distortions. However, if t deviates too much from the ideal cubic case where $t = 1$, the crystal structure will no longer be considered a perovskite [19]. This possibility of distorting into so many different crystal structures makes the perovskites extremely versatile. Additionally, because the distortion is dependent on the relative sizes of type A and type B cations, these distorted phases are dependent on the chemical composition of the material. Thus, two phases with different distortions in areas of different composition in a phase diagram can be separated by a compositional phase boundary, typically named a morphotropic phase boundary (MPB). By tuning the composition of the material to be at one of these MPBs, it is possible to exploit the properties of both of the two neighbouring phases, which enhances the piezoelectric properties [19]. Therefore, due to their versatility, the possibility of having several polar axes, and the possible presence of property-enhancing MPBs, the perovskites are amongst the most common good piezoelectric ceramics today.

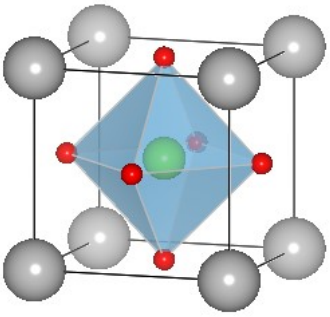

Figure 2.2: The cubic perovskite structure, with A-cations coloured gray, B-cations green, and the oxygen anions are red, based on information from Rödel et al. [19].

The distortions are also temperature dependent, with high temperatures favoring the more symmetric crystal structures. It is therefore useful to define the temperature where the transition from ferroelectric (low symmetry) to paraelectric (high symmetry, centrosymmetric) occurs. This temperature is defined as the Curie temperature, T_c, and is commonly used when discussing whether or not a material shows ferroelectic behaviour at a certain temperature [18]. As a final remark regarding piezo- and ferroelectricity, it is worth noticing that all ferroelectrics are also piezoelectrics, due to their "stricter" crystal structure requirements, while not all piezoelectrics are ferroelectrics. Thus, when talking about "piezoelectric ceramic coatings for biomedical applications", the coatings are actually ferroelectric as well, but it is the piezoelectric effect which is interesting in this case.

2.1.2 Piezoelectricity in organic materials

In addition to the traditional inorganic materials, as described in the previous section, also organic materials can be piezo- and ferroelectric. As early as in 1921, J. Valasek carried out a study of the piezo- and ferroelectric properties of Rochelle salt [22], which is made up of organic tartrate ions, thus being one of the first to establish a direct link between ferroelectricity and organic molecules [23]. Some decades later, in the 1950s, Fukada and Yasuda discovered that bones are piezoelectric [24], stating that the organic collagen molecule was responsible for this effect, and further studies by the same authors on collagen itself [25], confirmed its piezoelectricity. This was explained by the existence of hydrogen bonds in the polypeptide chains of collagen crystals, which make up the collagen polymer. Upon shear stressing, these hydrogen bonds can be displaced or polarized, ultimately causing a piezoelectric effect. Another important breakthrough in the field of organic piezoelectrics was the discovery of piezoelectricity in the synthetic polyvinylidene fluorine (PVDF) polymer by Kawai in the late 1960s [26], which sparked further search for piezo- and ferroelectricity in synthetically produced polymers [27].

The origin of piezo- and ferroelectric properties in organic materials varies greatly from material to material, but three of them will briefly be discussed in the following. The simplest case arises from molecular geometry, where non-centrosymmetric molecules exhibit permanent dipoles, which can be reoriented by the application of an electric field, just as for the inorganic materials discussed previously. This is the most common mechanism for ferroelectric polymers and for single-component low-molecular-mass compounds, such as PVDF and thiourea [23]. A second mechanism resulting in ferroelectric behaviour in

organic molecules is related to protons on hydrogen bonds, where a simultaneous transfer of the protons from one site to another in the hydrogen bond switches the spontaneous polarization of the structure. This mechanism can be found in the inorganic KH_2PO_4-family of materials, but can also be found in several organic materials, among them, squaric acid [23] and collagen, as mentioned above. The third and final mechanism is based on a multi-component donor-acceptor system. In this case an electron donor (D) binds with an electron acceptor (A) in a charge-transfer (CT) complex, which results in an initially non-polar DADADA... sequence, that exhibits no ferroelectric properties. However, being an equally spaced one-dimentional chain, this sequence qualifies for the Peierls' theorem, which says that one-dimentional chains with equal interatomic spacing are unstable [17]. As a consequence, one D and one A pair up into dimers, resulting in a spontaneous and switchable polarization, and thus a ferroelectric material, as shown in Figure 2.3. This is the case for, among others, tetrathiafulvalene (TTF) complexes with p-chloranil [23]. As can be seen, the range of organic ferroelectrics is large, and their applications can be correspondingly large, ranging from non-volatile memory to more environmentally friendly replacements of lead-containing piezo- and ferroelectrics [23].

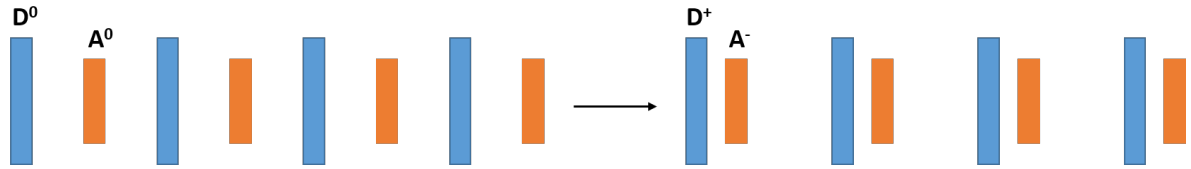

Figure 2.3: Peierls distortion for Donor (D) - Acceptor (A) chain: The equally spaced non-polar chain is distorted into D-A-dimers, and gains a net polarization.

2.1.3 Electromechanical effects in bone

In the late 1800s, J. Wolff stated that the bone remodeling process is strongly influenced by mechanical stress, and that the architecture and structure of the new bone therefore would vary depending on these stresses [28]. The mechanism for this is still not fully understood, but one suggestion that has gotten a lot of attention is the process of mechanotransduction, in which a biophysical force is converted into a cellular response [29]. For this to happen, there must be some mechanisms or signals which "inform" the bone cells that a mechanical stress has been applied. Once again, these mechanisms are not fully understood, but electromechanical effects such as streaming electric potentials and piezoelectricity have been used as explanations [11][29][30]. In the following, these effects will briefly be discussed, in relation to bone.

As mentioned in the previous sections, where piezoelectric effects in ceramics and organics were discussed, the piezoelectric properties of bone were discovered already in the 1950s [24]. This was explained by the displacement of hydrogen bonds in the collagen protein polymer in the bone [25] during shear stressing, and the resulting polarization of the hydrogen bonds leads to the development of surface charges. It is known that cells respond differently in the presence of surface charges compared to an uncharged surface [10][11], implying that cells can be used to sense the changes in surface charge, which was developed by the application of a mechanical force. Thus, a link between an applied force and a cellular response has been established, thereby explaining why the piezoelectric effect is important

for mechanotransduction.

The second electromechanical effect to be discussed is the streaming electric potential, which is an electrokinetic effect that arises when a polar fluid flows by a charged surface [31]. In the context of bones, the polar fluid is the water that is present in the bone, which flows through the channels in the somewhat porous bone structures. When the bone is mechanically loaded, it will slightly change its shape, thus giving pressure gradients in the water in the bone. To counteract these pressure gradients, the water will start flowing from areas with high pressure to areas with a lower pressure, and the resulting electrical potentials can now directly interact with the bone cells [29][30]. Once again, a connection between mechanical loading and bone cells has been established, by the streaming electrical potential acting as a signal.

As mentioned previously, the typical bone implant materials today are made of metals or metal alloys. Due to the nature of these metals, they do not exhibit the piezoelectric effect, neither do they have porous channels with charged walls that allow for streaming electric potentials to develop. This removes the coupling between applied load and cell response, which means that mechanotransduction is impossible, leaving the metal implants bioinert. However, this coupling between applied load and cell response can be solved by applying a piezoelectric coating onto the metal substrate. Now, when the metal implant is loaded and slightly deformed, the piezoelectric coating will be deformed correspondingly, thus developing charges on the implant surface for the bone cells to detect.

2.2 Materials

How easily one material can be deposited onto another is highly dependent on the materials in question. Therefore, the following sections concern the materials used in this project, namely $BaTiO_3$ and Ti6Al4V, and how they relate to the properties of the bone they wish to replace.

2.2.1 The structure of bone

When choosing materials for bone replacement implants, it is important that the properties of the implant matches those of bone. Therefore, before looking into these materials, it is useful to firstly look closer into the structure of bone itself. On a general level, bone can be described as a composite of inorganic hydroxyapatite in an organic collagen matrix, with water present [11][32]. The bone can form two different kind of structures: Compact bone (also known as cortical bone), which is dense and makes up the outer parts of the bone, and cancellous bone, which is a spongy 3D-network. This cancellous bone forms the bone core, and its porous structure allows for blood supply to the bone [11]. Of these types, it is the compact bone that is load bearing, having significantly higher values for both compressive strength and Young's modulus compared to the cancellous bone [33].

During a human lifetime, the bone is constantly remodeling its shape and structure to ensure sufficient strength. In this process, dead or defect cells are removed, and new cells are formed to replace the old. This is done by four different types of bone cells, namely osteoclasts, osteoblasts, osteocytes, and bone-lining cells [11], all of which have different functions. Firstly, the bone-lining cells bond to the surfaces of bones not to be remodelled.

The osteocasts dig out tunnels in the exposed bones, which then are refilled with new bone material by the osteoblasts. These osteoblasts are subsequently turned into osteocytes when they have been embedded into the bone composite [11][32], as shown in Figure 2.4. Thus, to improve the bone growth, these cells must somehow be stimulated and "encouraged" to become more active, and, as described in Section 2.1.3, piezoelectricity and streaming potentials are important factors for this encouragement.

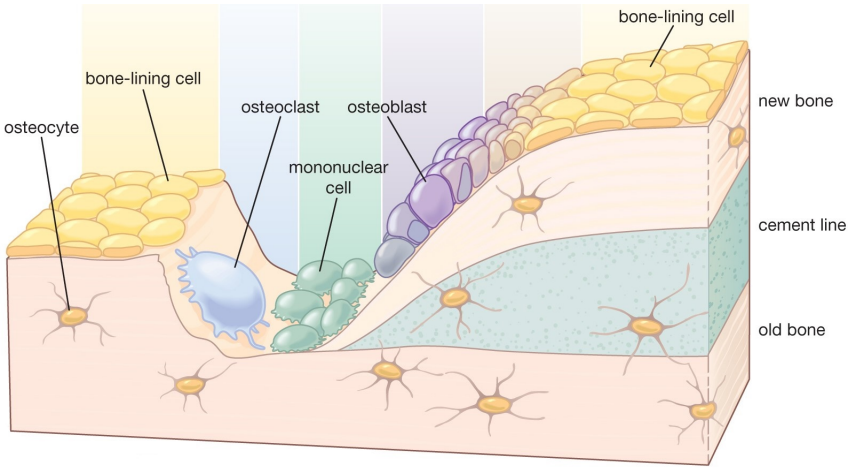

Figure 2.4: The cells involved in the bone remodelling process. By courtesy of Encyclopædia Britannica, Inc., Copyright ©2013; used with permission [34].

2.2.2 Ti6Al4V

Over the last decades, titanium alloys have seen an increase in use as bone implant materials. This is mainly due to their good biocompatibility and corrosion resistance, especially compared to the traditionally used stainless steels and Co-alloys. Additionally, when examining the compressive strength values in Table 2.2, it can be seen that conventional Ti-alloys have a higher strength than bone. This means that the Ti-alloys have sufficient strength to withstand the mechanical forces that arise during use as an implant in the body [35][36], thus making biocompatible Ti-alloys good base materials for this kind of use. However, as mentioned earlier, the metal implants loose some of their properties over time. Both wear and corrosion will eventually cause the metals to break apart [7][8], which in turn might cause local inflammations and possibly implant detachment. Thus, surface treatment of these surfaces is crucial to improve their quality, both to reduce corrosion and wear, but also to improve the bioactivity [37].

Table 2.2: Compressive strength and Young's modulus for Ti6Al4V compared to bone.

Material	σ_c [MPa]	E [GPa]
Ti6Al4V	848-1080 [38]	110 [39]
Ti6Al4V (66 % porous)	116 [40]	2.5 [40]
Compact bone	100-230 [33]	7-30 [33]
Cancellous bone	2-12 [33]	0.005-0.5 [33]

One of the main drawbacks when it comes to conventional Ti6Al4V as a bone replacement material is the large mismatch in Young's modulus between natural bone and the metal, as

can be seen in Table 2.2. As a result, the bone is insufficiently loaded and becomes stress shielded, which can lead to bone resorption and eventual loosening of the implant [40]. Therefore, a lot of research is currently conducted on lowering the Young's modulus of the Ti6Al4V alloy. As the elastic modulus is decreasing with increasing amount of porosity [41], a possible solution would be to make porous metal implants. This would at the same time allow for better fixation between the implant and the bone, due to the bone being able to grow into the implant pores. An interesting way of improving current implants could therefore be coating porous metal substrates with a piezoelectric material, to get the benefits from both of these methods.

2.2.3 Barium titanate

Barium titanate, $BaTiO_3$ (BT), has a perovskite structure as shown in Figure 2.5, where the high-temperature phase is a cubic perovskite with space group $Pm\bar{3}m$, and the lower-temperature phase is a tetragonal perovskite with space group P4mm [42][43]. This means that BT is non-centrosymmetric, and thus ferroelectric, at temperatures below the phase transition temperature, while the material is centrosymmetric and paraelectric at elevated temperatures. The Curie temperature of BT is reported to be in the range of T_c = 115-130 °C [18][44][45], which makes BT ferroelectric at body temperature. This allows BT to be used as a piezoelectric coating for biomedical applications, at least from a purely functional point of view.

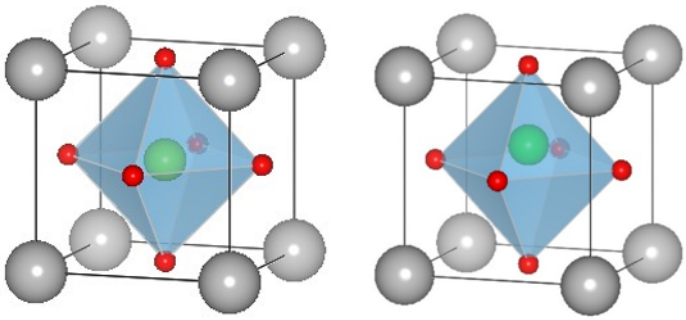

Figure 2.5: The crystal structure of a) cubic, centrosymmetric with space group $Pm\bar{3}m$ and b) tetragonal, non-centrosymmetric with space group P4mm $BaTiO_3$, where grey spheres represent Ba-cations, green spheres represent Ti-cations, and red spheres represent O-anions, based on information from Acosta et al. [43]. Note that the displacement of the Ti-cation in the tetragonal case is exaggerated, to emphasize the phase transition.

After the piezoelectricity of bone was discovered in the 1950s [24], several studies have been carried out regarding the possibility of using a piezoelectric material, such as BT, to improve the bone growth. *In vitro* studies of composites of up to 90 % BT with hydroxyapatite have shown an enhanced cell attachment, while at the same time being biocompatible [46], meaning that they can function as intended and generate a beneficial biological response, without causing any undesirable local or systemic effects [47]. Additionally, *in vitro* studies of BT-containing composites, e.g. poly(vinyldiene-trifluoroethylene)-BT, hydroxyapatite-BT, and titania-BT, have indicated that also these materials are biocompatible [11]. Furthermore, in the early 1980s, Park et al. carried out *in vivo* studies in which ceramic BT was implanted into the femurs of dogs [48][49]. These studies showed no inflammation or undesired

biological reactions between the implant and the tissue, showing that BT is highly biocompatible *in vivo*. Moreover, these studies indicated that the bone ingrowth, and thus also the strength and adhesion of the implant, was improved. Some years later, in the late 1990s, Feng et al., carried out a new study of piezoelectric ceramics implanted in the jawbones of dogs [50]. Here, the piezoelectric material was a hydroxyapatite-BT composite, and the study concluded that this composite significantly promoted the repair and growth of the bone compared to a pure hydroxyapatite implant. Based on these results, BT is a promising implant material for enhanced bone growth.

2.3 Thin film processing

When applying powder-based ceramic coatings on substrates, heat treatment of the samples is required to get the desired density and adhesion of the coating. The maximum temperatures of these heat treatments can be quite high, depending on the ceramic material in question. However, when working with metal substrates, oxidation of the metal is likely to occur at high temperatures. Therefore, to prevent this oxidation, low-temperature methods for applying coatings are required. There are several examples of these kinds of low-temperature methods, but in the following, a general introduction to sol-gel methods will be given, before the specific modified Pechini variety will be presented.

2.3.1 The sol-gel method

A sol-gel process is an umbrella term for a broad range of wet-chemical methods in which a solution containing the desired cations is prepared, followed by drying of the solution to form an amorphous gel. In a typical sol-gel process, the first step is to make a solution, a sol, of the precursors with the desired cations, in addition to e.g. chelating agents that help stabilize the cations in the solution. These precursors are often organometallic alkoxides, e.g. tetraethyl orthosilicate and titanium isopropoxide, which then undergo hydrolysis and condensation reactions to form metal-oxide networks [18]. This solution can be dried to give an amorphous gel, which subsequently can be heat treated to give a crystalline material. One of the main advantages of the sol-gel method is that the prepared solution contains precursors which are mixed on an atomic scale [18]. In this way, nanosized powders with a high degree of homogeneity and purity can be prepared at a fairly low temperature [41][51]. However, in addition to making nanopowders, the sol-gel method has also successfully been used to make thin films. This is typically done by dip-, spray- or spin-coating [51], where the latter will be discussed further in a following section.

Modified Pechini method

In 1967 Maggio Pechini patented a variety of the sol-gel method, in which carboxylic acids and polyhydroxy alxohols, together with suitable cation precursors, were used to prepare films of titanate and niobate dielectrics [52][53]. This method, commonly known as “the Pechini method”, has subsequently been altered even further, giving variations such as “the citrate gel method”, where no alcohols are utilized, and “the modified Pechini method”, which is based on aqueous precursors [18]. Especially the latter method, being both simple and versatile, has become a popular way of producing complex metal oxides. The starting point of this process is a homogeneous aqueous solution with stoichiometric ratios of the desired cation precursors, as well as selected additives required to ensure a high-quality

end-product. Upon evaporation of the solution, chemical reactions form a cross-linked polymer, with a rigidity that hinders segregation of the cations. Finally, when heat treated even further, this polymer is converted to the desired product of an oxide powder or film with high homogeneity [53]. Typically, the additives required for making the desired solution are chelating agents which form complexes with the metal cations in the solution, to prevent possible precipitation of metal salts. These chelating agents are usually carboxylic acids with multiple carboxylic groups, such as citric acid. However, for the most alkaline cations, such as barium, ethylenediaminetetraacetic acid (EDTA) is often required to help stabilize the otherwise weak complexes. Additionally, the acidity of the solution is often altered by adding e.g. NH_3 to prevent precipitation of the metal salts. Finally, a polyalcohol is added to give polymerization reactions between the alcohol- and carboxylic groups, resulting in a resin-like polyester network with the precursor cations stabilized by unreacted carboxylic groups within the network [53].

The modified Pechini method has been shown to be a suitable route for producing BT thin films [54], but in this method, polyalcohols are added to give the desired polymerization. This gives a large amount of organic matter in the solution, which later has to be removed by a calcination process. However, in 2018, Ræder et al. reported for the first time an aqueous route for producing BT thin films, without utilizing any alcohols [16]. In this study, the Ba-cations from a $Ba(NO_3)_2$-precursor were stabilized with both citric acid and EDTA, and NH_3 was added to avoid reprecipitation of $Ba(NO_3)_2$. The Ti-cations, originating from Ti-isopropoxide, were stabilized with citric acid, and the mixing of these two solutions gave a precursor solution of BT which was reported stable for >2 years at a concentration at 0.25 M. The solution was subsequently deposited onto (100) single-crystal $SrTiO_3$ substrates by spin-coating, and resulted in thin films with good ferroelectric properties.

2.3.2 Thin film processing by spin-coating

Spin-coating

A spin-coating process can typically be separated into four parts, as shown in Figure 2.6. Firstly, the suitable amount of solution, which depends on the size of the substrate, is deposited onto the substrate. This is followed by a spin-up process, where spinning of the substrate distributes the solution over the entire surface. Thirdly, the rotation speed is increased in the spin-off process. During this stage, the increased rotation velocity forces any surplus liquid to be removed from the substrate, leaving only a thin liquid film. Finally, the liquid in the solution is evaporated, giving an amorphous gel of organic and inorganic material. Further heat treatment of this gel will burn off the organics, which results in a dense and crystalline coating of the desired inorganic metal oxides [55].

The thickness of the films produced by spin-coating is highly dependent on the viscosity of the solution. For a more viscous solution, the amount of liquid that is spun off would be less than for a more free-flowing solution, resulting in a thicker film. In addition to this, the spinning velocity of the substrate has a significant effect on the film thickness, where a higher spinning velocity would increase the outwards forces on the solution, thus pushing more solution off the substrate. The thickness of the resulting film is therefore expected to decrease with increasing spinning velocity [51][55]. Also the concentration of the precursor solution used for the spin-coating has been shown to impact the final film thickness, with lower concentrations giving thinner films [56]. Depending on the mentioned parameters,

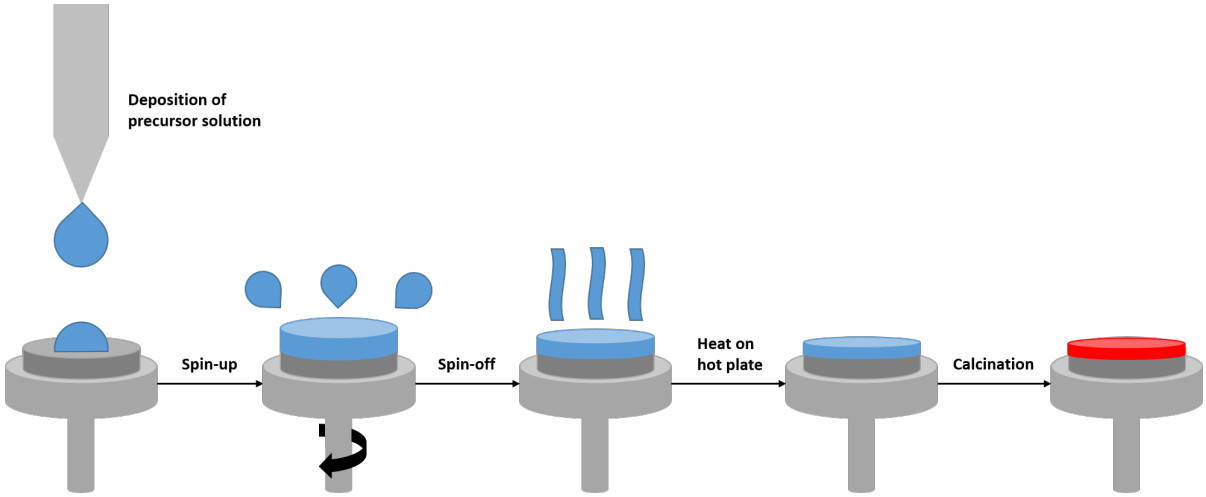

Figure 2.6: The spin-coating process: Deposition, followed by spin-up, spin-off, drying, and calcination.

the films produced by spin-coating are typically in the thickness range of 50-500 nm [51]. However, if a thicker final coating is desired, several layers can be deposited on top of each other.

A combination of variants of the sol-gel method with spin-coating has proven useful to produce a broad range of piezo- and ferroelectric thin film coatings [57]. By reacting lead acetates with zirconium and titanium alkoxides, and subsequently depositing the solution onto silicon substrate materials by spin-coating, Budd et al. showed that it was possible to make ferroelectric PZT thin films with good adhesion to the substrates [58]. Similar studies have later been carried out by e.g. Lakeman and Payne [59] and Tu et al. [60], and show good results, both in terms of adhesion, microstructure and ferroelectric properties. Also BT has successfully been produced via the sol-gel method. Kamalasanan et al. coated substrates of conducting glass, fused quartz, silicon, and stainless steel in 1991 by using a solution of barium 2-ethylhexanoate and titanium tetra-butoxide in acetic acid and methanol [61], and Hayashi et al. deposited BT onto $Pt(111)/SiO_2/Si(100)$ substrates in 1994 [62]. Additionally, both Ræder et al. [16] and Bakken [63] have produced BT thin films by aqueous chemical solution deposition and spin-coating, where Ræder et al. coated $SrTiO_3$ substrates, and Bakken coated both $SrTiO_3$ and platinized silica substrates. All of these studies showed that it was possible to produce BT thin films with good ferroelectric properties and adhesion by sol-gel methods and spin-coating. Based on these initial results, the sol-gel spin-coating methods have been further optimized, and are still widely used in the production of thin films on various substrates.

Wetting

During thin film processing, and especially in a spin-coating process, it is paramount that some of the solution remains on the substrate after the deposition is completed. Whether this is the case or not depends on the interactions between the solution and the substrate. These interactions can be described in terms of wetting, which in turn can be defined as how easily a fluid can spread on or adhere to a solid surface in the presence of other immiscible fluids [64]. Simply put: If the wetting is good, the solution sticks well to the substrate, and if the wetting is poor, most of it will bounce off the substrate. The wetting properties are

commonly described by the contact angle, θ, between a drop of deposited liquid and the substrate, as depicted in Figure 2.7. Usually, good wetting (i.e. a hydrophilic surface) is defined for $\theta < 90°$, while poor wetting (i.e. a hydrophobic surface) is defined for $\theta > 90°$ [64], and this convention will also be used in this report. For now, it is sufficient to say that tailoring of the substrate's surface to ensure good wetting is important in a spin-coating process. A common approach for doing this is by altering the surface roughness and texture of the sample, which will be discussed in more detail later, in Section 2.4.2.

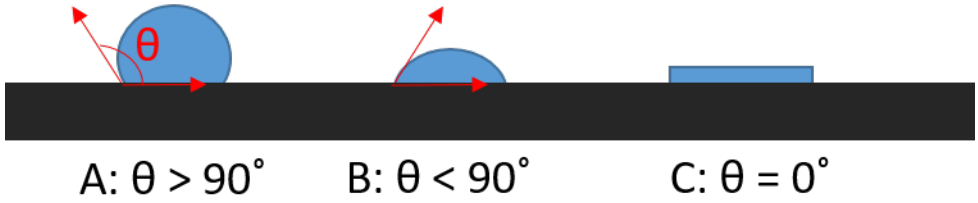

Figure 2.7: Illustration of wetting behaviour: A shows poor wetting, B shows good wetting, and C shows ideal wetting.

Heating programs and chemical reactions

To prevent any undesired oxidation of the metal substrate surface during the final heat treatment of the thin film, it is important to choose suitable processing conditions, both in terms of heating programs and atmospheres. Given that high temperatures and oxidizing atmospheres are required for this oxidation process to happen, there seems to be two simple ways to prevent the oxidation: either to lower the temperature, or to use a reducing or inert atmosphere. However, there are several factors to take into account when making these heating programs. The precursor solution for the thin film contains considerable amounts of organic materials, which have to be burned away to get a crystalline film. Depending on the solution and substrate, this happens at different temperatures, and thus a minimum temperature is required for the making of the film. Furthermore, as the organics typically need oxygen to be burned off, an inert atmosphere might prove challenging for achieving a crystalline film of good quality. Therefore, a compromise between temperature, atmosphere, and degree of substrate oxidation has to be found.

During the process of making said compromises between temperature, atmosphere, and degree of substrate oxidation, the heating programs must also be tailored to fit the stability and processing ranges of the substrate and coating materials, which in this thesis work are Ti6Al4V and BT, respectively. Considering the substrate first, when exposed to air in ambient conditions, titanium and its alloys immediately develop a 5-10 nm thick anatase (TiO_2) layer at the substrate surface. This thin layer is highly desirable when it comes to corrosion resistance, and for the biocompatibility of the titanium alloys [65]. However, several studies have shown that the thickness and nature of this oxide layer is changed drastically upon heat treatment of the metal [65][66][67][68]. Feng et al. showed that heating of a commercially pure titanium sample at 600 °C for 30 min resulted in a thick oxide film, and that the metastable anatase phase was transformed to the more stable rutile phase [65]. Frangini et al. studied the thermal oxidation of Ti6Al4V between 600 °C and 700 °C in air, and found that the oxide layer thickness increased with increasing temperature [66]. Similar results were also found by Lin et al., who investigated temperatures between 600 °C and 750 °C [67], and by Kumar et al., who investigated temperatures between 500 °C and

800 °C [69], both carried out in air on Ti6Al4V. The latter study also found that the oxide layer adhered well to the substrate at 500 °C and 650 °C, while spallation of the oxide layer occurred at 800 °C, implying a weak adhesion. For a coated system, spallation of the oxide layer would also result in the removal of the coating on top of the oxide layer, and is thus highly undesirable. Therefore, the maximum temperature during heat treatment of the coated substrates should be somewhere between 650 and 800 °C, and preferably towards the lower end of this temperature range, to have a safety margin in terms of catastrophic oxidation and spallation.

When it comes to producing BT by the modified Pechini method as described in Section 2.3.1, there are several reactions occurring before the final product is formed. These reactions have previously been thoroughly investigated in two studies by Ischenko et al. [70][71], and more recently by Ræder et al. [16] and by Kristine Bakken in her doctoral thesis [63]. Their findings indicate that a (Ba,Ti)-precursor complex is formed upon mixing of Ba- and Ti-precursors, and that the decomposition of this complex leads to the segregation of Ba-rich and Ti-rich phases. The Ba-rich phase, often called the barium oxycarbonate phase, has a general chemical formula of $BaO_x(CO_3)_{1-x}$, and has a calcite type crystal structure, while the Ti-rich phase, Ba_yTiO_{2+y}, is mostly amorphous [63][71]. Upon heating, these phases react with each other, forming BT according to the following proposed reaction equation [71]:

$$(\mathrm{Ba,Ti})-\text{Precursor complex} \longrightarrow \text{(1-y)}BaO_x(CO_3)_{1-x} + Ba_yTiO_{2+y} \longrightarrow BaTiO_3 \cdot \qquad \{1\}$$

In her doctoral thesis, Bakken conducted thorough investigations on the reactions and processes occurring when going from an aqueous BT precursor solution to a solid BT thin film [63], on a system similar to the one of interest in this Master's thesis. As a result of these investigations, Bakken was able to divide the processing into steps, or temperature regions, which will briefly be discussed in the following. Firstly, a drying step (150-200 °C) was identified, during which water evaporates, and an organic network, with Ba- and Ti-ions bonded in close proximity, is formed. Next, the process goes through a decomposition step (200-460 °C), where decomposition of nitrate and organics starts, and where ammonia evaporates. Furthermore, towards the end of this step, formation of carbonate is initiated. Following the decomposition step, organics are removed and carbonate is formed (460-530 °C), with the oxycarbonate- and Ti-rich phases dominating towards the end of this step. Further heating gives a step of BT nucleation and growth (530-600 °C), where BT is formed according to Reaction 1. Finally, above 600 °C, phase pure BT is formed, as the reaction from the previous step is completed. These findings are similar to those of Ræder et al., who observed the formation of the oxycarbonate phase at 550 °C, before it vanished again at 650 °C, upon formation of phase pure BT [16]. Thus, a temperature above 600-650 °C is expected to be a minimum calcination temperature requirement for producing phase-pure BT thin films by aqueous chemical solution deposition. Combined with the maximum processing temperature for the Ti6Al4V substrate, this leaves a temperature range of approximately 600 to 750 °C for the thermal processing of BT thin films on Ti6Al4V substrates.

2.3.3 Adhesion of coatings

In order to bring the piezoelectrically coated metal substrates from the laboratories and into real applications, it is crucial that the coating adheres well to the substrate. Whether this is the case or not depends on several different factors, but in the following, thermal expansion mismatch and substrate oxidation will be briefly discussed.

Thermal expansion mismatch

Thermal expansion can be described as the dimensional change in a material as the temperature is increased or decreased, and the magnitude of this dimensional change is typically described in terms of thermal expansion coefficients (TEC) [41]. Here, a large TEC-value corresponds to a large expansion or contraction, and vice versa. In an ideal coating situation, the two materials in question have approximately the same TEC-values, and expand and contract at an equal rate, meaning that the materials do not exert any stresses on each other. However, if there is a thermal expansion mismatch, the rate of expansion and contraction will be different. During heating, the material with the highest TEC (material A) will expand rapidly, while the material with the lowest TEC (material B) tries to retain its shape. The interaction between these different layers results in the development of stresses at the interface, which during heating will be compressive in material A and tensile in material B. During cooling, however, the nature of the stresses are inverted. Material A still wants to change its dimensions more rapidly than material B, but due to the change being a contraction, tensile stresses are now developed in material A, while the compressive stresses are developed in material B.

The magnitude of the thermal expansion is highly dependent on the interatomic bonding in the material, with weak bonds resulting in high thermal expansion. Therefore, metallic structures with weak bonds and close-packed structures, such as sodium and potassium, have high TEC-values, while more strongly bonded metals with larger atomic radii, such as titanium and iron, have lower TEC-values. Correspondingly for ceramics, materials with weak ionic bonds, such as NaCl and KCl, experience high thermal expansion, while materials with stronger and more covalent bonds, such as NiO and CaO, have a lower TEC-value [41]. For the BT-Ti6Al4V-system in this project, the TEC-values have been reported to be approximately $12.8 \cdot 10^{-6}\,\mathrm{K}^{-1}$ for BT in the range of 120-1000 °C [16], and $10.3 \cdot 10^{-6}\,\mathrm{K}^{-1}$ for the Ti6Al4V alloy [72]. Furthermore, in a sol-gel process such as the one in this thesis, the coating does not solidify properly before being held at the maximum temperature, and therefore, it is the cooling behaviour that is of greatest interest for this system. Now, BT has the highest TEC, and will therefore be exposed to tensile stresses. Additionally, it is known that ceramic materials are weakest in the tensile mode [41], and fracturing of the BT layer, especially close to the interface, might therefore cause challenges. This fracturing could in turn give poorer adhesion between the layers, eventually resulting in the delamination of the film [72][73].

Despite previously stated that it is the cooling behaviour that is of greatest interest, the processes that occur during heating should not be entirely forgotten. During the final heat treatment of the coated samples, organic matter will be burned off, and the films will solidify and densify. As a consequence of this, the new layer of coating is expected to shrink during heating. Above a certain temperature, where bonding between coating and substrate have been established, this densification would result in tensile stresses in the coating, which also would contribute to cracking of the coating [72]. Additionally, during heating, the Ti6Al4V

substrate will exert compressive stresses on the already deposited and calcined layers of coatings, as described previously. These compressive stresses might cause buckling and blistering of the film at the coating-substrate interface, which in turn can contribute to the delamination of the coating [74][75][76].

Oxidation of substrate

As mentioned before, the metal substrates used in this project will oxidize when heat treated in air, and the extent of this oxidation is expected to affect the adhesion between the coating and the metal. In 2001, Wei et al. investigated the adhesion of the ceramic material hydroxyapatite (HAp) on several metal substrates, with Ti6Al4V being one of these [72]. This study found that a thick metal oxide layer developed at the HAp-Ti6Al4V-interface, when the Ti6Al4V substrates were heat treated at maximum temperatures between 875-1000 °C, and subsequent SEM-imaging of the samples showed fracturing either between the metal oxide and the HAp or within the metal oxide layer. Based on these results, the authors identified the thick and porous oxide layer of Ti and Ti6Al4V as a weak link in the system [72], thus naming substrate oxidation as a possible problem for good adhesion.

However, other studies indicate that an preexisting surface oxide layer actually can improve the coating-substrate adhesion. It has been shown that TiO_2-coatings placed between e.g. hydroxyapatite and titanium substrates can improve the bonding between the layers [77][78], and in a study on sol-gel produced hydroxyapatite coatings on titanium substrates, Xu et al. investigated the surface structure of the TiO_2-layer to be coated with hydroxyapatite [77]. Their investigations revealed a cracked surface, created by the differences in mechanical and thermal properties during heating. When applying a coating to this cracked surface, the solution will be able to penetrate into these cracks, and the increased contact area between coating and substrate would ultimately result in a greater adhesion. However, it is worth noting that this is the case when the oxide layer is created on purpose before the ceramic coating itself is applied. During the calcination step, the oxidation of the substrate still continues, which eventually might be detrimental for the coating adhesion.

2.4 Surface texture effects

When producing metallic substrates spin-coated with a piezoelectric coating for bone replacement implants, the surface texture of the substrate is important for several reasons. (i) When implanted, it is the surface of the implant that the cells in the body will interact with. Their biological response are dependent on the roughness and texture of this surface, which ultimately stems from the texture of the metal substrate. (ii) It is the surface of the metal substrate that is coated during the spin-coating process. The wetting behaviour, and thus the coatability, of the substrate is dependent on the surface roughness, and any surface texturing of the metal substrate will have an important effect. (iii) The surface texture of the metal substrate affects the adhesion of the coating to the substrate, which is crucial for the quality of the end product. In order to get a better understanding of the importance of the surface roughness and texturing of the metal substrate, the following section will examine each of the above-mentioned cases, before briefly outlining how such textures can be made.

2.4.1 Texturing effects on bone growth

In addition to the effects of piezoelectricity, described in Section 2.1.3, it has been shown that substrate texturing and surface roughness have significant impacts on the bone-implant fixation. In 1991, Buser et al. reported on an *in vivo* study where hollow-cylinder implants with different surface roughness were inserted into the tibia and femur of miniature pigs [79]. The results of this study clearly showed an increase in bone-implant contact with increasing implant roughness, which would result in an improved bone fixation. Furthermore, *in vitro* studies carried out by Bowers et al. lead to the suggestion that implants should be made rough, on the basis that rough, sandblasted surfaces resulted in significantly higher levels of cellular attachment [80]. Indeed, taking advantage of rough and porous structures to give a better possibility for bone growth into the bulk of the implant, and also better clamping on the implant surface, has now become a popular method of improving the bone-implant fixation [14].

However, the bone-implant fixation is not the only property that is affected by the surface texture of the implant. In 1995, Martin et al. published a study which investigated the effect of surface roughness on osteoblast proliferation, differentiation and protein synthesis [81]. This study showed that the mentioned properties not only were significantly influenced by the magnitude of surface roughness, but also on the type of texturing. Furthermore, in 2001, Deligianni et al. investigated the effect of surface roughness of a Ti6Al4V substrate on human bone marrow cell response, and found, similarly to Martin et al., that both cell attachment and proliferation increased with increasing surface roughness [82]. In another study, Deligianni et al. also investigated the effect of hydroxyapatite surface roughness on human bone marrow cell adhesion, proliferation, differentiation and detachment strength, and once again found that all of these factors, apart from from cell proliferation, were improved [83]. As an added benefit, the above-mentioned properties do not only affect bone growth, but are also important for the final ingrowth and fixation of the implant [15]. Therefore, it is safe to say that surface roughness and texture have an important impact on cell behaviour and implant ingrowth and fixation, and tailoring of these properties is important to achieve the best implants possible.

2.4.2 Texturing effects on spin-coating

As mentioned in Section 2.3.2, tailoring of the surface properties of the substrate to be coated in a spin-coating process is important to ensure good wetting, and thus produce coatings of high quality. There are several factors that can be altered for this tailoring, but most of them can be explained by how the interactions between the liquid and the substrate are changed. One of the most important of these is the substrate surface roughness, often described as small, finely spaced deviations from the nominal surface [84], and in the following, the effect of surface roughness on substrate wettability, as well as the overall coating quality, will be discussed.

When surface roughness is introduced to the substrate surface, it will no longer be completely smooth, but contain e.g. polishing grooves, and the wetting behaviour will depend on whether or not the deposited liquid is able to fill these grooves, as shown in Figure 2.8. Firstly, if the liquid is able to fill the pores, a liquid-air interface will be replaced by a solid-liquid interface, which would change the contact angle according to the Wenzel

model [85],

$$cos\theta_w = r\, cos\theta, \tag{2.2}$$

where θ is the contact angle for the smooth surface, θ_w is the contact angle for the rough surface, and r is a roughness factor based on the area ratio between the actual surface and the apparent surface. For a rough surface, small grooves and ridges will make the actual surface larger than what it appears to be, which gives that $r > 1$ [85][86]. Based on this relation, it is possible to predict how the surface roughness will affect the wetting. Firstly, if $\theta < 90°$, then $\cos\theta > 1$, and $r\cos\theta > \cos\theta$, which gives $\theta_w < \theta$. Otherwise, if $\theta > 90°$, then $\cos\theta < 1$, and $r\cos\theta < \cos\theta$, which gives $\theta_w > \theta$. Another way of putting this is that surface roughness will amplify the existing wetting behaviour compared to the completely smooth surface, meaning that if the wetting was poor, roughness will make it even poorer, and vice versa. This relationship can also be explained in a more intuitive way: If a solid-liquid interface is preferred over a liquid-air interface, an increased contact area with solid compared to air would give a better wetting.

However, if the deposited liquid is not able to fill grooves and other surface features on a rough sample, the wetting will no longer follow the Wenzel model. Instead, the wetting will follow a state described by Cassie and Baxter, where air is trapped in pores or grooves underneath the deposited liquid [87]. For this case, the contact angle, θ_c can be found from the relation

$$cos\theta_c = f_1\, cos\theta_1 - f_2, \tag{2.3}$$

where θ_1 is the contact angle on a smooth surface of the material, f_1 is the total area of solid material underneath the droplet per estimated area underneath the droplet, and f_2 is the corresponding value for air under the droplet [87][88]. It should be observed that if $f_2 = 0$, i.e. if there is no air underneath the drop, this equation reduces to the Wenzel mode as shown in equation 2.2. To illustrate Cassie-Baxter behaviour, an example study on fibres placed in a grid-pattern can be used. This study showed that when the distance between two fibres was large compared to the radius of the fibres, the apparent contact angle increased [87]. As the distance was increased, more of the solid area underneath the droplet was replaced with air, meaning that f_2 was large, and f_1 was small. Thus, as $\cos\theta_1$ is negative when the wetting is poor, a large θ_c was expected. However, it was important that the spacing between the fibres was not too large, as this would allow the deposited liquid to solely be located at a flat area between the fibres, and thus ”ignore“ the grid pattern, which caused the Cassie-Baxter behaviour in the first place. Therefore, a small radius of the fibers is required to get proper Cassie-Baxter behaviour.

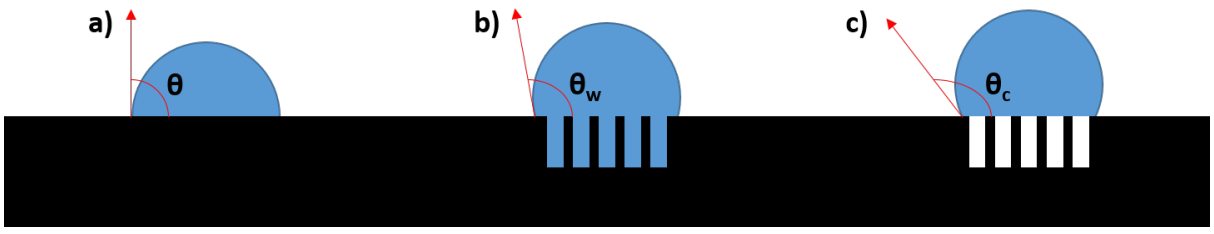

Figure 2.8: Illustration of wetting modes: a) a smooth surface, b) Wenzel mode, and c) Cassie-Baxter mode.

A second factor influencing the wetting properties is the cleanness of the surface. If an aqueous solution is to be deposited onto a substrate, but the surface of the substrate contains some hydrophobic organic residue, e.g. lubricants from polishing, or simply grease from a fingerprint, the wettability will be decreased. Due to this, surface cleaning methods such as plasma cleaning have been shown to improve the wetting compared to an uncleaned substrate [89].

From the previous discussion, it is clear that the substrate surface roughness and texture affect the spin-coating process through the wettability of the substrate, but conversely, it has also been shown that the spin-coating procedure itself can have a significant impact on the final surface roughness of textured substrates [90][91][92]. Experiments carried out by Stillwagon et al., where textured substrates were coated with different types of epoxy, showed that the planarization, i.e. the flattening of surface texture, increased with increasing time between the completion of spinning and the start of curing [90]. This observation was explained by the impact of capillary and gravitational forces, which would act to level the still viscous fluid. Moreover, it was observed that a less viscous fluid resulted in a more rapid planarization, as the viscous force counteracting the capillary and gravitational forces was lower. Also Gupta and Gupta studied the parameters that influence planarization during spin-coating, by coating silicon substrates with polymer solutions [92]. Amongst other things, this study concluded that an increased spinning speed always causes a decreased planarization, and that periodic features on the substrate result in greater planarization than isolated features. Additionally, it was found that more concentrated solutions typically resulted in more uniform surfaces, as these solutions would shrink less during drying. Thus, from the two studies mentioned above, some key points for retaining the substrate surface texture after spin-coating are to (i) cure the solution immediately after spinning is completed, (ii) coat the substrates at a high spinning speed, and (iii) use low-concentration solutions with as high viscosity as possible.

2.4.3 Texturing effects on coating adhesion

When coating substrates with surface texturing, the roughness might affect the adhesion of the coating to the substrate in several ways. Firstly, as discussed in Section 2.4.2, the roughness will change the wetting properties of the substrate, which in turn will determine how much of the deposited solution that can attach to the substrate. Additionally, the surface texture can provide a method for mechanical bonding of the coating to the substrate. As long as the wetting is sufficiently good, the applied solution will be able to fill scratches, pores, and any other topological features on the substrate surface. In addition to providing an increased contact area between the coating and the substrate, which is beneficial for the adhesion, these features can result in mechanical interlocking, where the film is clamped tight to the substrate [78]. This was one of the cases for the improved adhesion in the study by Xu et al. [77], discussed in Section 2.3.3, but also a study by Piveteau et al. [93] showed similar results. In this study, the authors investigated the mechanical adhesion of calcium phosphate containing TiO_2 coatings, produced by the sol-gel method, to titanium substrates with different surface roughness. By carrying out rotating bending testing and tensile bond testing, it was found that the adhesion increased with increasing roughness on the micrometer scale, thus showing that the mechanical adhesion was significant for this system.

2.4.4 Laser-texturing of metallic substrates

For the production of the rough, or textured, surfaces mentioned above, a wide range of surface treatments can be employed. These treatments include traditional methods such as titanium plasma spraying, grit-blasting, acid-etching, which all have successfully been used to roughen the surfaces of titanium alloy implants [94]. However, a more modern and accurate method for producing patterns on metal substrates is to use ultra-fast laser machining techniques, whereof the direct femtosecond laser ablation processing has gained traction the recent years [95]. This method is suitable for a wide range of material types with an equally wide range of geometrical forms, and can generate nanostructures on the surface, ranging from micro- to macroscale at ambient conditions [96]. This process is carried out by irradiating the surface to be textured with a femtosecond laser beam, which interacts with the electrons of the material, exciting and thermalizing them. The thermalized electrons subsequently heat the surrounding lattice, causing local melting and ablation, which happens on the pico- to nanosecond timescale. Following the ablation, the surface cools down rapidly and solidifies to produce the desired structures [96], which depend on the input parameters for the process. As shown by Schnell et al., in two different studies on Ti6Al4V substrates, these structures can vary greatly, ranging from nanosized laser-induced periodic surface structures (LIPSS) to macroscale grid-patterns [97][98]. The properties of these structures will in turn affect several processes related to the production and application of coated metal substrates for biomedical applications, and the selection of correct surface texture for the desired application is therefore important.

2.5 Mechanical properties of thin films

During the production of ceramic thin films on metallic substrates, the processes during the solidification and calcination of the films exert stresses on the films. The resulting strains in the films can be detrimental to the film integrity, both in terms of cracking and adhesion, and it is therefore crucial that the mechanical properties of the films are good enough to withstand these stresses.

2.5.1 Strain development in thin films

In general, there are three main mechanisms by which strain is developed in crystalline thin films deposited on non-deformable substrates, as outlined by Nix in 1989 [99]. Firstly, if the thermal expansion coefficient of the film material differs from that of the substrate material, the different rates of expansion and contraction will cause thermal strains to be developed, as described in greater detail in Section 2.3.3. Secondly, growth strains, also known as intrinsic strains, can develop if the dimensions of the film change after it has been bonded to the substrate. These dimensional changes are often related to changes in density during the firing process of the films, where water, organics and additives are burned off to leave a solid film. When investigating a thermal barrier system consisting of a yttria-stabilized zirconia thermal barrier coating on a (Ni,Pt)Al bond coat, Mumm et al. looked closer into the growth strains arising during thermal cycling, and whether they contributed to the final failure of the systems [100]. By doing this, it was found that the thermally grown oxide film between the bond coat and the thermal barrier coating grew

thicker during thermal cycling, which resulted in the development of growth strains. These strains caused crack nucleation and extension, and ultimately contributed to the failure of the thermal barrier coating.

The third and final mechanism for strain development identified by Nix is epitaxial mismatch between the film and the coating, which arises as the film, on a microscopical level, tries to accommodate the mismatch in the lattice parameters of the film compared to those of the substrate [99]. This type of strain has proven to be a challenge for a $LaAlO_3/SrTiO_3$ system investigated by Liu et al., where lattice mismatch at the interface between the two materials resulted in epitaxial strains [101]. In this study, it was found that when the thickness of the $LaAlO_3$ exceeded a critical value, a rapid relaxation of the epitaxial strain occurred, while simultaneously releasing a large amount of energy. As the resistance of $LaAlO_3$ to cracking was found to be lower than the amount of released energy, this resulted in crack formation on the film surface. The epitaxial strains might also occur together with the two other aforementioned strain types, depending on the type of materials and processing conditions. Therefore, when making thin films on substrates, the mechanical properties of the thin films have to be sufficiently good to withstand all of these strains, without experiencing cracking, delamination, or catastrophic failure.

2.5.2 Testing of mechanical properties

To determine whether or not the mechanical properties of the thin films are sufficiently good, several different tests can be carried out. Only for adhesion testing, which will be the main focus in the following, there are over 200 different testing methods [102], depending on the material systems in question. Understandably, it is impossible to assess all of these, and the main focus of this section will therefore be on scratch- and indentation tests.

Scratch testing

During a typical scratch test on a film, a diamond tip or a stylus is placed onto and drawn across the film, with the application of a vertical and increasing load to the tip during the scratching. The monitoring of this increasing load, combined with observations of the point on the scratch where film detachment firstly occurs, allows for the determination of the film's critical load, i.e. the maximum load the film can withstand without detaching from the substrate [102][103]. This procedure has successfully been employed by e.g. Kuo and Yen to determine the critical load for detachment of electrochemically deposited hydroxyapatite coatings on biomedical titanium [104], and likewise by Nie et al. for layered bioceramic hydroxyapatite/TiO_2 coatings deposited on Ti6Al4V substrates by micro-arc oxidation and electrophoresis [105].

A newer and more advanced variety of regular scratch tests is the nanoscratch test, which is commonly used for determining adhesion strength and the modes of mechanical failure for thin ceramic coatings. When compared to regular scratch tests, the loads and scratch tip radii of the nanoscratch tests are significantly smaller, and it is these features of the nanoscratch test that make it more suitable for determining the properties of thin films [106]. The nanoscratch technique has been used by Nieh et al. to determine the interfacial strength between magnetron sputtered hydroxyapatite coatings and titanium substrate [107], and by Dey et al. to determine the critical normal load that leads to delamination of mircroplasma sprayed hydroxyapatite coatings on stainless steel SS316L substrates [108].

Additionally, the nanoscratch technique has been used by Jouanny et al. to determine the friction coefficient of TiO_2 thin films deposited by radiofrequency reactive sputtering on Ti6Al4V substrates [109]. Based on this, it is clear that the nanoscratch technique is well-suited for determining important properties of thin films produced by several different methods, where the adhesion strength perhaps is the most important.

Indentation testing

For a film-substrate situation, the typical indentation test is used to determine properties such as the film hardness and Young's modulus, as well as film detachment and cracking, and works by indenting a sharp diamond tip into the material in question [102][110]. This method has successfully been used by e.g. Musil and Jirout to investigate the cracking and toughness of a wide range of ceramic thin films made by magnetron sputtering [111], and by Perumal et al. to determine the hardness of a Al_2O_3-40 wt% 8 mol% yttria stabilized zirconia composite [112]. As in the case of scratch testing, the classical indentation test has a nano-ranged counterpart, namely the nanoindentation test. This test employs smaller indenters, thus allowing smaller sample volumes to be investigated [113], which has proven useful when investigating thin films with thicknesses on the nanoscale. The nanoindentation technique has been used to determine the mechanical properties, and especially hardness and Young's modulus, by Nieh et al. [107], Dey et al. [108], and Jouanny et al. [109], whose materials systems were discussed in the section on nanoscratch testing. Additionally, Hahn et al. used nanoindentation to determine the mechanical properties of a hydroxyapatite-carbon nanotube composite deposited on a Ti substrate by aerosol deposition [114], and Fan et al. used nanoindentation to look at the elastic modulus and scratch resistance of a composite coating of collagen protein and calcium phosphate minerals, made by a procedure that involved electrolysis to induce self-assembly of the collagen fibrils [115]. Thus, also nanoindentation has proven itself useful for determining mechanical properties of several different types of coating, and is a test to be considered when working with thin film systems.

2.6 Electrical properties of thin films

In order to test the dielectric properties of thin films, conductive electrodes have to be deposited onto the films, and external voltages are applied to the samples. To be able to understand the mechanisms and reactions occurring during the dielectric testing, the following sections look deeper into the electrical properties of a system consisting of a metal substrate and a piezoelectric ceramic coating.

2.6.1 The influence of coating quality on its piezo- and ferroelectric properties

Based on the literature, it is clear that the electrical properties of the film are highly dependent on the film quality. A study on the effect of porosity on PZT films on silicon substrates, prepared by the sol-gel method by Zhang et al., found that both the remnant polarization and coercive field were lower for PZT-films with 3 % pores, compared to dense films (<1 % pores) [116]. Based on these results, the authors concluded that porous films probably are less suitable for the piezoelectric or ferroelectric applications. Similar results were also found by Stancu et al., who investigated pores in sol-gel produced PZT thin films on platinized silicon substrates [117]. In this case, the porosity was controlled by the

addition of the organic macromolecule polyvinylpyrrolidone to the precursor solution, and the resulting pores were once again found to reduce both the remnant polarization and the coercive field of the films.

Also the degree of crystallinity has been found to impact the electrical properties of the coatings. A study on organic, ferroelectric poly(vinylidene fluoride-trifluoroethylene) thin films on platinum-coated silicon wafers by Zhang et al. investigated how film thickness and crystallinity affected the ferroelectric properties of the film [118]. The results revealed a critical film thickness of 100 nm, below which the crystallization process is hindered, yielding a low crystallinity. An abrupt decrease in remnant polarization was also observed below this critical film thickness, which fits well with the fact that ferroelectric responses primarily originate from the crystalline phase [118]. The observations regarding polarization also correspond nicely with earlier studies on more traditional ceramic ferroelectric materials. One of these studies, by Hayashi et al., investigated how the dielectric properties of sol-gel-produced BT thin films deposited on Pt(111)/SiO_2/Si(100)-substrates depended on the film thickness [62]. Here, it was found that the crystallinity increased as the film thickness was increased from 0.25 to 0.58 µm, while at the same time, the remnant polarization doubled, and the coercive field was reduced by two thirds. Finally, a study from Thomas et al. on RF magnetron sputtered PZT on platinized glass substrates, investigated the influence of annealing properties on the thin film's ferroelectric properties [119]. By annealing the samples at temperatures in the range of 500-700 °C, it was found that the remnant polarization increased and coercive field decreased as the annealing temperature was increased, once again explained by the growth of crystallites. As the annealing temperature increased, more of the intermediary phase was converted into the desired perovskite phase, which also contributed to the improvement of the dielectric properties. Thus, based on the three above-mentioned studies, a high degree of crystallinity is important to achieve good (ferro)electric properties.

2.6.2 Metal-Insulator Junctions

When a metal is brought into contact with a semiconductor with a different band structure, bending of the semiconductor bands will occur to align the Fermi levels of the materials. Depending on the relationship between the work functions (Φ_i) of the materials, which describe the distance from the Fermi level to the vacuum level, and the type of majority charge carriers in the semiconductor, this can give rise to two different types of contacts. If, for an n-type semiconductor, the work function of the metal is larger than that of the semiconductor, a Schottky contact is developed, while an Ohmic contact is developed for the opposite case. This can also be explained in terms of Fermi levels, where if the Fermi level of the semiconductor is higher than that of the metal, a Schottky contact is developed, while a lower semiconductor Fermi level results in an Ohmic contact. The set of rules used for determining the contact type for the different types of semiconductors is shown in Table 2.3 [120][121].

Table 2.3: Overview of the junction contact type for n- and p-type semiconductors (SC) in contact with a metal (M), where the semiconductor Fermi level (E_F) or work function (Φ) is greater or smaller than that of the metal.

Junction contact type	n-type semiconductor	p-type semiconductor
Schottky	$E_{F,SC} > E_{F,M}$ ($\Phi_{SC} < \Phi_M$)	$E_{F,SC} < E_{F,M}$ ($\Phi_{SC} > \Phi_M$)
Ohmic	$E_{F,SC} < E_{F,M}$ ($\Phi_{SC} > \Phi_M$)	$E_{F,SC} > E_{F,M}$ ($\Phi_{SC} < \Phi_M$)

Schottky contact

If an n-type semiconductor is brought into contact with a metal with a lower Fermi level, electrons will spill over from the conduction band of the semiconductor and into the metal, and the semiconductor conduction band bends away from the Fermi level, as shown in Figure 2.9. This spilling of electrons results in a negative charge on the metal side of the junction, while a positive region depleted for electrons is developed on the semiconductor side. As a result, a contact potential, eV_0, is developed across the junction region, which at equilibrium prevents more electrons to move from the semiconductor and into the metal. Furthermore, as the semiconductor conduction band is bent away from the Fermi level of the metal at the junction, an energy barrier which prevents electrons from moving from the metal and into the semiconductor is developed. This barrier is known as a "Schottky barrier", denoted Φ_B, and depends on both the work functions and the overall band structure of the materials in question,

$$\Phi_B = (\Phi_M - \Phi_n) + (E_C - E_{F,n}) = \Phi_M - \chi_n, \tag{2.4}$$

where E_C is the energy level of the semiconductor conduction band, E_F is the Fermi level, and χ_n is the electron affinity of the semiconductor, i.e. the energy difference between the conduction band and the vacuum level [120][121].

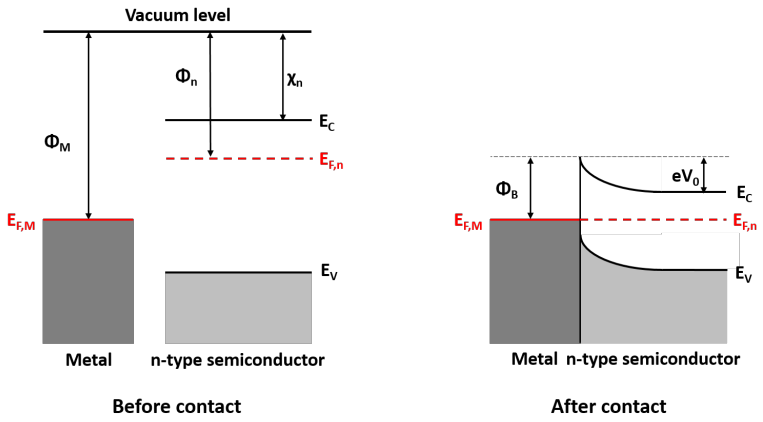

Figure 2.9: Band-structure of a metal/n-type semiconductor couple before and after Schottky contact, based on information from Sze [120] and Pierret [121].

A general characteristic of a Schottky contact is that it behaves differently depending on the direction of an externally applied bias. Upon application of an external bias, V_{App}, the Fermi levels of the two materials are no longer aligned, and the discrepancy depends on the magnitude of the applied bias. For a forward bias, i.e. when the external potential is

applied in the direction that opposes the built-in potential, the injected electrons experience a lower potential barrier for moving from the semiconductor and into the metal. This results in current that increases with increasing potential, as shown in Figure 2.10a). However, when a reversed bias is applied, the built-in potential is enhanced, making the potential barrier for electron movement from semiconductor to metal higher. In this case, the reverse bias makes electrons move from the metal and into the semiconductor, as shown in Figure 2.10b), but to do this, they must overcome the Schottky barrier. This barrier is far greater than the built-in potential barrier for the forward bias case, and the resulting current is thus significantly smaller. Therefore, a Schottky barrier is rectifying, allowing current flow when an external potential is applied in one direction, but minimal current flow when the potential is reversed, as shown in Figure 2.12 [120][121].

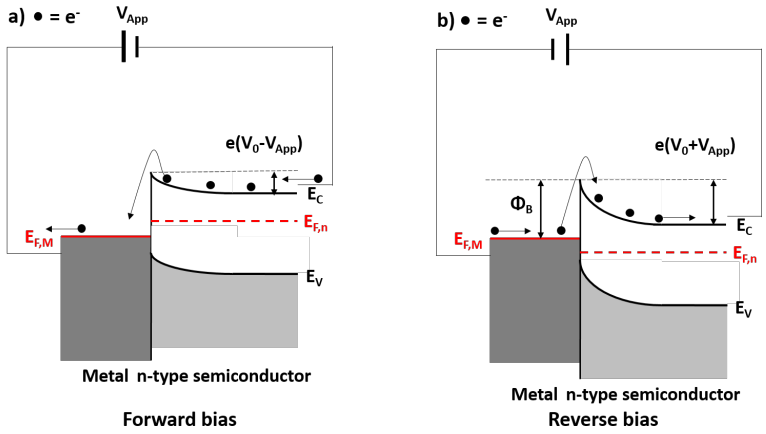

Figure 2.10: Illustration of the band-structure of a Schottky contact with an applied a) forward bias, and b) reverse bias, based on information from Sze [120] and Pierret [121].

Ohmic contact

If an n-type semiconductor is brought into contact with a metal with a higher Fermi level, electrons will spill over from the metal and into empty states in the conduction band of the semiconductor. This causes electrons to accumulate in the region close to the interface, resulting in a bending of the semiconductor conduction band towards the Fermi level of the metal, as shown in Figure 2.11. Due to the higher concentration of electrons, this region is more conductive than the rest of the semiconductor. As the conduction band of the semiconductor now bends towards the Fermi level of the metal, no equivalent to the Schottky barrier is developed, neither is there any built-in potential barrier for electrons moving from the semiconductor and into the metal. Thus, the Ohmic contact conducts current equally well under both forward and reversed bias, resulting in the I-V characteristics shown in Figure 2.12 [120][121].

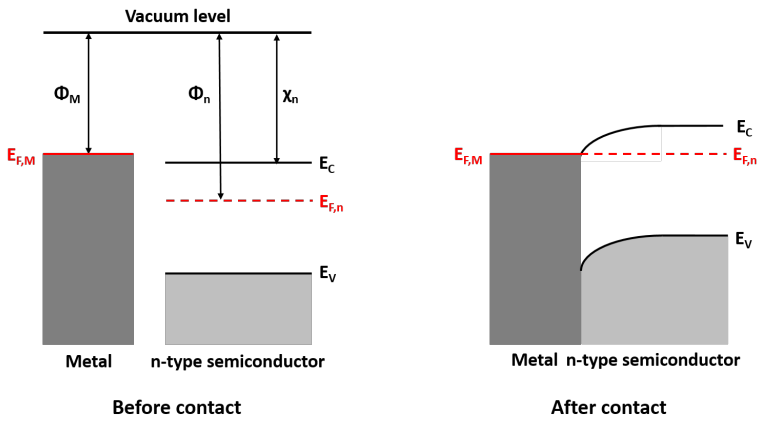

Figure 2.11: Band-structure of a metal/n-type semiconductor couple before and after Ohmic contact, based on information from Sze [120] and Pierret [121].

Based on the previous discussions regarding Schottky and Ohmic contacts, the following "rule" emerges: At a Schottky contact, there will be a depletion of the majority charge carriers, resulting in the majority carrier band bending away from the Fermi level, while at an Ohmic contact, there will be an accumulation of the majority charge carriers, resulting in the majority carrier band bending towards the Fermi level. Although having discussed the case of an n-type semiconductor, the same general rule also holds for p-type semiconductors, leading to the energy relationship criteria previously defined in Table 2.3 [120][121].

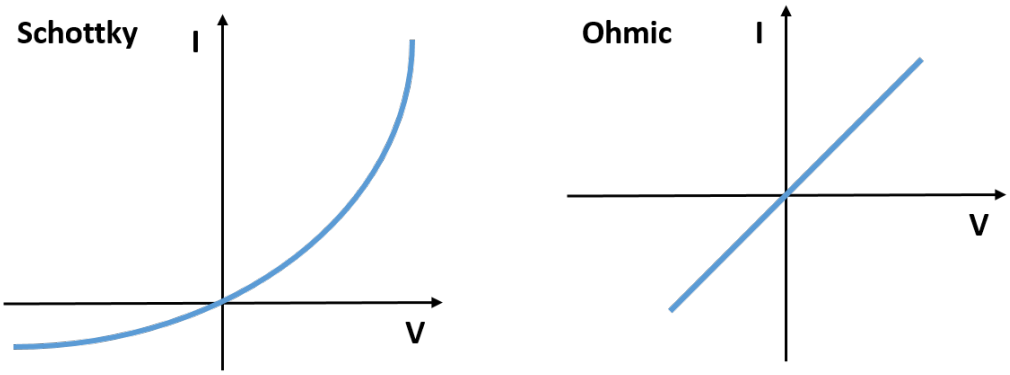

Figure 2.12: I-V Characteristics of a Schottky contact (left), showing rectifying behaviour, and of an Ohmic contact (right), showing non-rectifying behaviour.

BT based systems

When investigating systems where BT thin films have been applied to metallic or ceramics substrates, typically two electronic contacts with BT and another material can be found. Firstly, and perhaps most importantly, is the contact located between the BT thin film and the substrate itself, which will be present as long as the film is adhered to the substrate. From the literature, it has been found that some of the most popular substrates to coat BT onto are based on Pt or $SrTiO_3$ (STO), where e.g. Stanescu et al. investigated BT deposited onto both of these substrates by the molecular beam epitaxy method [122]. Also Ræder et al. deposited high-quality BT thin films on STO substrates, but this time by chemical solution

deposition [16], while Park et al. used radio frequency magnetron sputtering to deposit BT onto a Pt/Ti/SiO_2/(100) Si platinized silicon substrate [123]. BT has also successfully been used in multilayer structures with both Fe and Ni, investigated by Duan et al. [124] and Liu [125] respectively. From the aforementioned studies, it can be seen that a wide variety of materials can be used as substrates for BT thin films, revealing the versatility of BT.

Secondly, and perhaps more easily forgotten, is the contact between the BT film and the top metallic electrodes deposited onto the film, typically to be able to measure electrical properties of the films. For this top electrode, the most common material is Pt, which amongst others Ræder et al. [16], Abe et al. [126], and Stengel et al. [127] successfully used to measure piezoelectric properties. The latter of these studies also examined the possibility of using $SrRuO_3$ (SRO) as the top electrode instead of Pt, and found that the SRO electrodes were significantly better in terms of polarization at the metal/ferroelectric boundary. Also Park et al. successfully used SRO, both as top electrode and substrate, to measure the electrical properties of BT [128]. Additionally, both Ag and Au have been used as electrode materials, e.g. by Stanescu et al., who used both [122], and by Kaemmer et al., who compared electrical properties of a Pt/BT/Au system with a $YBa_2Cu_3O_{7-x}$ (YBCO)/BT/YBCO system [129]. This study found only weak ferroelectric properties when the gold electrode was used, while a more typical ferroelectric hysteresis loop could be identified when YBCO electrodes were used. As the electrode material obviously plays an important role in the measurement of the ferroelectric properties, this must be taken into careful consideration when designing and selecting materials for the final system to be measured on.

2.6.3 Electromigration in BT/TiO_2/Ti6Al4V samples

In a layered system with layers of different materials, it is important to look at how the layers in the system respond to their surroundings. As previously described, the purpose of the BT/TiO_2/Ti6Al4V multilayer system described in this thesis is as a coating on bone replacement materials, and it is the piezoelectricity of the BT layer that is the functional component. Therefore, the dielectric properties of the system have to be tested, and during these tests, external voltages are applied to the system. Due to this, it is useful to take a deeper look into how this system will behave when exposed to an electric field, and especially if and how atomic or ionic movement and reactions will occur. Thus, in the following, the basic theory of electromigration, along with some relevant examples, will be described.

The basics of electromigration

Electromigration can in simple terms be described as migration of materials as a consequence of an electric field [130], or more advanced as forced atomic diffusion, with an electric field and associated electric current in metals as the driving force [131]. This is an important failure mechanism in thin films as opposed to bulk materials, due to the short length scales and correspondingly high electric fields involved. When an electric field is applied, the affected material will experience two forces: F_{Field}, a purely electrostatic force caused by the applied field, and F_{Wind}, the electronic wind force caused by the momentum transfer between electrons and the ions in the crystal lattice. These forces act in different directions, with F_{Field} acting in the direction of the electric field, and F_{Wind} acting in the opposite direction of the applied field (the direction of moving electrons), as indicated in Figure 2.13 [130][131].

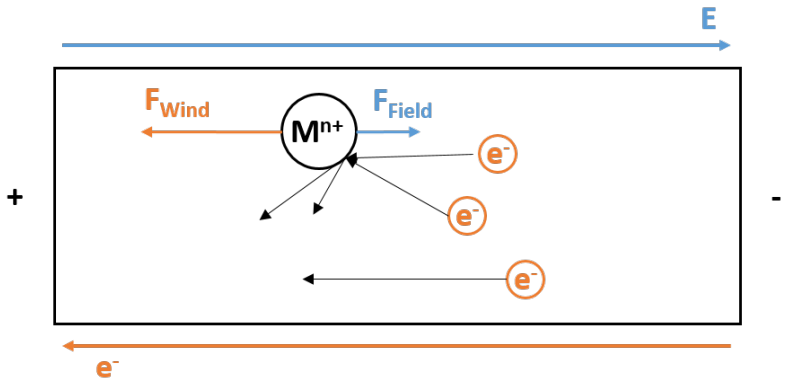

Figure 2.13: Schematic overview of the forces acting on a metal ion during electromigration. The electric field force, F_{Field}, acts in the direction of the electric field, while the electron wind force, F_{Wind}, acts in the direction of electron flow. It should be noted that the wind force, that arises when electrons "bump" into the metal ions, is far greater than the field force, thus dominating the migration.

For the case of a typical conductive metal, the metal ions will to some extent be shielded by the conductive electrons, thus reducing the effect of the purely electrostatic force on the metal ion. The conductive electrons, on the other hand, are not shielded or hindered in any such way, and the flow of electrons colliding with and transferring momentum to the metal ion will be large, making the electron wind force correspondingly large. As a consequence of this, the electron wind force is significantly larger than the electric field force, making the latter negligible. Thus, metal ions tend to migrate in the opposite direction of the applied electric field [130].

In general, there are two main types of electromigration: solid-state electromigration and electrolytic electromigration. The former of these is what has been explained until now, while the latter is the subject of the following section. Whereas the solid-state electromigration is based on the electron momentum transfer, and typically requires high temperatures and high current densities, the electrolytic electromigration is an electrochemical phenomenon where ionic transport happens at ambient temperatures and low current densities. However, for this reaction to happen, the presence of moisture is required [130][132]. The amount of moisture required is material-dependent, ranging from humid to actually wet surfaces [132], but in general, the metal is oxidized, and the resulting metal ions are dissolved in any moisture present on the sample surface. Thus, oppositely to the case of solid-state electromigration, the free metal ions now migrate in the direction of the electric field, from anode to cathode [130][132]. Finally, Table 2.4 briefly summarizes the differences between solid-state and electrolytic electromigration.

Table 2.4: Summary of the differences between solid-state and electrolytic electromigration, based on information from Lienig and Thiele [130] and Krumbein [132].

Migration type	Transport mechanism	Temperature	Current density
Solid-state	Electron momentum transfer	High (> 150 °C)	High (> 10^4 A cm^{-2})
Electrolytic	Ionic transfer	Ambient (< 100 °C)	Low (< 10^{-3} A cm^{-2})

Oxygen vacancies

The electromigration of oxygen vacancies has been shown to have a tremendous impact on the electrical properties of several dielectric systems [122][133][134][135], and is therefore important to assess. Furthermore, oxygen vacancies are some of the most common point defects in semiconducting metal oxides [135], and in the BT/TiO_2/Ti6Al4V system in focus for this thesis, they can be found in the piezoelectric BT layer, and in the TiO_2-layer that is developed by oxidation of the substrate.

There are several ways oxygen vacancies can be generated in TiO_2. One of the most common of these is by doping with foreign elements, where the charge neutrality requirement ensures the creation of oxygen vacancies when a metal ion of lower valency substitutes the Ti^{4+} in the host structure [18][135]. By employing Kröger-Vink notation for an arbitrary example of doping Fe^{3+} into TiO_2, the following reaction equation can be obtained,

$$2\,Fe^{3+} \xrightarrow{2\,TiO_2} 2\,Fe'_{Ti} + 3\,O^{X}_{O} + V^{\cdot\cdot}_{O}, \qquad \{2\}$$

where $V^{\cdot\cdot}_{O}$ denotes the generated positively charged oxygen vacancy. Depending on the valency of the metallic dopant, a different amount of oxygen vacancies will be created, but similar reaction equations can be created in all cases. However, not only metallic elements can be used as dopants, but also non-metallic elements such as carbon can be used [135]. In this case, one negatively charged carbon atom, C^{4-}, replaces two oxygen atoms in the crystal structure, generating one new oxygen vacancy to ensure charge neutrality:

$$C^{4-} \xrightarrow{TiO_2} Ti^{X}_{Ti} + C^{''}_{O} + V^{\cdot\cdot}_{O} \qquad \{3\}$$

However, oxygen vacancies can also be created by methods that do not involve doping. Several wet-chemical oxidation and reduction reactions have been shown to successfully generate oxygen vacancies in a wide range of products [135]. Additionally, annealing of nanomaterials in oxygen-deficient atmosphere has been found to generate oxygen vacancies in a simple and effective way [135]. This can be done in gases such as argon, nitrogen, or hydrogen, but as soon as the material is returned to ambient atmosphere, the oxygen in the air can react with some of the vacancies, thus removing them, showing that this is a reversible process [136].

Migration of oxygen vacancies

If an oxygen vacancy-containing material is exposed to an electric field, the positively charged vacancies will start to migrate towards the negatively charged cathode. This is expected to change the resistivity of the system, depending on what substrate the ferroelectric film is coated on. In 2019, Stanescu et al. found that substrates acting as "oxygen reservoirs", for example Nb-doped STO, result in a lower resistance state when a negative voltage is applied, while application of a positive voltage results in a higher resistance state [122]. The authors explain this by stating that when a negative voltage ($V < 0$) is applied, the oxygen vacancies start to move towards the sample surface. As the substrate acts as an oxygen reservoir, it can also provide oxygen vacancies if needed. Therefore, more and more vacancies can migrate towards the surface, eventually forming a conductive filament band. Now, if a positive voltage ($V > 0$) is applied, the oxygen vacancies will migrate towards and into the substrate again, resulting in the break-down of the conductive filament at the surface, and an increase in resistance, as shown in Figure 2.14a).

However, if the substrate does not act as an oxygen reservoir, e.g. for Pt-substrates, the oxygen reservoir must be some other place. This is typically the ambient air, and the system will now act in the opposite manner. Still, V > 0 causes oxygen vacancies near the surface to move towards the substrate, but in this case, this allows for new oxygen vacancies to be incorporated into the surface area when O_2 leaves the material. When enough vacancies have been incorporated, a conductive filament is formed, giving increased conductivity. For the opposite case, V < 0 drives oxygen vacancies towards the surface of the system, where they react with O_2 in the air, and are annihilated. As the substrate cannot provide any new oxygen vacancies, the concentration of vacancies will be reduced, thus breaking up the conductive filaments and increasing the resistance, as shown in Figure 2.14b).

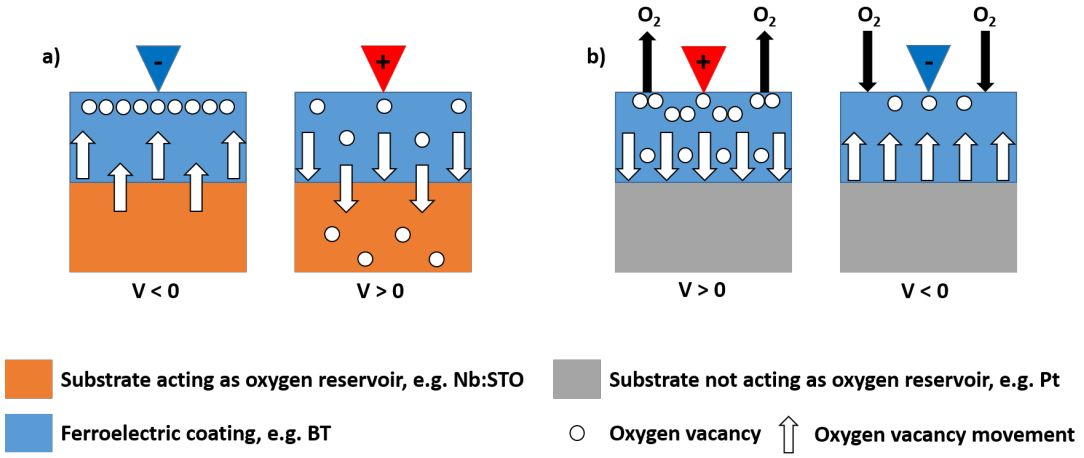

Figure 2.14: The migration of oxygen vacancies under positive and negative applied voltages for a) a substrate acting as an oxygen reservoir, where V < 0 generates a conductive filament band of oxygen vacancies, and b) a substrate unable to act as an oxygen reservoir, where V > 0 generates a conductive filament band of oxygen vacancies, based on information from Stanescu et al. [122]. Notice that in b), no oxygen vacancy migration across the coating-substrate interface is possible.

Oxygen vacancies have been the subject of many reports investing the degradation and lifetime of (multilayer) ceramic capacitors. Both Yang et al. [133] and Randall et al. [134] state that the electromigration of oxygen vacancies when the system is exposed to an electric field initiates a process which ultimately leads to the degradation of insulation resistance of the system. The authors of the former publication investigated a BT system more closely. In this case, they found that dopants and vacancies segregate at the grain boundaries during sintering, causing a space charge region to be developed in these areas. The development of this space charge region creates an electric barrier for further vacancy migration, which slows down the degradation process. At the same time, the region becomes depleted of electron carriers, thus increasing the resistivity at the grain boundaries. As an electric field is applied, the oxygen vacancies moves towards the cathode of the system, but as the grain boundaries act as barriers for migration, oxygen vacancies will pile up at the cathode-side of the BT grain. However, the barrier at the grain boundaries is not 100 % effective, allowing some leakage across the boundary. Therefore, as the oxygen vacancy content at the boundaries increases during the device's lifetime, the leakage currents will also increase, eventually causing device break-down. This is also the case at the electrode contact, where the pile-up of oxygen vacancies causes an increased conduction, eventually driving the preexisting non-Ohmic contact towards an Ohmic contact [133].

3 Experimental

Many of the experimental activities and procedures carried out in this Master's thesis are similar to those in its preceding project work, and major parts of Section 3.2 have therefore been reused from the project report [1]. However, some refinements have been done to clarify the procedure descriptions, and new descriptions have been made for activities that were not carried out in the project work.

3.1 Chemicals and apparatus

The only chemical required to produce the BT-coated Ti6Al4V samples, was a 0.13 M BT precursor solution, which was based on the work of Ræder et al. [16], and made during this thesis' preceding project work, as described in [1]. However, several apparatuses were used for the production and characterization of samples, as shown in Table 3.1.

Table 3.1: Apparatuses used for preparation and characterization of the BT films on the Ti-alloy substrates.

Apparatus	Manufacturer	Purpose
InfiniteFocus	Alicona	Imaging and topography measurements
Drop Shape Analyzer - DSA 100	Krüss	Contact angle measurements
LaboPol-21	Struers	Polishing of substrates
Plasma cleaner, Femto	Diener electronics	Plasma cleaning of substrates
Spin coater WS-400B-6NPP/LITE/AS	Laurell	Spin coating BT solution onto substrates
AccuThermo AW610	Allwin21 Corp.	Rapid thermal processing of samples
Da Vinci 1 D8 Advance Diffractometer	Bruker	XRD analyses
Helios NanoLab DualBeam FIB	FEI Company	Imaging of substrate-coating interface
MST Micro Scratch Tester	Anton Paar	Scratch tesing of coated substrates
LVFESEM, Zeiss Supra, 55VP	Zeiss	Low-resolution EDS mapping
Gold sputter Coater S150B	Edwards	Deposition of gold electrodes
Piezoelectric Evaluation System (aixPES)	aixACCT	dielectric measurements

3.2 Procedure

To investigate the effects of surface texture on the possibility of applying piezoelectric BT thin films on Ti6Al4V substrates, three main steps of experimental work had to be carried out. Firstly, the uncoated substrates were characterized in terms of surface texture and contact angle. Then, the coating was applied by a wet-chemical spin-coating process, where the applied solution had been prepared by an alcohol-free modified Pechini method. Finally, the coated samples were analyzed in terms of coating purity, degree of oxidation, adhesion, and surface texture. In the following, the procedures for each of these steps will be described in greater detail.

3.2.1 Characterization of uncoated Ti-alloy substrates

The textured samples that were investigated in this project were produced by Hermann Seitz' Microfluidics group at the University of Rostock, Germany, and are shown in Figure 3.1. Prior to texturing, all samples, sized approximately 10x10 mm, were polished, resulting

in the reference surface texture. Subsequently, surface texture was applied to an area of approximately 8x8 mm, leaving the parts closest to the edges identical to the reference sample. The textures were made by ultra-short pulse laser machining, and combinations of laser-induced periodic surface structures (LIPSS) and crossed patterns created by running the laser over exactly the same area over and over again (Grid), resulted in samples with a wide range of surface textures. These types of textures were chosen because it is known that cells adhere differently to different structures on different length scales [97]. Prior to the characterization, these samples were cleaned with ethanol in an ultrasonic bath for 5 minutes, before being patted dry with light-duty tissue wipers and stored in closed sample boxes.

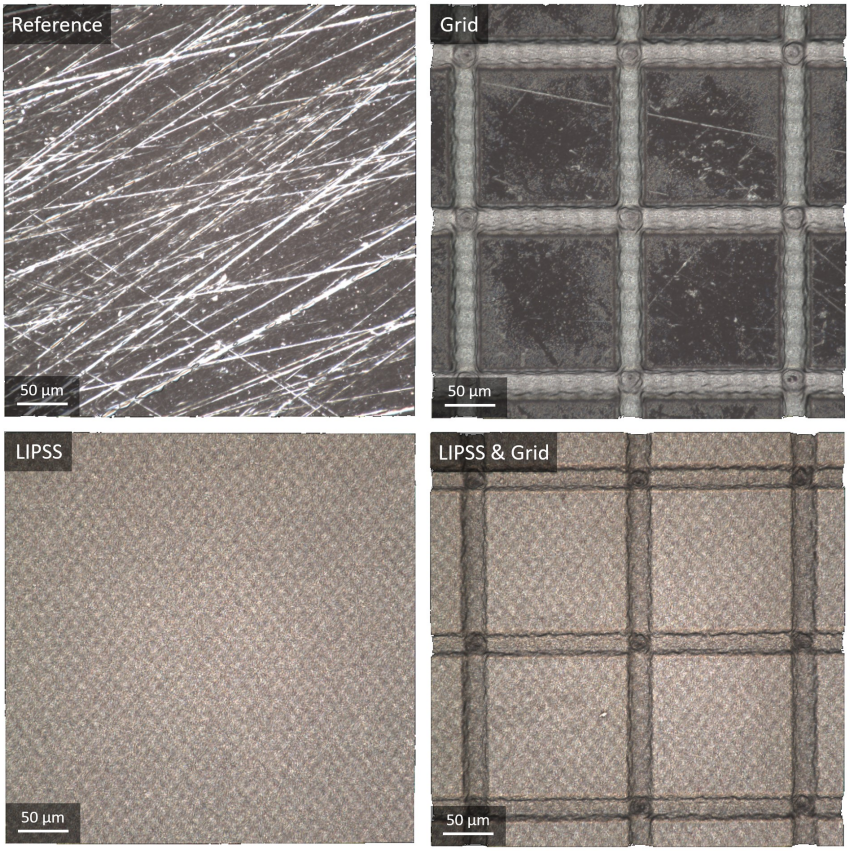

Figure 3.1: 408x408 µm example optical images of the substrates produced by Hermann Seitz' group in Rostock, Germany.

Surface texture

To be able to compare how the substrate texturing affects the possibility to coat the substrates, the surface textures of the substrates were investigated with an Alicona InfiniteFocus microscope. During imaging, a 50X magnifying objective lens was used, and 3D data sets of the surface topography in a 408x408 µm square were collected in a focus range of ±40 µm from the point where the sample surface was in focus. By processing these topography data sets, the imaging software was able to calculate the average area surface roughness for the samples in question. For these calculations, an automatic planar reference plane, based on the sample to be imaged, was applied. Furthermore, the area surface roughness calculations were carried out on areas without any obvious flaws, to

ensure that the results were representative for the entire sample. Thus, as mechanical processing typically results in a somewhat different texture close to the edges compared to the interior of the substrates, the areas closest to the edges of the samples were omitted.

To ensure that the intended substrate surface texture was not concealed during the coating process, the coated samples were once again investigated with the Alicona InfiniteFocus microscope. The procedure was identical to the investigations prior to coating, and made it possible to assess the impact of the coating procedure on the surface texture.

Contact angle measurements

To see how the substrate wettability was affected by the surface texture, the substrates were investigated with a Krüss DSA100 Drop Shape Analyzer. Each substrate was tested five times, with instrumental parameters as shown in Table 3.2, and the substrates were patted with a light-duty tissue wiper, and left to dry completely for approximately 20 minutes, between each test. In order to see how plasma cleaning affected the substrates, their wettability were investigated once again after being plasma cleaned.

Table 3.2: Instrumental parameters for contact angle testing.

Parameter	Value
Drop type	Sessile
Drop size	5 µL
Dosage rate	1 µL s^{-1}
Time of measurement	4 s after drop deposition
Temperature	25 °C
Drop liquid	Distilled water

3.2.2 Coating of BT solution onto Ti-alloy substrates

The process of coating the Ti6Al4V substrates with BT can be divided into four steps, as shown in Figure 3.2, namely plasma cleaning, spin-coating, drying, and rapid thermal processing. In the following, the experimental details regarding each of these steps are described in more detail.

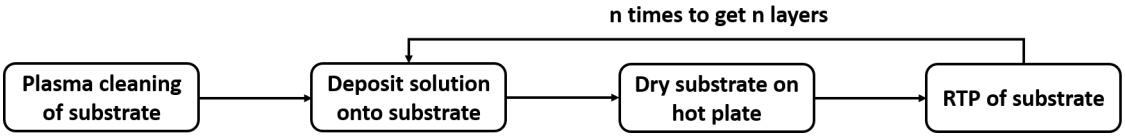

Figure 3.2: Flow-chart for spin-coating of substrates.

Plasma cleaning

In order to remove any surface impurities and dust which could negatively impact the film quality, and to improve the wettability of the substrates, the substrates were cleaned in a plasma cleaner prior to the spin-coating. The instrumental parameters for this process, carried out on a Diener Electronic Femto Plasma Cleaner, are shown in Table 3.3.

Table 3.3: Parameters for plasma cleaning of Ti6Al4V substrates.

Plasma type	Plasma Intensity	Generator Intensity	Time
O_2	50 %	50 %	1 min

Spin-coating and drying

The second step of the coating process was the spin-coating of the BT solution onto the substrate. Here, a syringe with a 0.2 µm filter tip was used to deposit a drop of 0.13 M BT solution onto the differently textured substrates. The BT solution was produced in the previous project work by an alcohol-free modified Pechini method, as described in [1], based on the work of Ræder et al. [16]. After deposition of the solution, the substrate was spun in a Laurell Spin Coater at 3500 rpm for 40 s, followed by a spin-down to 0 rpm over 10 s.

As the coating procedure was a batchwise process, the newly coated samples were immediately transferred to a hot plate, holding a temperature of 100 °C, while the remaining substrates in the batch were being coated. When all substrates had been coated, the temperature of the hot plate was raised to 180 °C, and the samples were heated for 5 min before being removed from the hot plate. This allowed for evaporation of water from the solution, and let the films set slightly prior to further processing.

Rapid Thermal Processing

The final step of the coating procedure was the heat treatment of the samples in an Allwin21 Corp. AccuThermo AW610 Rapid Thermal Processor (RTP). For the heat treatment of one coating layer, the heating chamber was firstly flushed with N_2-gas to remove any impurities, before the samples were heated to a maximum temperature of either 600 °C or 700 °C in air. The samples, still in air atmosphere, were then held at the maximum temperature for 6 min, before being cooled to room temperature, now in N_2-atmosphere to prevent further oxidation of the substrate. These heating programs are for simplicity abbreviated T600 and T700 respectively, and the heating parameters for each of these processes are presented in Table 3.4, with Figure 3.3 showing their heating profiles. When the final heating of the sample was finished, the solution deposition and heating process was repeated until nine layers of coating had been produced.

Table 3.4: Heating parameters for rapid thermal processing to 600 °C (T600)/700 °C (T700).

Step #	Step type	Step time [s]	End Temperature [°C]	Atmosphere
1	Delay	5	20	N_2
2	Ramp	360/420	600/700	Air
3	Steady	360	600/700	Air
4	Steady	No set time	20	N_2

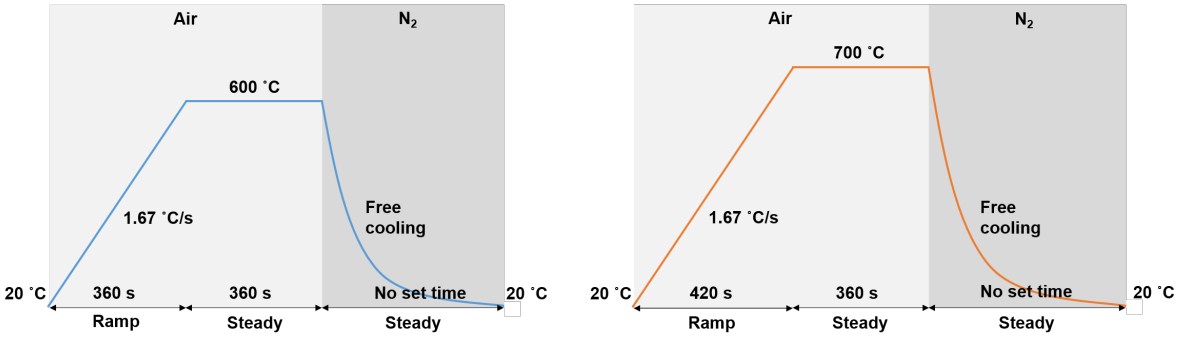

Figure 3.3: Temperature profiles for heating to a maximum temperature of 600 °C (T600, left) and 700 °C (T700, right). For both cases, the heating chamber was firstly flushed with N_2 (not included in figure), before a ramp step in air with a heating rate of 1.67 °Cs^{-1} to the maximum temperature. The samples were then held at maximum temperature in air for 6 min, followed by free cooling to room temperature in N_2-gas.

Optimization of heating procedures

In order to optimize the heating process, several heating procedures were tested, all of which were carried out on polished substrates. As the samples had to be heat treated after each solution deposition, it was possible to use different heating parameters for each layer of coating. Figure 3.4 and Table 3.5 provide an overview of these different combinations of heating programs that were tested, along with the abbreviations that will be used for them in the following. Note that the polished samples tested to optimize the heating programs will be named in the form of P_{H-X}, where X indicates the heating program.

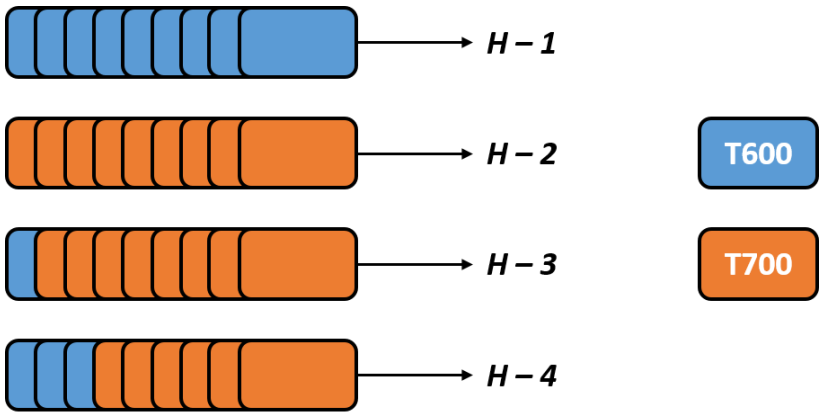

Figure 3.4: Temperature sequences tested for the heat treatment of 9-layered BT-coated Ti6Al4V substrates in the rapid thermal processing furnace. Each box represents the heating program for one layer of coating, with the blue and orange boxes representing T600 and T700 respectively.

Table 3.5: Explanation of the naming for the heating procedures.

Procedure	Explanation
$H-1$	All 9 layers heat treated with T600
$H-2$	All 9 layers heat treated with T700
$H-3$	First layer heat treated with T600, and last 8 layers heat treated with T700
$H-4$	First 3 layers heat treated with T600, and last 6 layers heat treated with T700

Coating of textured samples

For the coating of the textured samples, heating procedure $H-2$ was chosen. Once again, 9 layers of coating were deposited, with the same procedure as described for the optimization of the heating procedures. Additionally, one set of polished samples was only heat treated with procedure $H-2$, without applying any coating, to get an impression of the properties of the oxidation layer that develops on the substrate during heating. Table 3.6 provides an overview of the naming of the samples included in the final comparison.

Table 3.6: Naming of the different types of textured samples, where the polished samples were produced by the author at NTNU, and the rest of the samples were produced by Hermann Seitz' group at the University of Rostock, Germany.

Name	Explanation
P	Sample polished with 4000-grit SiC paper
R	Reference sample
L	Sample with LIPSS pattern
G	Sample with Grid pattern
LG	Sample with LIPSS & Grid pattern

3.2.3 Characterization of coated samples

After the substrates had been coated, the finished samples were analyzed by X-ray diffraction (XRD) to investigate phase purity of the coating, and by focused ion beam (FIB) imaging to investigate adhesion and oxidation of the substrate. Low-resolution energy-dispersive X-ray spectroscopy (EDS) was also carried out on the cross-section areas at the substrate-coating interfaces, in order to get a better overview of the elemental composition in these area. Additionally, some of the coatings were scratch tested to get a better measure of the adhesion, and they were investigated by optical microscopy to see if the substrate texturing was retained during coating. Finally, the dielectric properties of the samples were tested, to investigate if the coatings functioned as intended.

XRD of coating surface

In order to investigate the phase purity of the coating without getting too much signal from the substrate, Grazing Incidence XRD (GI-XRD) was used. This was carried out in a Bruker Da Vinci 1 D8 Advance instrument, with instrumental parameters as shown in Table 3.7. The recorded diffraction peaks were matched with known peaks in the PDF- 4+ database by using version 5.1 of the EVA-software.

Table 3.7: Parameters for GI-XRD.

Parameter	Value
Scan type	θ-2θ
Scan range	10.000-60.012°
Step size	0.028°
Steps	1800
Time/step	4.00 s
Incident angle	2.000°
Slit mode	Fixed
Anode	Cu

FIB-imaging of coating-substrate interface

To be able to investigate the coating-substrate interface, and thus reveal any crack formation or oxidation layer between coating and substrate, the samples were imaged in a Helios DualBeam Focused Ion Beam (FIB) instrument. During this process, a platinum protective layer was first deposited onto the sample, after which a cleaning cross section was made by the ion beam through the protective layer and into the substrate. Thus, by using the electron beam to look at the sample at a 52° angle, the inside wall of the milled cross-section could be imaged, revealing the interface layers. The instrumental parameters for these processes are shown in Table 3.8, while Figure 3.5 illustrates the different steps of the imaging process. Note that the length of the cross section area (L) depended on the type of cross section made, but for all cases, the length of the area for Pt-deposition (L+1) was 1 µm longer than the cross section itself.

Table 3.8: Parameters for the processes conducted during the Focused Ion Beam imaging, where "L" indicates the length of the cross section area.

Process type	Dimensions (xyz)	Beam type	Current	Voltage
Deposition of Pt	(L+1)x1x1 µm	Ion	93 pA	30 kV
Cleaning cross section	Lx4x2 µm	Ion	0.93 nA	30 kV
Imaging	Cross section area	Electron	0.17 nA	3 kV

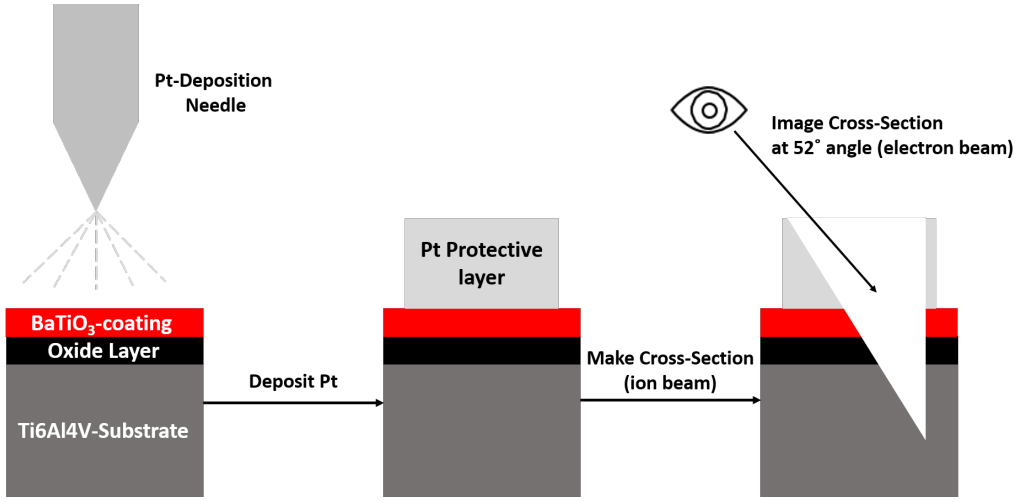

Figure 3.5: Schematic overview of the FIB-imaging process.

EDS of coating-substrate interface

In order to get a rough understanding of the chemical compositions of the different layers that were observed at the coating-substrate interface, EDS line scans were carried out with a Zeiss Supra 55VP LVFESEM instrument. The instrumental parameters for these investigations are shown in Table 3.9.

Table 3.9: Parameters for the EDS analysis of the coating-substrate interface.

Parameter	Value
Acceleration voltage	10 kV
Tilt angle	48°
Frames (scan repeats)	32
Resolution	27 nm
Dwell time	200 s

For a typical EDS line scan measurement, the line to be measured was set to start in the substrate area, and to go through the interface layers, before ending in the Pt-deposition layer. An illustration of this, together with an example of the typical results achieved from the line scan, is shown in Figure 3.6, where the red arrow indicates the length and direction of the EDS line scan. As can be seen, the typical elements detected were Pt, Ga, Ba, Ti, Al, V, and O, with characteristic X-ray energies as shown in Table 3.10. It should be noted that Ga and Pt does not originate from the substrate-coating itself, but from the FIB ion beam and Pt-deposition, respectively. Therefore, when displaying the EDS results in Section 4.3.4, these elements are omitted. Additionally, it can be seen that the lines for Ti and Ba are significantly higher than those of Al, V, and O. This is in general the case, as Ti is the main component of the substrate, and as the signals from Ti and Ba are overlapping. Thus, to be able to see the trends in the latter elements, these two groups of elements are separated and plotted in different graphs with different scales on the y-axes in Section 4.3.4.

Table 3.10: Characteristic X-ray energies for elements of interest in the EDS analysis.

Element	Characteristic energy [keV]
Ti	4.512 (Kα)
Al	1.486 (Kα)
V	4.953 (Kα)
O	0.525 (Kα)
Ba	4.466 (Lα)
Ga	1.098 (Lα)
Pt	2.050 (Mα)

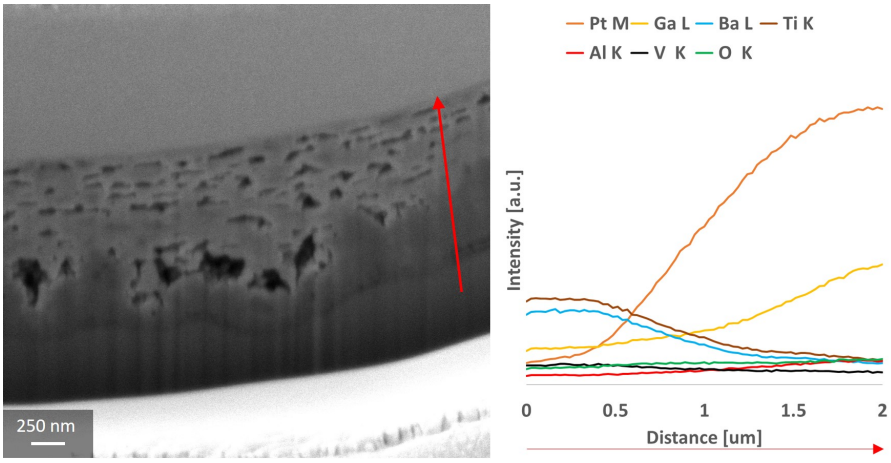

Figure 3.6: Example for typical EDS-measurement and corresponding results. The red arrow indicates the length and direction of the EDS line scan, while the labels of the graph reveals the type of elements detected, together with the detected energy series.

Scratch testing

As a part of the determination of the best heating procedure, investigations of the coating adhesion and strength were carried out by scratch testing. This was performed with a Anton Paar MST Micro Scratch Tester, with instrumental parameters as shown in Table 3.11. The required force for coating failure was determined optically, by locating the point on the scratch where its appearance changed drastically, as described in Section 2.5.2 and illustrated in Figure 3.7. Note that scratch testing was not carried out on the textured substrates, as it was expected that their differences in surface topography would have made the results incomparable.

Table 3.11: Parameters for scratch testing.

Parameter	Value
Scratch type	Progressive
Load range	30 - 25 000 mN
Scratch length	3 mm
Scratch rate	1 mm min^{-1}

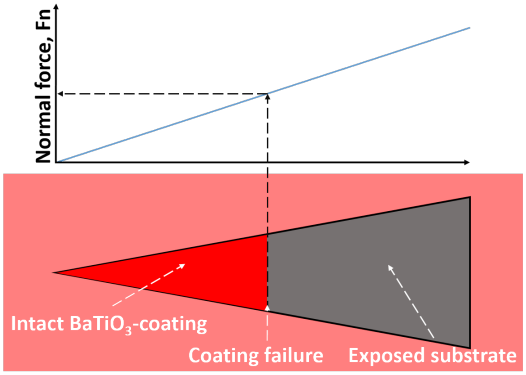

Figure 3.7: Illustration of the point of coating failure for a progressive scratch test: The abrupt color change indicates coating failure/delamination, and the corresponding force can be found graphically.

In order to investigate the scratched samples, as well as to see how the coating behaved in different regions of the scratch, the Helios DualBeam Focused Ion Beam (FIB) instrument was utilized. This made it possible to do surface imaging of the scratches, where the areas close to the scratches were especially interesting, as these areas had been exposed to the highest amount of stress. Furthermore, by milling out a cross-section as described in the previous section on FIB, it was possible to determine whether or not the coating was present at different points of the scratch. By doing this, the failure type and thus some broad characteristics of the films could be determined.

Dielectric testing

For the determination of the dielectric properties of the BT coatings, dynamic hysteresis measurements (DMH) were performed with an aixACCT Piezoelectric Evaluation System (aixPES), using the thin-film mode (TF-SHU). These measurements resulted in polarization curves, and were carried out both for the set of samples used to determine the best heating sequence, and for the coated textured samples, as well as a polished sample that was solely oxidized. Prior to this, circular gold top-electrodes were deposited on the coated samples by an Edwards S150B Sputter Coater. In order to make the electrodes evenly sized and sufficiently small, the sample was placed in the sputter mask displayed in Figure 3.8. For the DMHs, the measurements were carried out top-to-top between two different gold electrodes for all tested samples, as shown in Figure 3.9a). Additionally, for the textured samples, the DMHs were carried out top-to-bottom between a gold electrode and a corner of the substrate where the coating had been scratched off as well, as shown in Figure 3.9b), to investigate if this affected the polarization curves. The input parameters for these measurements, both in terms of electrode geometry and for the hysteresis measurements, are shown in Table 3.12.

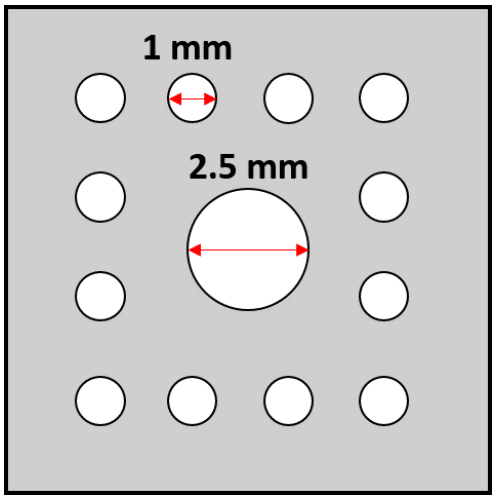

Figure 3.8: Sketch of the mask used for sputtering. The small holes have a diameter of 1 mm, while the large center hole has a diameter of 2.5 mm. Note that only the smallest electrodes were used in the dielectric measurements.

Table 3.12: Instrumental parameters used for dielectric testing. Here, "Film thickness" refers to the input parameter in the software, and, for the measurements carried out top-to-top, represents two times the actual BT film thickness.

Parameter	Value
Type	Dynamic Hysteresis Measurement
Waveform	Triangle
Loop type	Single
Film thickness (top-to-top)	2 times the total (coating + oxide) thickness
Film thickness (top-to-bottom)	Total (coating + oxide) thickness
Electrode area	0.785 mm^2 (D = 1 mm)
Frequency	100 Hz
Amplitude	1 V

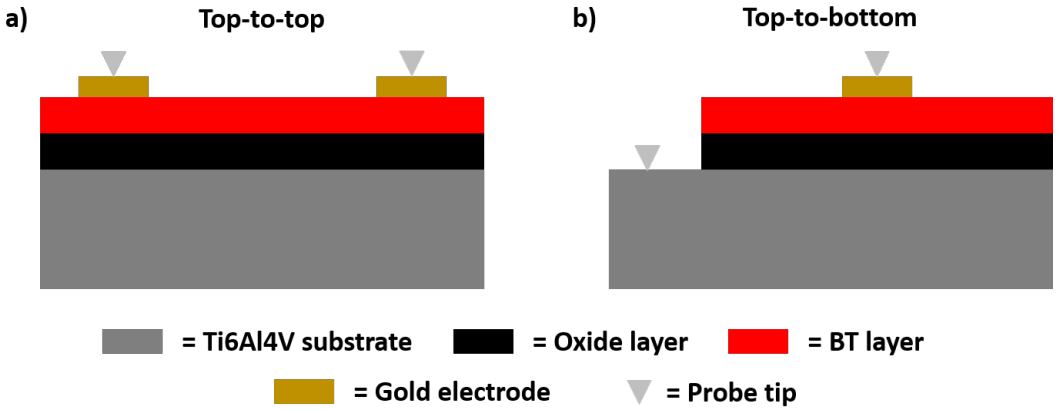

Figure 3.9: Schematic illustration of the experimental configuration for dielectric measurements: a) Top-to-top, and b) top-to-bottom.

Some general comments should be made regarding the input parameter "Film thickness", which describes the thickness of the dielectric coating that is measured. For the system investigated in this work, both the BT coating and the oxide layer that develops on the Ti6Al4V substrate are dielectric, and it is the total thickness of these two layers that has to be fed to the software. Furthermore, when measuring top-to-top, the current has to pass this combined layer on the way down from the first gold electrode to the substrate, and once again on the way up from the substrate to the second gold electrode. Therefore, for top-to-top measurements, the input thickness corresponds to two times the actual combined thickness of the coating and oxide layer. However, for top-to-bottom measurements, the current only passes through the coating and oxide layers once, making the input thickness the same as the actual combined thickness of the coating and oxide layer. When deciding the exact input parameters for the thickness, the substrate-coating interface region of the samples in question were investigated in the FIB. For the measurements on the polished samples treated with the different heating programs, this was quite easy, and the values are shown in Figure 4.10 in Section 4.2.2. However, for the textured samples treated with heating program $H-2$, the film thickness varied greatly. Therefore, it was assumed that the combined thickness of the coating and oxide layer on the textured samples corresponded to that found for the polished sample treated with heating program

$H-2$. Some errors are therefore expected when it comes to the values for the electric field, which depend on the coating thickness. Additionally, for the top-to-top measurements, the measured electric fields and polarization values depend on the spacing between the different electrodes. A model to compensate for this effect have been made for an interdigitated electrode configuration [16], but not for the top-to-top configuration, and the recorded values in this work are therefore approximations.

To investigate the influence of oxygen vacancies on the dielectric behaviour, more tests were carried out on sample P_{H-3}. To do this, the sample was annealed in N_2-gas at 400 °C for 4 h, according to Figure 3.10, before its dielectric properties were tested again as described above.

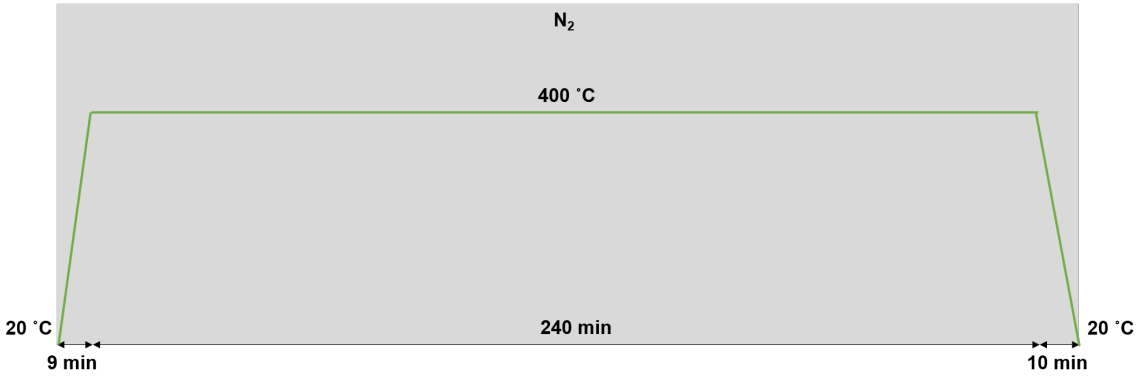

Figure 3.10: Temperature program used for the annealing process in N_2-gas: 9 min ramp time from room temperature to 400 °C, where the sample was held for 4 h, before 10 min cooling time to room temperature again.

3.2.4 Sample overview

To summarize the experimental activities, Table 3.13 provides an overview of all samples and the tests that were carried out on them.

Table 3.13: Overview of samples and experimental activities: See Tables 3.5 and 3.6 for explanation of the sample names. Here, GI-XRD refers to grazing incidence X-ray diffraction, FIB refers to focused ion beam milling and imaging, DMH refers to electric dynamic hysteresis measurements, and EDS refers to energy-dispersive X-ray spectroscopy.

Sample	**Test(s)**
P_{H-2} (uncoated)	GI-XRD, FIB, DMH, EDS
P_{H-1} (coated)	GI-XRD, FIB, Scratch, DMH
P_{H-2} (coated)	GI-XRD, FIB, Scratch, DMH
P_{H-3} (coated)	GI-XRD, FIB, Scratch, DMH, Annealing in N_2 and repeat of DMH
P_{H-4} (coated)	GI-XRD, FIB, Scratch, DMH
R-1 – R-4 (uncoated)	Surface roughness, Contact angle before and after plasma cleaning
R-1 – R-3 (coated)	Surface roughness, GI-XRD
R-1, R-3 (coated)	FIB, EDS
R-2 (coated)	DMH
G-1 – G-4 (uncoated)	Surface roughness, Contact angle before and after plasma cleaning
G-1 – G-3 (coated)	Surface roughness, GI-XRD
G-1, G-3 (coated)	FIB, EDS
G-2 (coated)	DMH
L-1 – L-4 (uncoated)	Surface roughness, Contact angle before and after plasma cleaning
L-1 – L-3 (coated)	Surface roughness, GI-XRD
L-1, L-3 (coated)	FIB, EDS
L-2 (coated)	DMH
LG-1 – LG-4 (uncoated)	Surface roughness, Contact angle before and after plasma cleaning
LG-1 – LG-3 (coated)	Surface roughness, GI-XRD
LG-1, LG-3 (coated)	FIB, EDS
LG-2 (coated)	DMH

4 Results

4.1 Properties of uncoated substrates

In order to properly discuss and draw conclusions from the results regarding the optimization of the heating programs and the spin-coating of the textured samples, it is important to have an insight into the properties of the uncoated substrates themselves. Therefore, in the following, properties of the uncoated substrates that directly affect the coating procedure will be assessed, and results that provide a base line for further investigations will be presented.

4.1.1 Surface roughness and wetting of textured substrates

As a part of the investigation of the substrate surface roughness and texture, all of the textured substrates were investigated by optical microscopy. The obtained topography height profiles of the samples within each texture group were nearly identical, and therefore, only a representative example of each sample set is shown in Figure 4.1. This figure clearly reveals the polishing stripes in sample R and the flat areas of sample G, while the LIPSS pattern on samples L and LG have concealed these distinct marks. On sample L, the LIPSS treatment has made a pattern of diagonal lines, where the height profile varies periodically between ±200 nm. Furthermore, the grid lines on samples G and LG are clearly visible, and an extra deep well can be observed at the intersection of the grid lines.

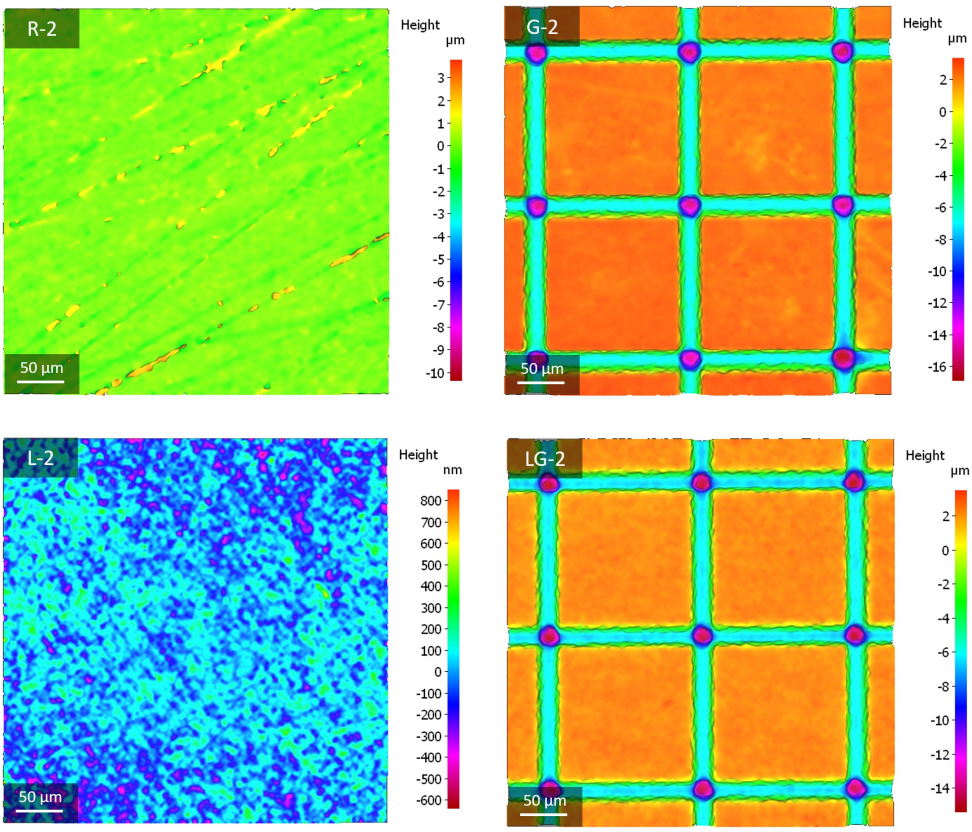

Figure 4.1: Topography height profiles of a selection of uncoated substrates.

After collecting 3D datasets of the topography height profiles of the textured substrates, the area surface roughness of the substrates was calculated using the imaging software. For each texture group, four substrates were analyzed, and the resulting average area surface roughness values, *Sa*, are shown in Figure 4.2. Also included in this figure is the surface roughness information provided by Hermann Seitz' Microfluidicis group in Rostock, who manufactured the textured substrates. This makes it possible to address both differences in the analyses, and the reproducibility of the results. It can be observed that the R and L samples have the lowest area surface roughness, while the grid pattern on samples G and LG results in a significantly higher area surface roughness. Furthermore, the analyses of the uncoated samples at NTNU are very similar to those of the Rostock group for samples G, L and LG, while the NTNU-value for sample R is approximately 4 times larger than that measured in Rostock.

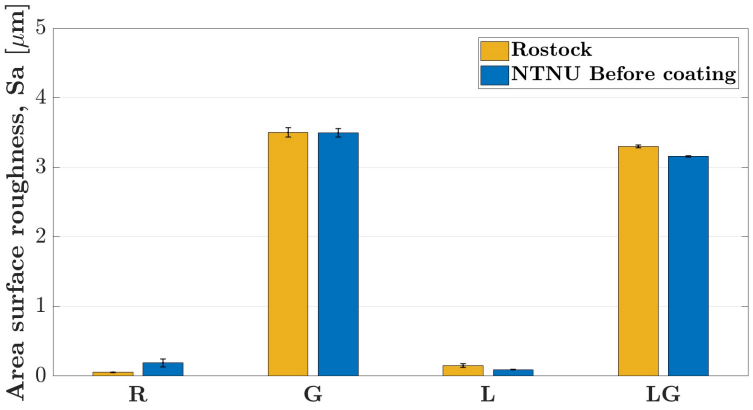

Figure 4.2: Comparison of area surface roughness values of uncoated samples, measured in Rostock (yellow) and by the author at NTNU (blue).

In order to assess the wetting properties of the textured metal substrates, contact angle measurements were carried out. For each sample, five drops of distilled water were deposited, and the resulting averages and standard deviations are shown in Figure 4.3. This figure also shows how the contact angle changed after plasma cleaning, which is the wetting-enhancing step at the start of the spin-coating procedure. Here, it should be noted that the plasma cleaning slightly improved the wetting for sample groups R and L, while the wetting was improved significantly for sample groups G and LG.

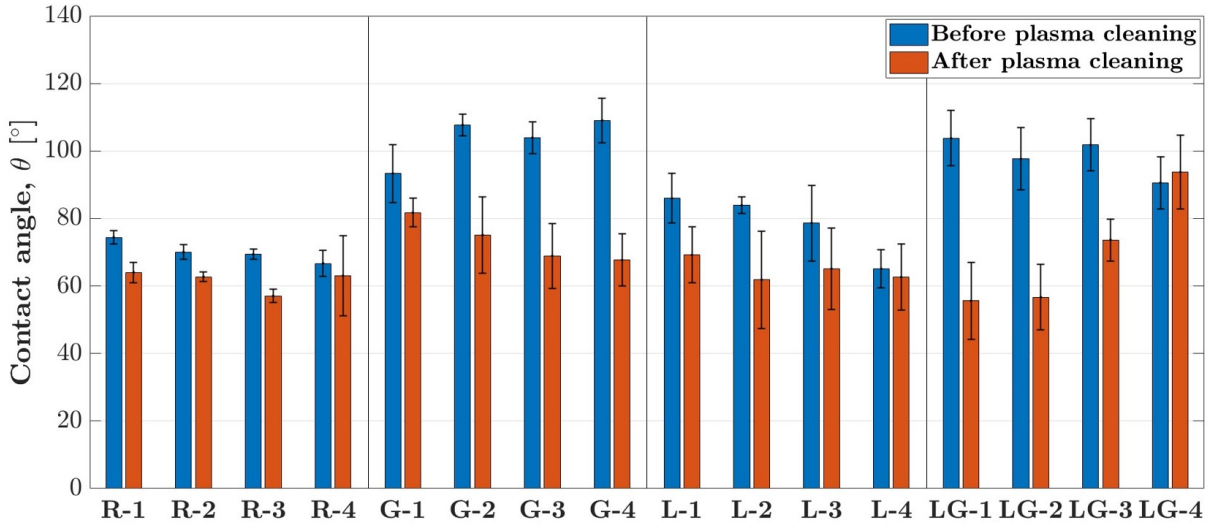

Figure 4.3: Contact angle measurements on each of the textured samples before (blue) and after (orange) plasma cleaning.

The contact angle measurements for the individual samples were used to calculate average values for each of the texture groups. These results are shown in Figure 4.4, together with contact angle measurements received from Rostock, once again making it possible to assess the reproducibility. The samples from Rostock were not plasma cleaned, and comparisons must therefore be made with the NTNU-results before plasma cleaning. By doing this, a good match between these measurements for all texture groups, except for group R, is revealed. This figure also emphasizes the observations from Figure 4.3, that the plasma cleaning slightly improved the wetting of samples R and L, while it significantly improved the wetting of samples G and LG. The improved wetting for samples G and LG corresponds nicely with what was observed visually during the contact angle measurements: Directly after drop deposition on plasma cleaned samples G and LG, the contact angle was rather large, but after approximately 2 s, the drop started to spread, resulting in the reduced contact angle seen in Figures 4.3 and 4.4.

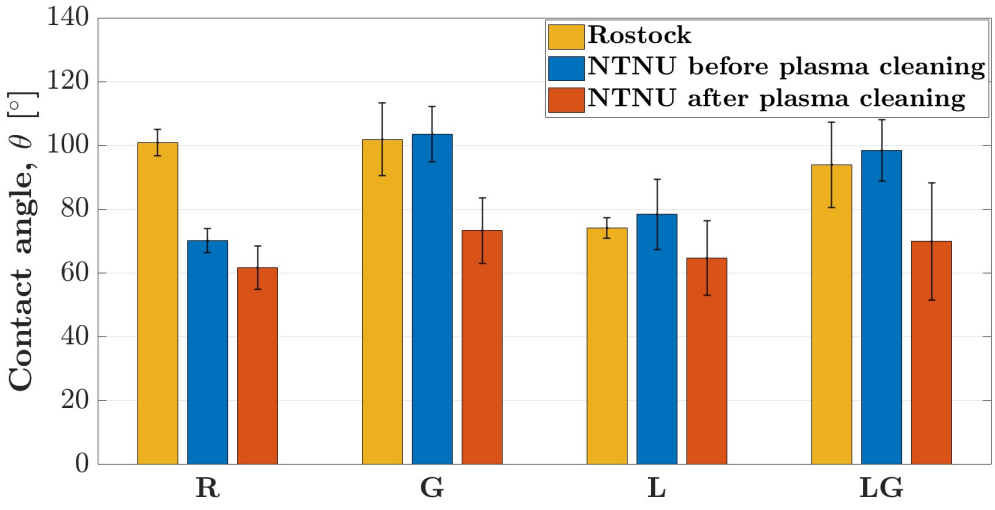

Figure 4.4: Contact angle measurements of the different texture groups carried out in Rostock (yellow, not plasma cleaned), and at NTNU before (blue) and after (orange) plasma cleaning.

4.1.2 Heat treatment of an uncoated, polished substrate

As described in Section 3.2.2, a polished, uncoated substrate was heat treated with heating program $H-2$, and subsequently investigated, in order to get a better understanding of how the substrate itself behaves upon heating. An important step in this investigation was to image the oxide-substrate interface, in order to determine the thickness and the microstructure of the oxide layer. To do this, a cross-section was made in the FIB, as described in Section 3.2.3, but instead of using the "standard cross section depth" of 2 µm, the depth was set to 4 µm. In that way, it was possible to reveal the entire oxide layer, as shown in Figure 4.5. The oxide layer resulting from the heat treatment was found to be quite thick (700 nm), and it contained some pores close to the oxide-substrate interface. Furthermore, dark speckles can be observed evenly distributed through the oxide layer, indicating the presence of some secondary phase. The same figure also reveals the surface topography of the oxide layer, which has a rough appearance.

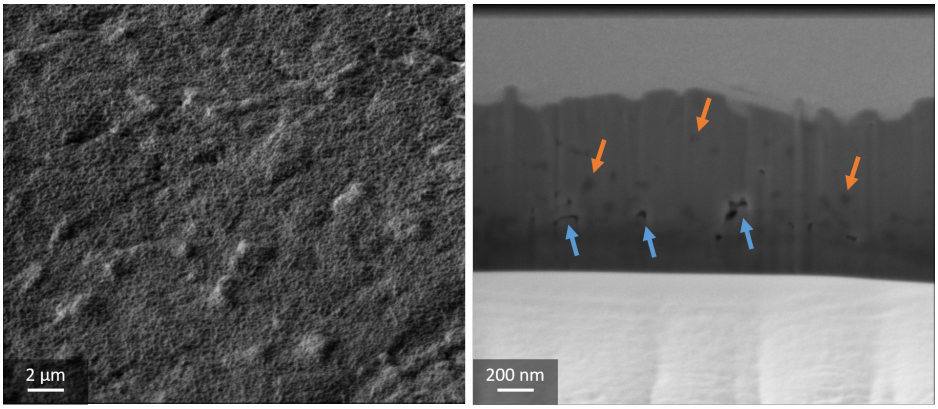

Figure 4.5: Image revealing the surface topography and the oxide-substrate interface of a polished, uncoated sample, after heating the substrate with heating program $H-2$. The blue arrows point towards some of the pores, while some of the dark speckles are indicated by the orange arrows.

GI-XRD was carried out to investigate the effect of heating on the Ti6Al4V substrate, as this could reveal whether or not secondary phases were present in the samples. The results, revealing the effect of heating to a maximum temperature of 600 °C once (T600), to a maximum temperature of 700 °C once (T700), and to a maximum temperature of 700 °C nine times ($H-2$), are shown in Figure 4.6. From the rutile and anatase peaks present in this figure, it is clearly seen that some oxidation occurs for all of the samples, but significantly less for the sample treated with T600 once. As the maximum temperature is increased to 700 °C, the peaks corresponding to the rutile phase become more prominent, and the sharpness of these rutile peaks increases when heat treated nine times. The small peak at approximately 2θ = 25° indicates the presence of some anatase, but it is clear that rutile is the dominating TiO_2 polymorph. Note that there is some mismatch between expected and actual peak position, especially in the range of 2θ = 35-45°. This is most likely a sample displacement error originating from imperfect mounting of the samples, and is therefore not related to the differences in heat treatment.

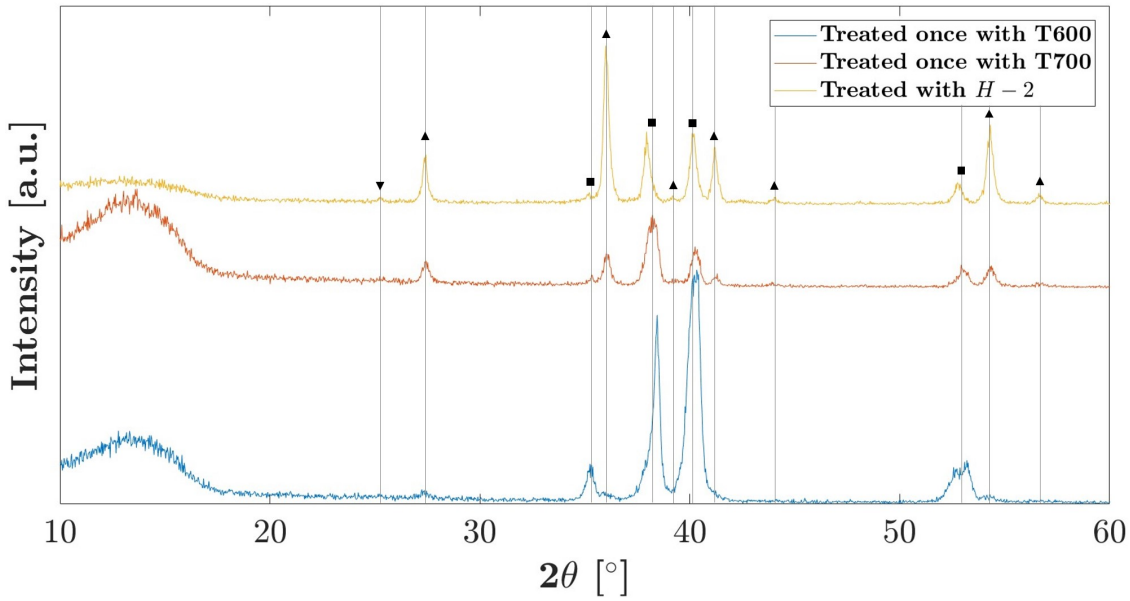

Figure 4.6: Measured GI-XRD diffractograms for uncoated, polished samples treated once with heating program T600 or T700. The peak are marked with: (■) for Ti10Al4V (PDF 04-002-8708, best replacement for Ti6Al4V), (▲) for the rutile polymorph of TiO_2 (PDF 04-003-0648), and (▼) for the anatase polymorph of TiO_2 (PDF 00-021-1272).

To be able to distinguish the dielectric behaviour of the coating and the oxidized substrate itself, polarization curves were measured at 1 V and 100 Hz on the oxidized substrate, as described in Section 3.2.3. A typical example of these curves is shown in Figure 4.7, and reveals that no ferroelectric polarization response is observed for the oxidized substrate.

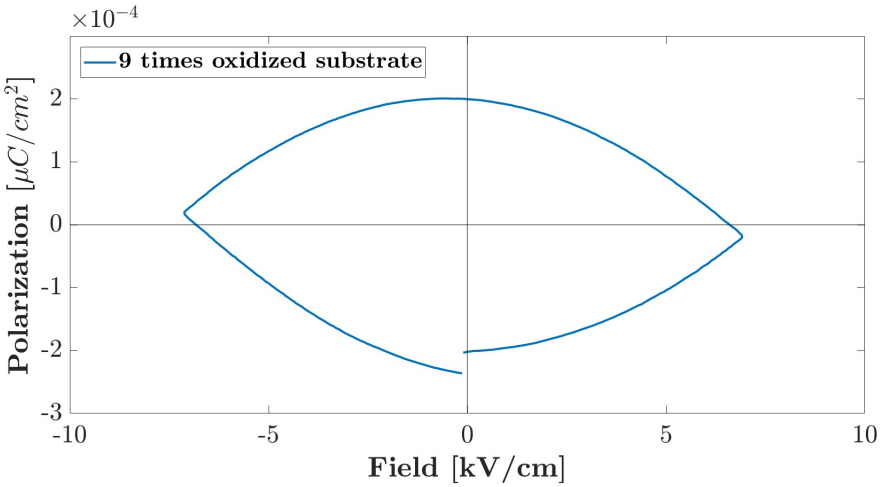

Figure 4.7: Typical polarization curve for a polished sample that subsequently has been heat treated nine times with heating program $H-2$, measured top-to-top at 1 V and 100 Hz.

4.2 Optimization of the heating program

Before spin-coating the textured substrates, investigations were made in order to decide what temperature program resulted in the best compromise between coating properties

and substrate degradation. For that, polished substrates were spin-coated and treated with four different heating programs, and the resulting samples were analyzed in terms of phase purity, adhesion, appearance of coating-interface region, and dielectric properties. In the following, these results will be presented, before a conclusion on the best temperature program will be made.

4.2.1 Phase purity

For the assessment of phase purity, crystallinity and substrate oxidation, all of which are important factors for the final quality of the coating, GI-XRD was carried out on the coated samples treated with the different heating programs, as described in Section 3.2.3. The results of this procedure are shown in Figure 4.8, and reveal that all of the heating programs resulted in some detectable substrate oxidation. However, the degree of oxidation appears to be highly dependent on the type of heating program used. For the sample treated with the lowest maximum temperature, i.e. program $H-1$, almost no traces of the rutile phase could be observed, while the samples treated with the three remaining heating programs display clear rutile peaks, indicating a significantly higher degree of oxidation. Of the three samples that at some point were heated at a maximum temperature of 700 °C, the sharpness and the relative intensity of the rutile peaks compared to the primary BT peak is highest for the sample treated with heating program $H-3$, while samples P_{H-2} and P_{H-4} show diffractograms that closely resemble each other. Additionally, the diffractograms for all of the samples show that the desired BT phase has been formed, but the peak sharpness is generally higher for the samples heated at the highest temperatures, with sample P_{H-2} showing the sharpest peak. This is a clear indication of improved crystallinity and a more complete BT-forming reaction, which in practice rules out heating program $H-1$ as a candidate for the best heating program.

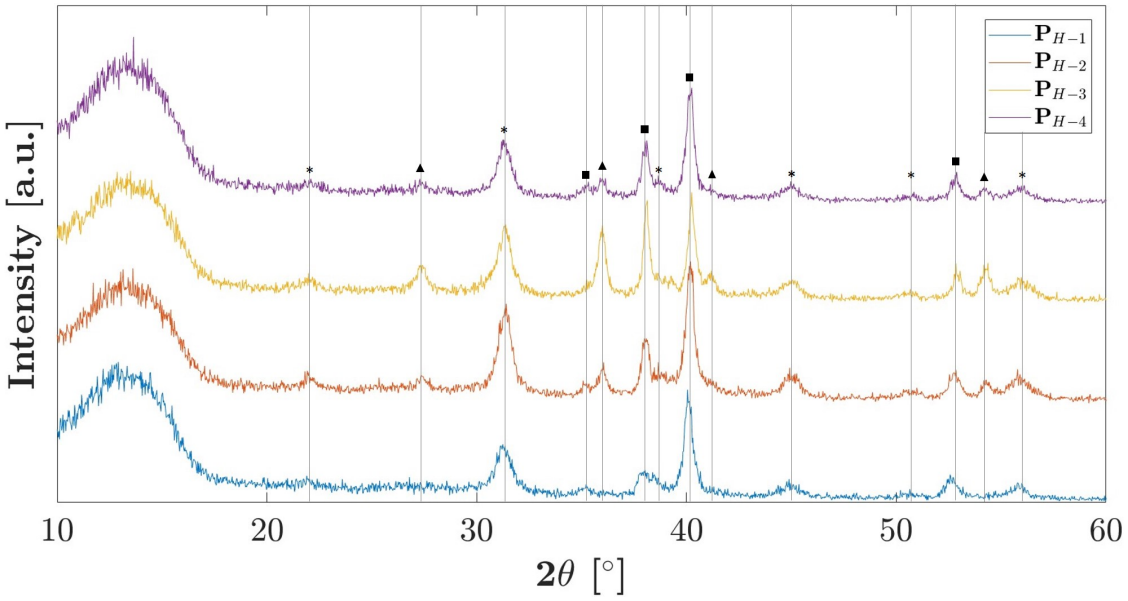

Figure 4.8: Measured GI-XRD diffractograms for coated, polished samples treated with the different heating programs. The peak are marked with: (*) for $BaTiO_3$ (PDF 04-012-8127), (■) for TiAl10V4 (PDF 04-002-8708, best replacement for Ti6Al4V), and (▲) for the rutile polymorph of TiO_2 (PDF 04-003-0648).

4.2.2 Substrate-coating interface

Another important parameter for the decision on the best heating program was the adhesion between substrate and coating. Therefore, to investigate this, cross-sections revealing the substrate-coating interface were made by using FIB. The resulting cross-section images at 25000X magnification are shown in Figure 4.9. Here, four distinct layers can clearly be seen: The bottommost Ti6Al4V layer, followed by a TiO_2 reaction layer, the BT coating, and finally the Pt protective layer, as indicated on sample P_{H-2}. From this figure, it is observed that heating sequence $H-1$ results in a dense film, but with cracks running along the interface. Heating sequence $H-2$ results in a mostly dense film with no cracks, but with some pores, while $H-3$ results in a highly porous interface region. Finally, heating sequence $H-4$ results in a porous film, where the pores are connected, giving cracks at the coating-substrate interface.

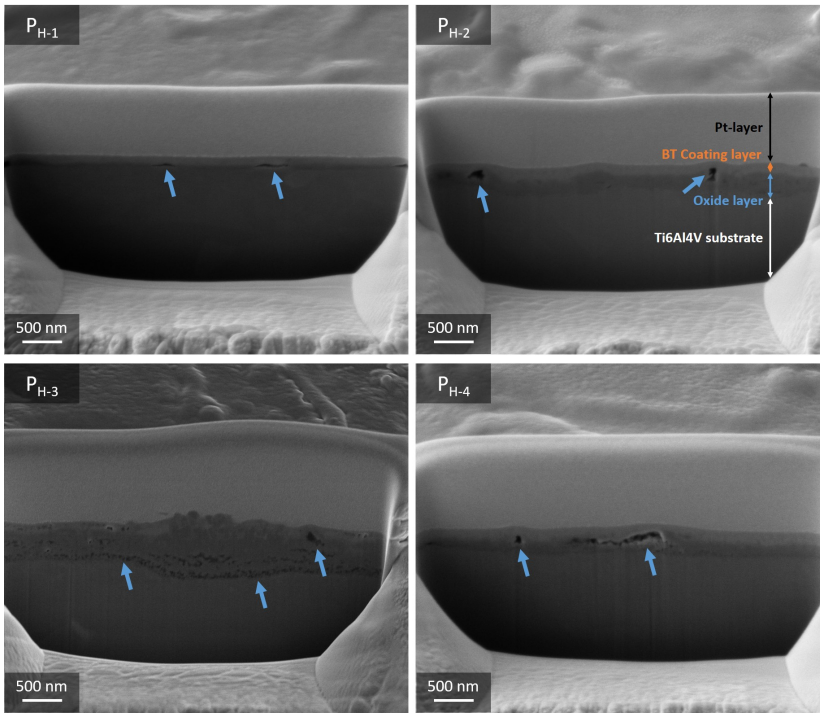

Figure 4.9: FIB-images of the coating-substrate interface on sample P, showing the effect of the different temperature programs. The different layers are indicated on sample P_{H-2}, while blue arrows point at important features in the images.

In order to investigate how the final thickness of the BT coating and of the TiO_2 reaction layer was affected by the heating sequence, and thus obtain a quantification of the degree of oxidation, FIB images of the coating-substrate interface at five different locations were captured. The layer thicknesses were measured directly from the images, and the results of this procedure are shown in Figure 4.10. These results indicate that the thickness of the BT coating is constant and independent of heating sequence, while the opposite is true for the thickness of the TiO_2 layer. The measurements show that the TiO_2 layer is thinnest for heating sequence $H-1$, and thickest for heating sequence $H-3$, while sequences $H-2$ and $H-4$ result in an intermediate thickness, which corresponds nicely with what can be seen in Figure 4.9.

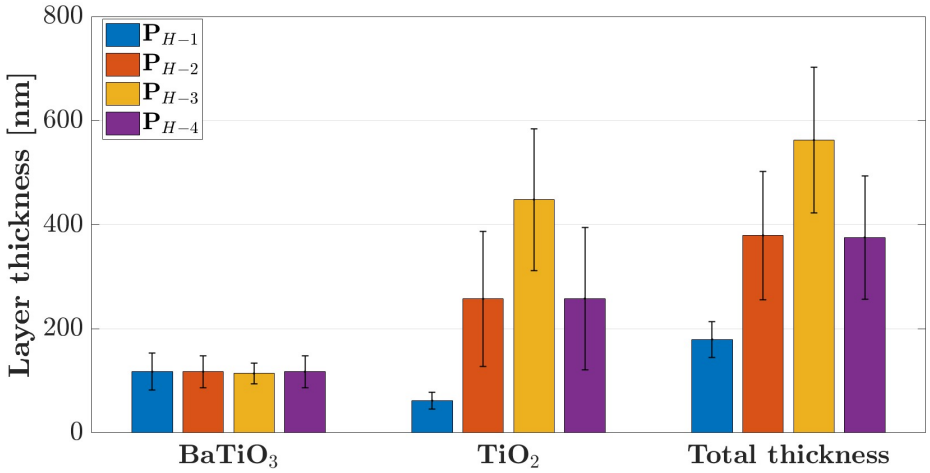

Figure 4.10: Thicknesses of the BT and TiO_2 layers for the different heating sequences.

4.2.3 Scratch testing

Further investigations of how the heating programs affected the coating adhesion were carried out by performing progressive scratch tests on the polished, coated samples. For this, five scratches were made on each of the four samples, and the point of coating delamination was determined optically, as described in Section 3.2.3. The average coating strength in terms of observed applied normal force at the point of coating delamination are shown in Figure 4.11, indicating that heating programs $H-2$ and $H-4$ result in the best adhesion. However, it should be noted that the coating strengths varied greatly from scratch to scratch on the same sample, as indicated by the large standard deviations in the measurements. Additionally, the actual process of optically defining the exact point where delamination occurred was challenging, further adding to the uncertainty of these results. Thus, the results for determining what heating program is the best in terms of coating adhesion were inconclusive.

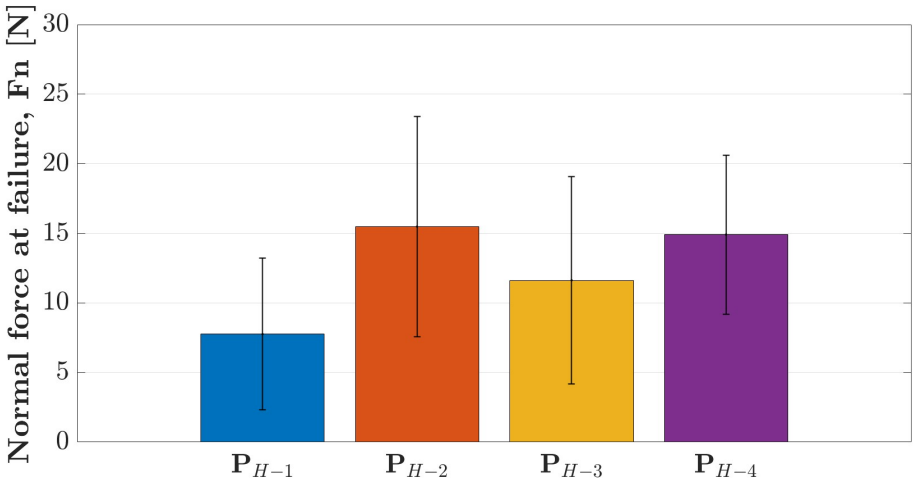

Figure 4.11: Average normal force at failure for scratch tests on coated, polished samples treated with the different heating programs.

Closer investigations of the scratches were made in the FIB-instrument, as described

in Section 3.2.3. For all of the four heating programs, surface images were made at the beginning of the scratch, where the scratching force was quite low, as well as at the end of the scratch, where the scratching force was at its highest. Furthermore, images revealing the coating-substrate interface inside the scratch trajectory were captured at points close to the beginning and close to the end of the scratch, to reveal whether or not the coating was still present. Firstly, the images taken of sample P_{H-1} are presented in Figures 4.12 and 4.13. Figure 4.12a) reveals some fine crack lines early in the scratch path, indicating that even a weakly applied force is sufficient to cause coating failure. From the images of the end of the scratch, shown in Figure 4.12b) and c), it is clear that the indenter has penetrated into the substrate with a depth that exceeds the coating dimension by a large margin, and pushed residue material in front and to the sides of itself. However, as can be seen from Figure 4.13, the coating has not been completely peeled off, most likely due to it being pushed into the underlying substrate by the indenter as the normal force increases. Looking at the edges of the scratched area, little to no cracking appears to extend from the scratch and out towards the surrounding coating, implying that the fracture toughness of the coating is high.

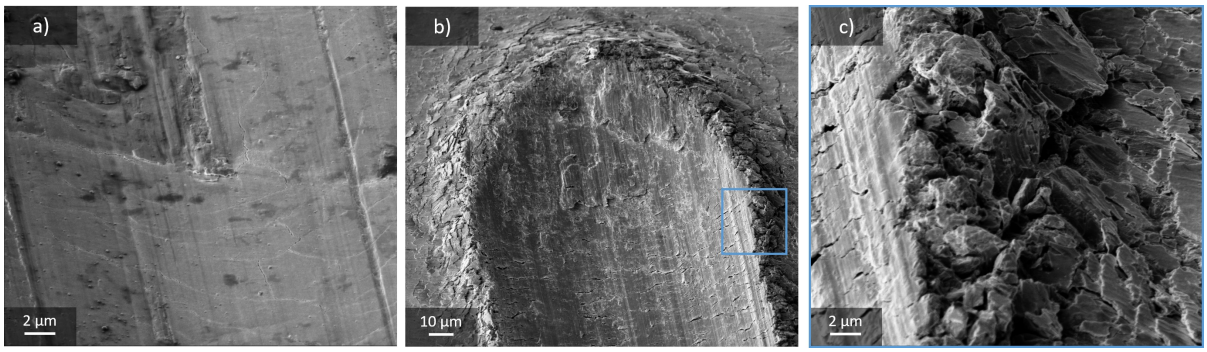

Figure 4.12: Surface images of different positions along a scratch mark on a polished coated sample, treated with heating program $H-1$: a) 5000X image from the beginning of the scratch, b) 800X overview image of the scratch end, and c) 5000X image of the area inside the blue frame in figure b).

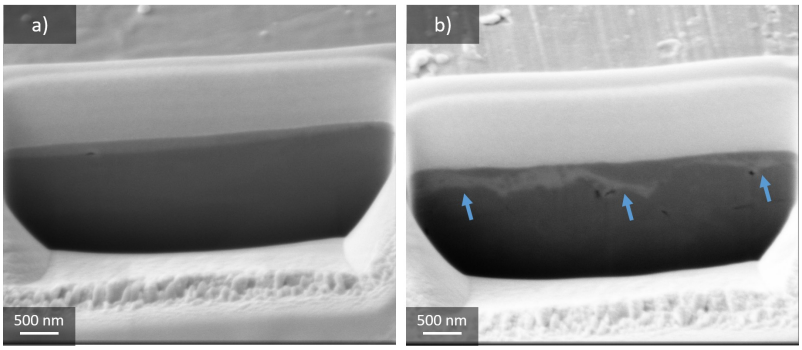

Figure 4.13: Interface images at 25000X at different positions of a scratch mark on a polished coated sample, treated with heating program $H-1$: a) at the beginning of the scratch, and b) at the end of the scratch. The blue arrows point at coating that has been pushed into the underlying substrate by the indenter.

Figures 4.14 and 4.15 reveal the surface- and interface regions of the sample heat treated with heating program $H-2$. Unlike for sample P_{H-1}, no visible cracks can be seen in the beginning of the scratch trajectory in Figure 4.14a), but instead, some discoloration can be observed, possibly indicating coating delamination already at this point. As for sample P_{H-1}, the end of the scratch, shown in Figures 4.14b) and c), appears to reveal a bare substrate, with little to no cracks extending from the scratch edges. In this case, the bare substrate is confirmed by looking at the coating-substrate interface, where the bright coating layer present at the beginning of the scratch (Figure 4.15a)) has been completely removed at the end of the scratch (Figure 4.15b)). It should be noted that also the oxide layer underneath the coating layer has been removed during scratching, making it difficult to determine whether it is the coating-oxide adhesion or the oxide-substrate adhesion that has been the reason for the delamination.

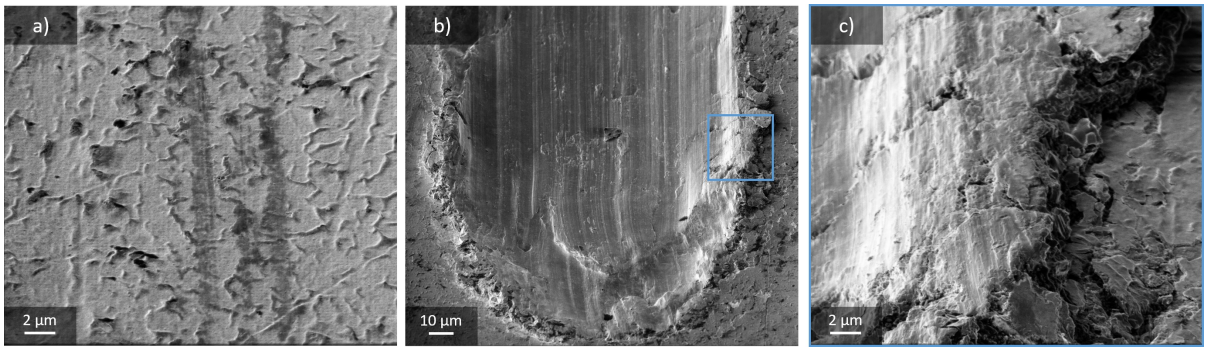

Figure 4.14: Surface images of different positions along a scratch mark on a polished coated sample, treated with heating program $H-2$: a) 5000X image from the beginning of the scratch, b) 800X overview image of the scratch end, and c) 5000X image of the area inside the blue frame in figure b).

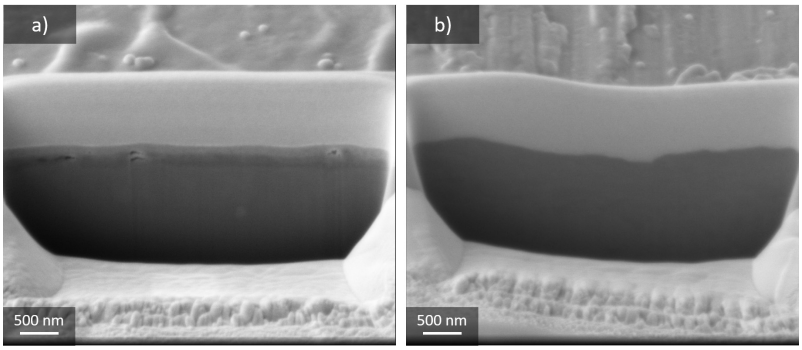

Figure 4.15: Interface images at 25000X at different positions of a scratch mark on a polished coated sample, treated with heating program $H-2$: a) at the beginning of the scratch, and b) at the end of the scratch.

The surface- and interface images of sample P_{H-3} are shown in Figures 4.16 and 4.17, and display many of the same features seen for sample P_{H-2}. Once again, some discoloration can be seen in the beginning of the scratch path (Figure 4.16a)), while the scratch end reveals a bare substrate (Figure 4.16b)) with little to no crack spreading (Figure 4.16c)). In this case, the interface image captured at the beginning of the scratch, shown in Figure 4.17a), reveals the presence of a darker layer above parts of the brighter coating layer. This implies

that some impurities, possibly present on the indenter from previous scratches, have been deposited on top of this area of coating during scratching. Also this time, the interface image of a cross-section towards the end of the scratch (Figure 4.17b)) reveals that both the oxide- and the coating layer have been removed from the substrate, confirming that only a bare substrate is left behind.

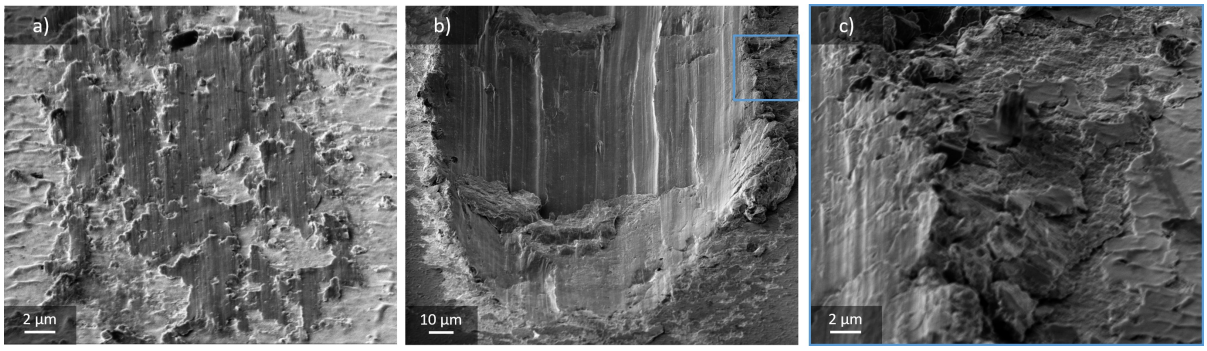

Figure 4.16: Surface images of different positions along a scratch mark on a polished coated sample, treated with heating program $H-3$: a) 5000X image from the beginning of the scratch, b) 800X overview image of the scratch end, and c) 5000X image of the area inside the blue frame in figure b).

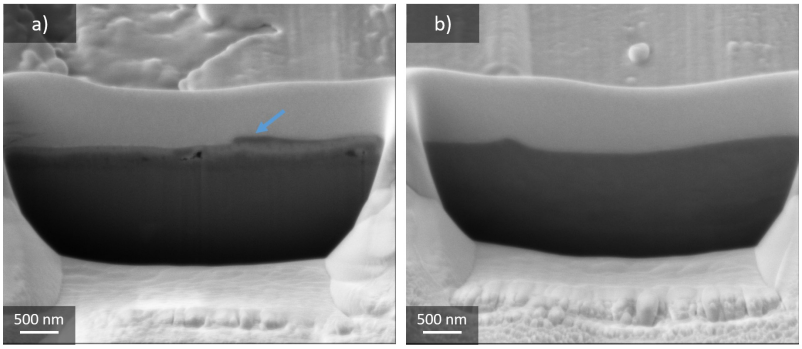

Figure 4.17: Interface images at 25000X at different positions of a scratch mark on a polished coated sample, treated with heating program $H-3$: a) at the beginning of the scratch, and b) at the end of the scratch. The blue arrow points at an impurity layer that has been deposited on top of the coating layer by the indenter.

Figures 4.18 and 4.19 show the surface- and interface regions of sample P_{H-4}. Once again, the surface images show the same trends as for sample P_{H-2}, with discoloration at the beginning of the scratch, a bare substrate at the end of the scratch, and little to no crack growth originating from the scratch itself, as seen in Figure 4.18a), b), and c), respectively. Figure 4.19a) reveals that the coating is present at the beginning of the scratch, while only the substrate can be identified in Figure 4.19b).

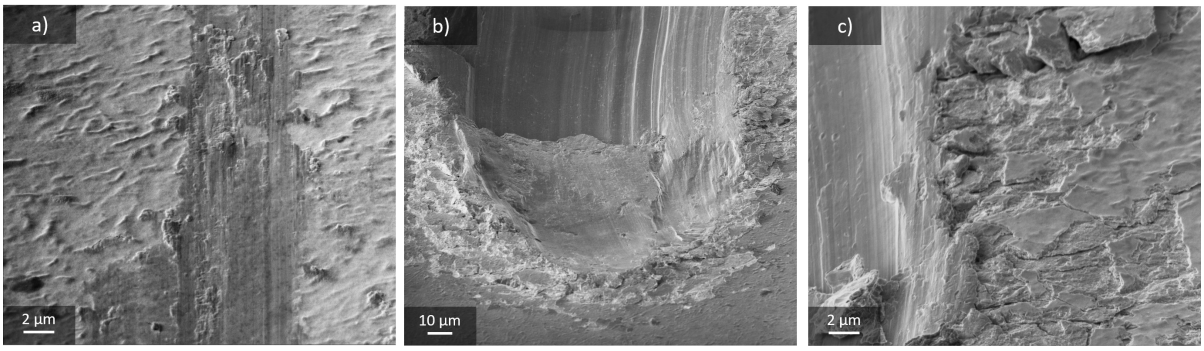

Figure 4.18: Surface images of different positions along a scratch mark on a polished coated sample, treated with heating program $H-4$: a) 5000X image from the beginning of the scratch, b) 800X overview image of the scratch end, and c) 5000X image of the edge at the scratch end. In this case, the area shown in c) is not visible in b).

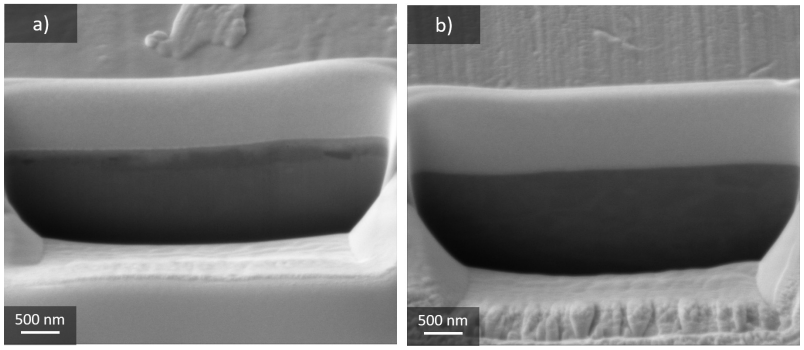

Figure 4.19: Interface images at 25000X at different positions of a scratch mark on a polished coated sample, treated with heating program $H-4$: a) at the beginning of the scratch, and b) at the end of the scratch.

4.2.4 Testing of dielectric properties

As the functionality of the finished samples lies in their piezoelectric properties, polarization curves were measured on each of the samples treated with the different temperature programs, as described in Section 3.2.3. The results, measured top-to-top between two gold electrodes deposited on top of the coating at 100 Hz and 1 V, are shown in Figure 4.20, and reveal large differences between the samples. Firstly, it can be seen that the samples treated with heating programs $H-1$ and $H-4$ display polarization curves that closely resemble those of a conductive material, while the samples treated with $H-2$ and $H-3$ display curves that are expected for dielectric materials. However, despite showing dielectric curves, the latter samples do not show the hysteresis loops that are characteristic for ferroelectric materials. Secondly, samples P_{H-1} and P_{H-4} display significantly higher maximum polarization values than the remaining two samples, which relates well to their apparent differences in conductivity.

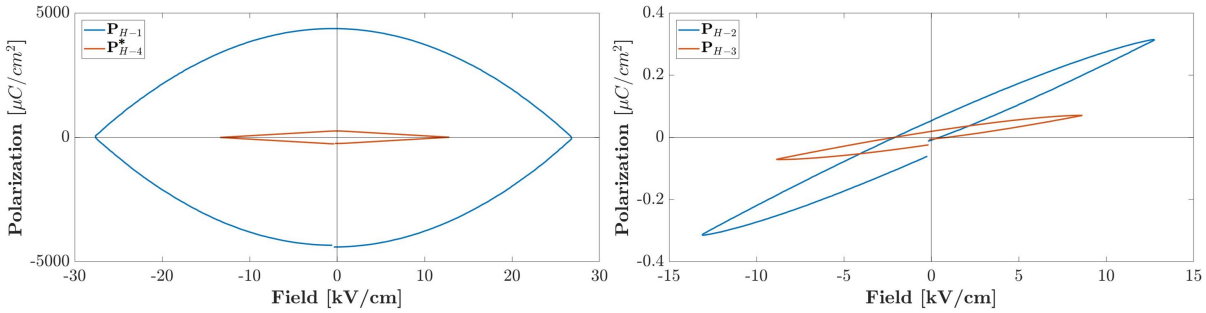

Figure 4.20: Polarization curves for polished samples treated with the different temperature programs, measured top-to-top at 1 V and 100 Hz. Note that the measurement for P^*_{H-4} resulted in the error message "Overflow", despite utilizing the highest current range.

During piezoelectric testing of sample P_{H-3}, approximately one month after the sample was produced, an interesting observation was made: As soon as the gold electrode was touched with one of the probe tips of the aixACT instrument, a dark brown/black spot appeared at the point of contact, even before any measurements had been made. This occurred when touching several electrodes, and the spots started out small, but kept growing in size until they covered most of the electrode. On some of the other electrodes, however, no such spots were observed. Towards the end of the testing session, the size of the spots seemed to have stabilized, but the following day the spots had disappeared completely, indicating that some kind of reversible process had occurred. To investigate this more closely, the sample was re-tested one and two weeks later, both times resulting in the generation of spots, but significantly smaller than the first time. This time, it could be seen that the spots disappeared during the testing session, strengthening the hypothesis of a reversible reaction occurring. After returning from CoViD-19 lock-down, six weeks later, the samples treated with the remaining temperature programs were sputtered and tested for dielectric properties. On these samples, no spots were observed, and it was therefore decided to re-test the sample P_{H-3}, which previously had shown spots. At this point, however, no spots could be observed on this sample either, despite running the exact same procedure as the preceding tests on this sample.

A first hypothesis was that the time spent between the coating procedure and the testing had an impact, as the spots on sample P_{H-3} were observed to be smaller for each time the sample was tested, before eventually not appearing at all after the lock-down period of six weeks. However, when coating and producing the textured samples (to be discussed later), the dielectric measurements were done only one week later, with no spots appearing. It should be noted that these samples were treated with heating program $H-2$, and not $H-3$, but this observation seems to weaken the time-related hypothesis significantly. A second hypothesis was related to the generation of oxygen vacancies during the calcination of the coating, as the samples were cooled from maximum temperature in N_2-gas. These oxygen vacancies, when exposed to an electric field, could migrate towards the electrodes, and generate the observed spots. As the samples were stored in air, it was believed that the ambient conditions contributed to the elimination of the oxygen vacancies over time. It was therefore decided to anneal the sample in question in N_2-gas at 400 °C for 4 h, to try to re-introduce the vacancies. However, upon re-testing of the dielectric properties, no spots were observed this time either. Also, no significant difference could be seen in the polarization curves before and after annealing, as shown in Figure 4.21. Therefore, the

oxygen vacancy migration hypothesis seems weakened, as well. Finally, to keep track of what was tested and observed when, Figure 4.22 shows a timeline for all of the dielectric testing.

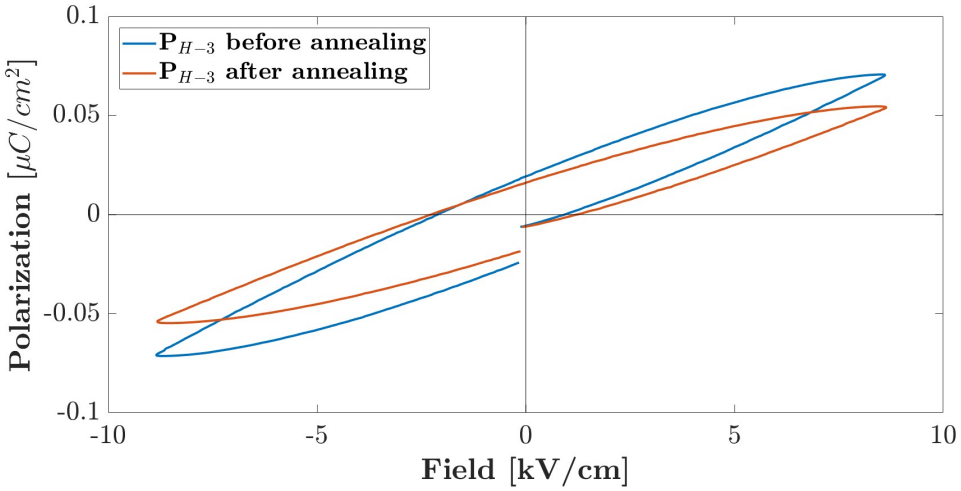

Figure 4.21: Polarization curved for polished sample treated with heating program $H-3$ before and after annealing in N_2-gas at 400 °C for 4 h, measured top-to-top at 1 V and 100 Hz.

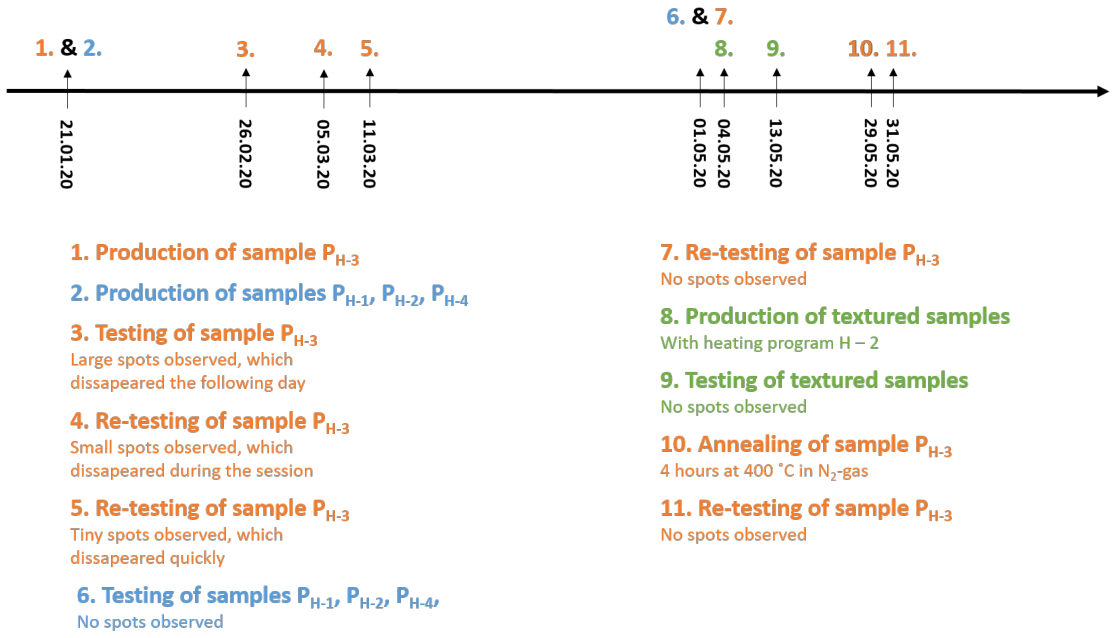

Figure 4.22: Timeline showing important dates and observations related to the dielectric testing of the samples. The tests are color coded according to the sample they are related to, with orange representing sample P_{H-3}, blue representing the remaining samples P_{H-X}, and green representing the textured samples.

4.2.5 Selection of best heating program

In order to finally decide on the heating program that resulted in the best properties, each program was ranked in terms of degree of oxidation, phase purity and crystallinity, adhesion, and polarization curves. The rankings are based on discussions in Section 5.2, and are shown in Table 4.1, where 1. is the best score, 4. is the worst score, and "-" indicates an invalid result.

Table 4.1: Ranking of the different heating programs in the categories used for the evaluation process, where 1. is the best score, 4. is the worst score, and "-" indicates an invalid result.

Category	*H–1*	*H–2*	*H–3*	*H–4*
Degree of oxidation	1.	2.	4.	2.
Phase purity and BT crystallinity	4.	1.	1.	3.
Adhesion	4.	1.	2.	3.
Polarization curves	-	1.	2.	-
Overall	4.	1.	2.	3.

Based on this table, and independent of the outcome of the two invalid polarization measurements, it is clear that heating program $H-2$ results in the overall best properties. Thus, this heating program was used in the later stages of the experimental work, where laser-textured substrates were spin-coated.

4.3 Textured samples

After completing the first sub-goal of determining that heating program $H-2$ was the best candidate for the coating calcination process, the focus was turned to the main objective of this thesis, namely the spin-coating of substrates with a surface texture. This was done according to the procedure described in Section 3.2.2, and post-production characterization steps included new measurements of surface roughness and phase purity, as well as imaging of the coating-substrate interface, and finally measurements of dielectric properties. In the following, the results regarding these properties, all of which are important for the final application of the coating on bone replacement implants, will be the presented.

4.3.1 Surface roughness

One of the main reasons for investigating spin-coating of textured substrates is the knowledge of how surface texture and roughness improves properties such as bone growth and -attachment. It is thus important that not only the substrates themselves are rough, but that this roughness is retained after the spin-coating procedure. Therefore, an important characterization step after the spin-coating was area surface roughness measurements, carried out as described in Section 3.2.3, which reveal whether or not the applied coating concealed or retained the texture of the substrates. The results, shown in Figure 4.23 reveal a decrease in roughness for all of the samples, except for the sample group with the LIPSS texture (L), which experienced a slight increase in roughness. It should be noted that the roughness of the samples changed only slightly, indicating that little planarization of the texture has occurred. Further confirmation of the retaining of surface texture after coating

can also be seen in Figure 4.24, which shows the topography height profiles of the coated samples. As before the coating, it is still possible to see some polishing stripes on the R-sample, while these are now covered on the G-sample. The grid-pattern on samples G and LG is also still clearly visible, while the surface structure of the L-sample no longer has its periodic pattern of diagonal bright and dark lines.

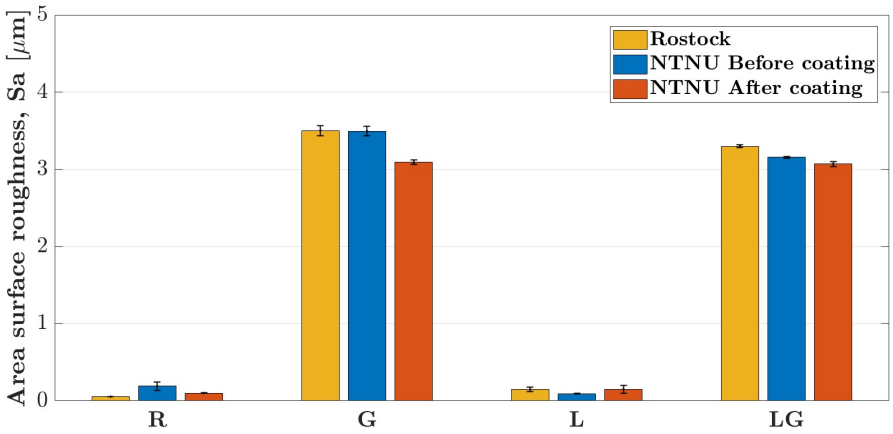

Figure 4.23: Comparison of area surface roughness values of uncoated samples, measured in Rostock (yellow) and at NTNU (blue), with coated samples measured at NTNU (orange).

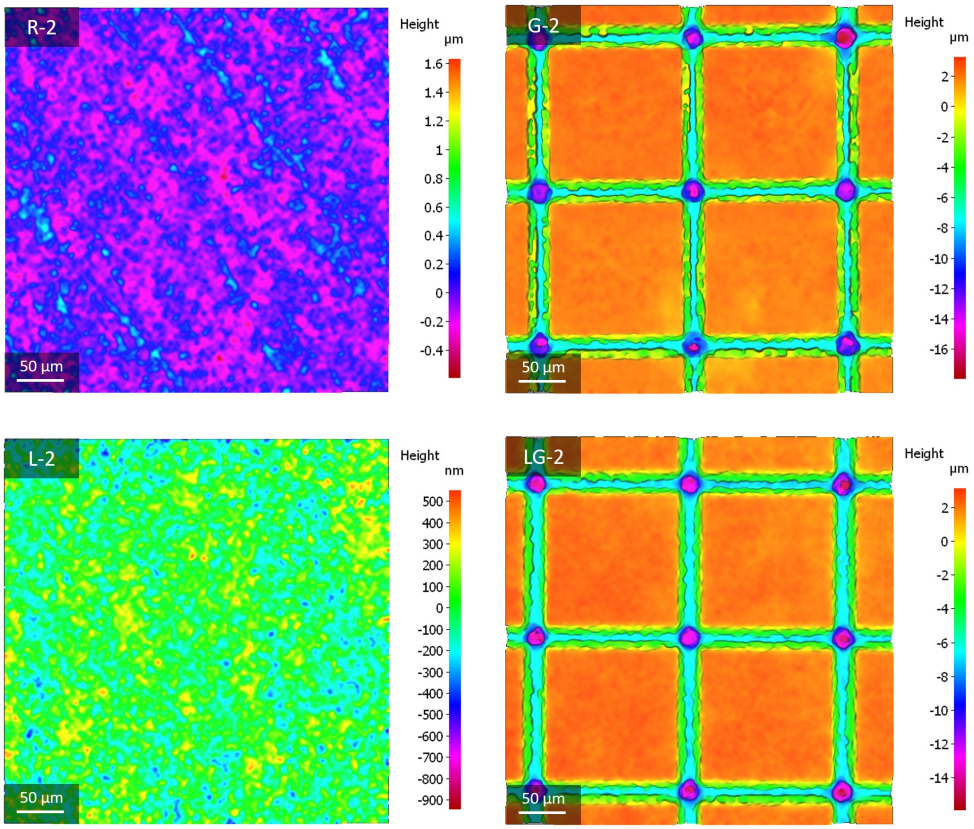

Figure 4.24: Topography height profiles of a selection of coated substrates.

4.3.2 Phase purity

Another important step was to determine whether or not the different substrate textures facilitated the formation of different types of reaction products, thus ultimately affecting the phase purity of the coating. This was done by carrying out GI-XRD on all of the coated substrates and using the PDF-database to match the obtained diffraction peaks with plausible chemical compounds, as described in Section 3.2.3. All of the measured diffractograms on samples with the same texture contained the same diffraction peaks, and one representative diffractogram from each texture group was therefore selected to represent the remaining samples. For ease of comparison, the measured diffractograms are shown together in Figure 4.25. From this figure, several interesting differences and similarities between the textures are revealed. Firstly, by the presence of its main peak at approximately 2θ = 31.5°, it can be seen that BT was formed on all of the substrates. However, this peak is significantly higher and sharper for the reference sample compared to the samples with the remaining three textures, indicating that the formation of BT occurred more easily on the reference sample. This is further confirmed by looking at the remaining BT peaks, which are clearly visible for the reference sample, but barely visible for the remaining samples. Furthermore, the presence of rutile phases in all of the diffractograms indicates that oxidation has occurred for all samples. In this case, the intensity and sharpness of the rutile peaks is similar for all of the textures, perhaps being slightly more severe for samples R-1 and G-1. In these two samples, small traces of the anatase phase can also be seen, which are not as visible for samples L-1 and LG-1. Finally, the diffractogram of sample G-1 reveals a small peak at approximately 2θ = 28°, which is not present in any of the other textured samples. By its match from the PDF-database, this peak is suggested to represent a barium aluminium titanium oxide.

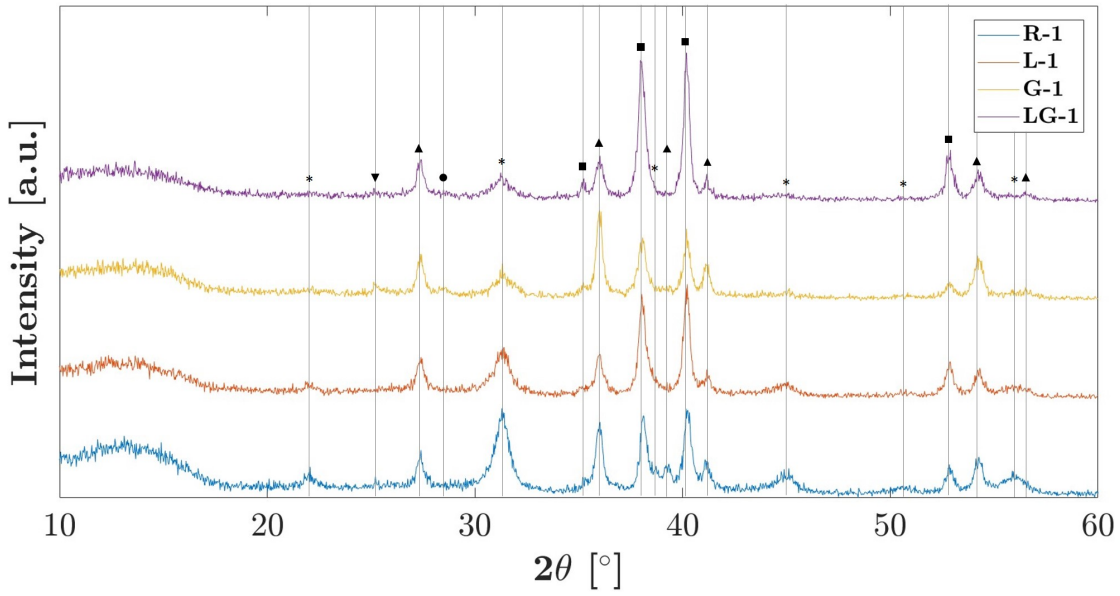

Figure 4.25: Measured GI-XRD diffractograms for coated, textured samples treated with heating program $H-2$. The peak are marked with: (*) for $BaTiO_3$ (PDF 04-012-8127), (■) for TiAl10V4 (PDF 04-002-8708, best replacement for Ti6Al4V), (▲) for the rutile polymorph of TiO_2 (PDF 04-003-0648), (▼) for the anatase polymorph of TiO_2 (PDF 00-021-1272), and (•) for Barium aluminium titanium oxide ($Ba_{1.181}Al_{1.903}Ti_{6.087}O_{16}$, PDF 01-076-2767).

A note of caution when it comes to the diffraction patterns is that GI-XRD is intended to be carried out on planar samples, which is not the case for the textured samples investigated in this thesis. As the incident angle of the X-rays is low, any irregularities on the sample surface might result in major deflections in the signal to be detected, thus resulting in incorrect results. This is especially important for samples G and LG, where the presence of grid-lines might interfere significantly with the incident beam. Also the randomly nanotextured surface on samples L and LG might interfere with the incident beam, and give observed results that do not represent the actual composition of the samples. Therefore, some caution should be taken when comparing GI-XRD diffractograms of samples that differ in terms of surface geometry and texture.

4.3.3 Coating microstructure and substrate-coating interface

To achieve a better impression of how the spin-coating procedure affected the surface topography, the coated samples were imaged by secondary electron imaging in a FIB-instrument, as described in Section 3.2.3. The resulting images, shown in Figure 4.26, confirm the findings in Section 4.3.1: The coating has not been able to fill the grid-lines on samples G-3 and LG-3, neither has it filled the polishing lines on sample R-3. However, the polishing lines on the flat surfaces of sample G-3 are no longer visible, despite that the flat surfaces of samples G are untreated, and should in principle be equal to sample R. Additionally, it seems that some kind of periodic structure of alternating bright and dark lines have appeared on sample L-3, especially visible in the bottom right part of the image.

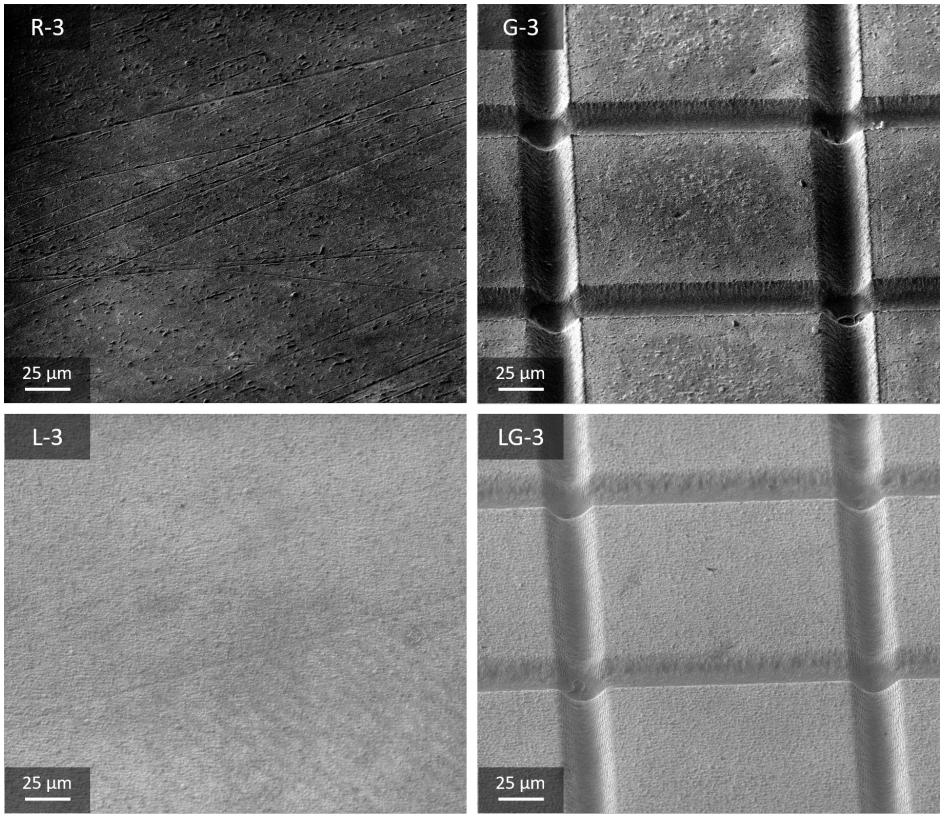

Figure 4.26: Overview images at 500X of the surfaces of the coated, textured samples.

Texture group R

High-magnification images of the surface of sample R-3 were taken at 5000X and 15000X magnification to achieve a more detailed overview of the coating microstructure, and are shown in Figure 4.27a) and b) respectively. The former of these shows a mostly smooth surface, with some hills and ridges, while the latter reveals that the smooth areas of the coating are highly porous, with pore sizes below 100 nm. Additionally, some growth of small, spherical grains with a size of approximately 100 nm can be observed, especially present on the hills and ridges on the surface. Cross-section images of two different reference samples, R-1 and R-3, show some variance in the appearance of the coating-substrate interface, where the coating layer in Figure 4.28a) lies nicely on top of a smooth oxide layer, while the coating layer in Figure 4.28b) appears to be more mixed into the oxide layer. In both cases, a trail of pores running along the oxide-substrate interface can be observed, while some porosity is also found further towards the top of the oxide layer. The coating layer itself appears dense in both cases, with no cracks running along the coating-oxide interface, thus indicating good adhesion. Note that examples of both of these types of interfaces were found in both samples, and these two interfaces do therefore act as representative images for the entire texture group.

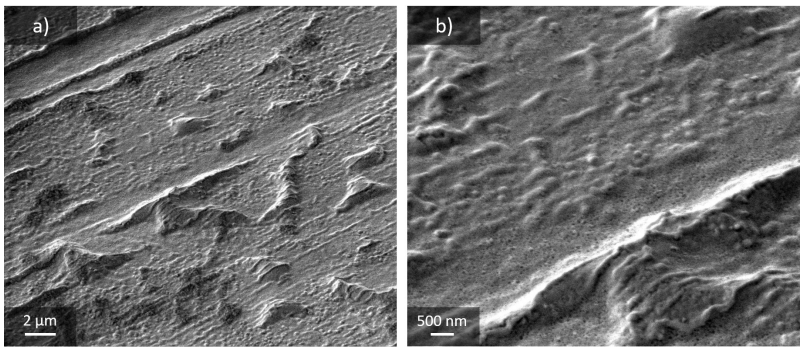

Figure 4.27: Surface image of sample R-3 at a) 5000X, and b) 15000X.

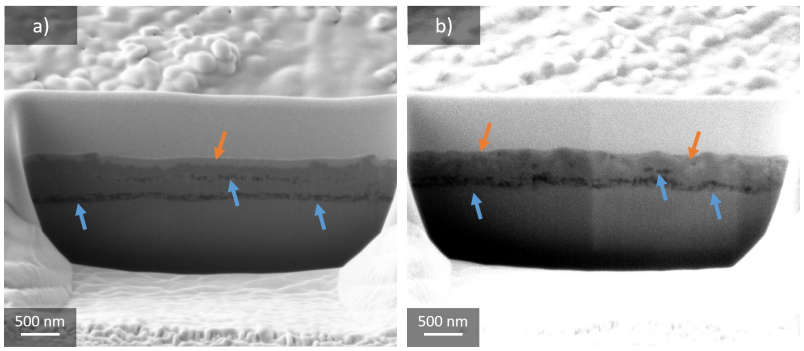

Figure 4.28: Interface images at 25000X of samples a) R-1 and b) R-3, where the blue arrows point out porous features of the layers, while the orange arrows point indicate the inhomogeneities of the coating layer.

Texture group L

Figure 4.29 shows high-magnification surface images captured from the inside and the outside of the LIPSS-textured area on sample L-3. As expected, it can be seen that the coating on the non-textured area, shown in Figure 4.29a), looks similar to that of sample R-3, being smooth with some hills and ridges. However, the surface topography of the coating inside the textured area, displayed in Figure 4.29b), is vastly different, showing a wavy pattern of periodic ridges with smooth areas between the ridges. On the ridges, growth of spherical grains with a diameter of approximately 100 nm can be observed. This grain growth is not present in the areas between the ridges, which upon further magnification, shown in Figure 4.29c), reveal the presence of a porous coating, once again with pore sizes below 100 nm. The ridges and valleys of this sample can clearly be seen in Figure 4.30, which shows the coating-substrate interface region of two different cross-sections made on sample L-1. In this case, instead of forming a smooth coating layer as for the R-textured samples, the coating partially fills the gap between the ridges on the nanotextured substrate, dampening some of the texturing effect. However, as is clear from both Figures 4.29b) and 4.30, the upper-most parts of the sample are not completely planar, and some texture has been retained. Also here, the trail of pores running along the oxide-substrate interface is observed, as well as some porosity in the higher layers of the oxide layer. The coating layer, however, appears mostly dense, and the good filling between the ridges of the substrate, with no sign of cracking along the coating-oxide interface, implies good coating adhesion.

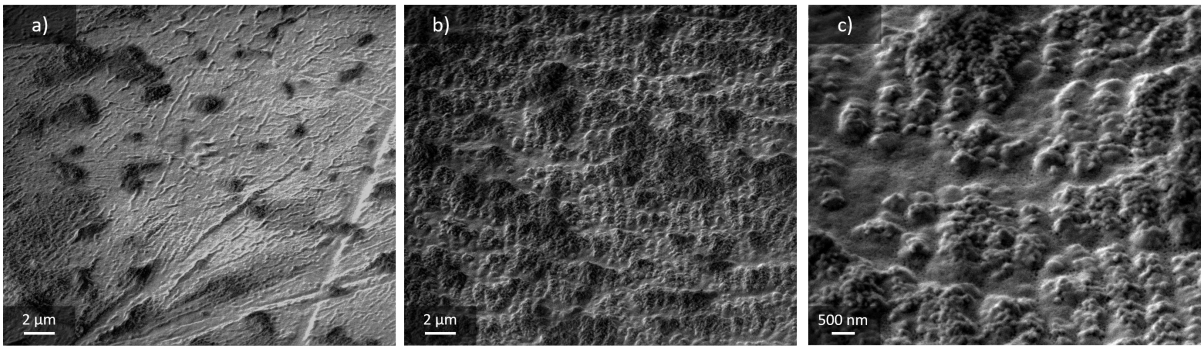

Figure 4.29: Surface image of sample L-3 at a) 5000X outside of the textured area, b) 5000X inside of the textured area and b) 15000X inside of the textured area.

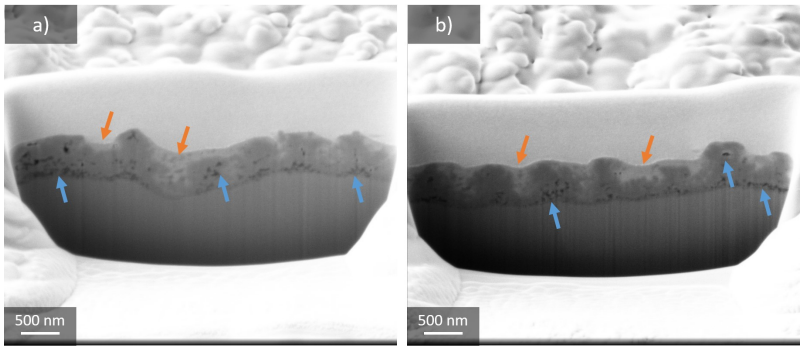

Figure 4.30: Interface images at 25000X of two different regions of sample L-1, where the blue arrows point out porous features of the layers, while the orange arrows indicate that the coating has partially filled the area between the ridges.

Texture group G

Surface images were also captured of sample G-3, and Figure 4.31 displays the images from some of the flat areas of this sample. As in the case of sample L-3, the image in Figure 4.31a) was taken from outside of the textured area, and closely resembles the more or less smooth appearance of sample R-3. However, when investigating the flat surfaces inside of the textured area, shown in Figure 4.31b), a large degree of crystal growth could be observed. Upon further magnification (Figure 4.31c)), the crystals appear to have a tetragonal shape, where the largest have a length of 500-600 nm. Additionally, no pores can be observed on the coating surface, neither inside nor outside of the textured area. Also on this sample, a cross-section was made to reveal the coating-substrate interface, and an overview image of this cross-section is shown in Figure 4.32. By looking more closely into the positions of the interface indicated by the colored frames in Figure 4.32, it becomes clear that the interface region is not completely homogeneous, where only small parts of the oxide layer appears to have been covered with the bright coating layer. Additionally, darker areas can be observed towards the top of the oxide layer, indicating the formation of some secondary phase. Furthermore, the thickness of the oxide layer varies significantly, still with a trail of pores running along the oxide-substrate interface.

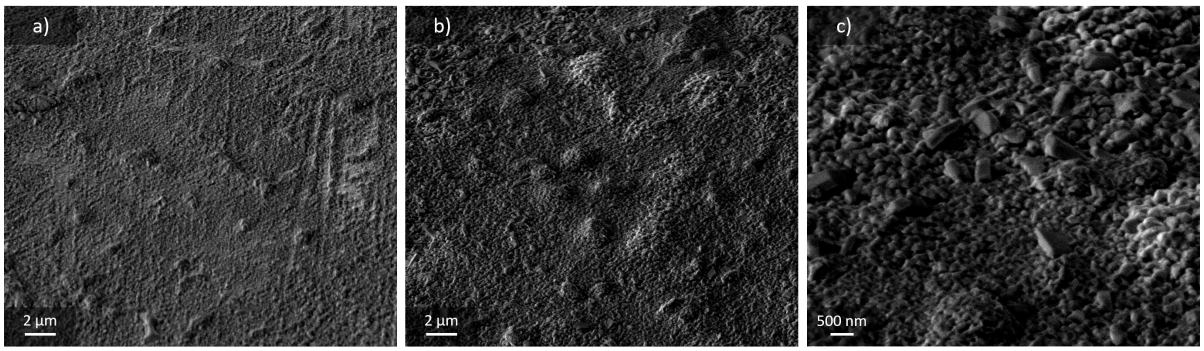

Figure 4.31: Surface image of a flat surface of sample G-3 at a) 5000X outside of the textured area, b) 5000X inside of the textured area and c) 15000X inside of the textured area.

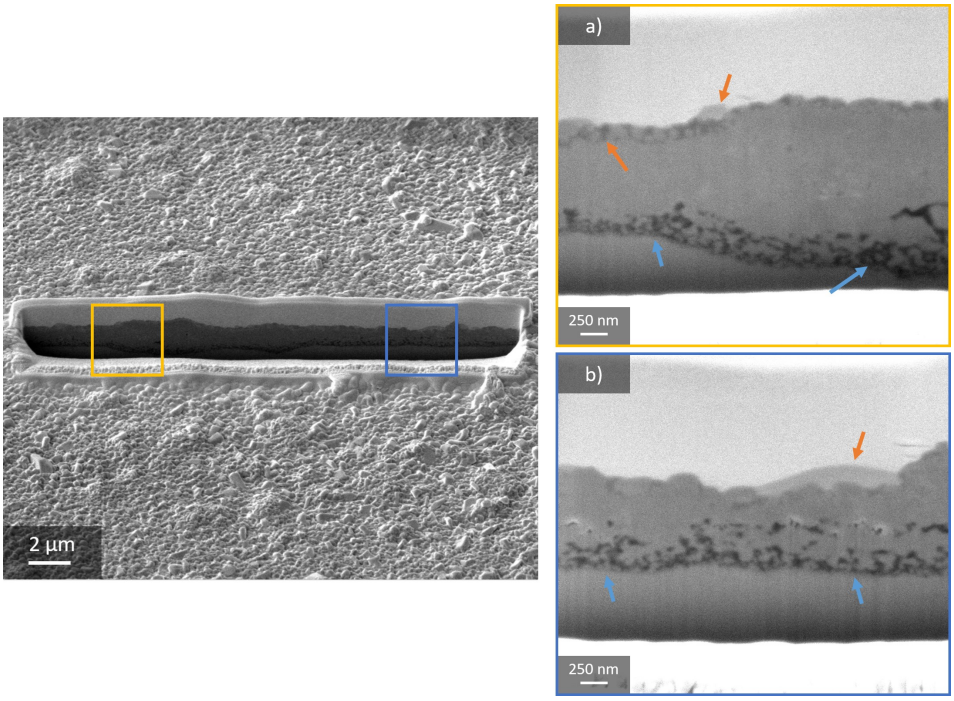

Figure 4.32: 5000X overview interface images of a flat surface on sample G-3, along with images at 35000X of the areas indicated by the colored frames. The blue arrows point out porous features of the layers, while the orange arrows point at the dark secondary phase, as well as the poor coating coverage.

Also the valleys created by the grid pattern on sample G were imaged, and the resulting images are shown in Figure 4.33. Here, it can be seen that the crystals described previously on the flat surfaces, also are present towards the top of the valley (Figures 4.33a) and c)), while no crystals can be observed in the bottom of the valley (Figure 4.33b)). Instead, the bottom region is highly porous, with some pores as large as 200 nm in diameter. Large differences going from the bottom towards the top of the valley can also be seen in the cross-section images of the valley, shown in Figure 4.34. At the bottom of the valley (Figure 4.34a)), the coating layer is thick and porous, while it becomes thinner and less porous towards the top of the valley (Figure 4.34b)), and finally more or less disappears when the top of the valley has been reached (Figure 4.34c)). The thickness of the oxide layer appears to remain quite constant, once again with pores running along the oxide-substrate interface.

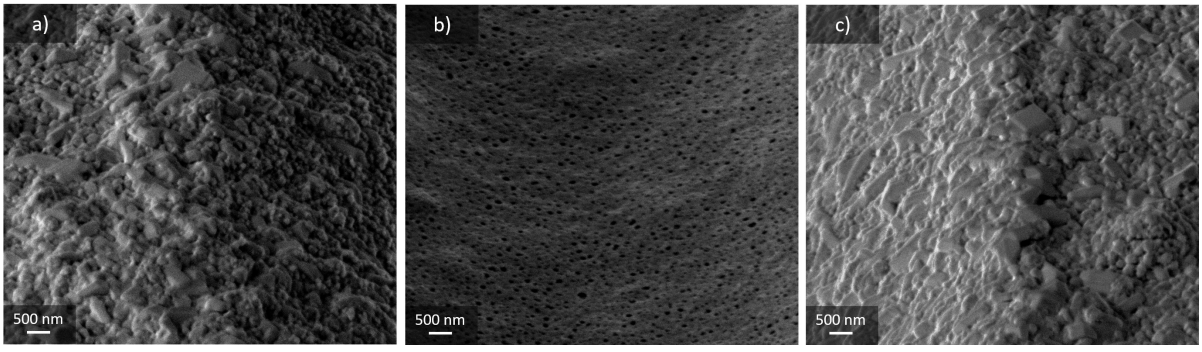

Figure 4.33: 15000X image of a grid-valley of sample G-3: a) upper left edge of valley, b) bottom of valley, and c) upper right edge of valley.

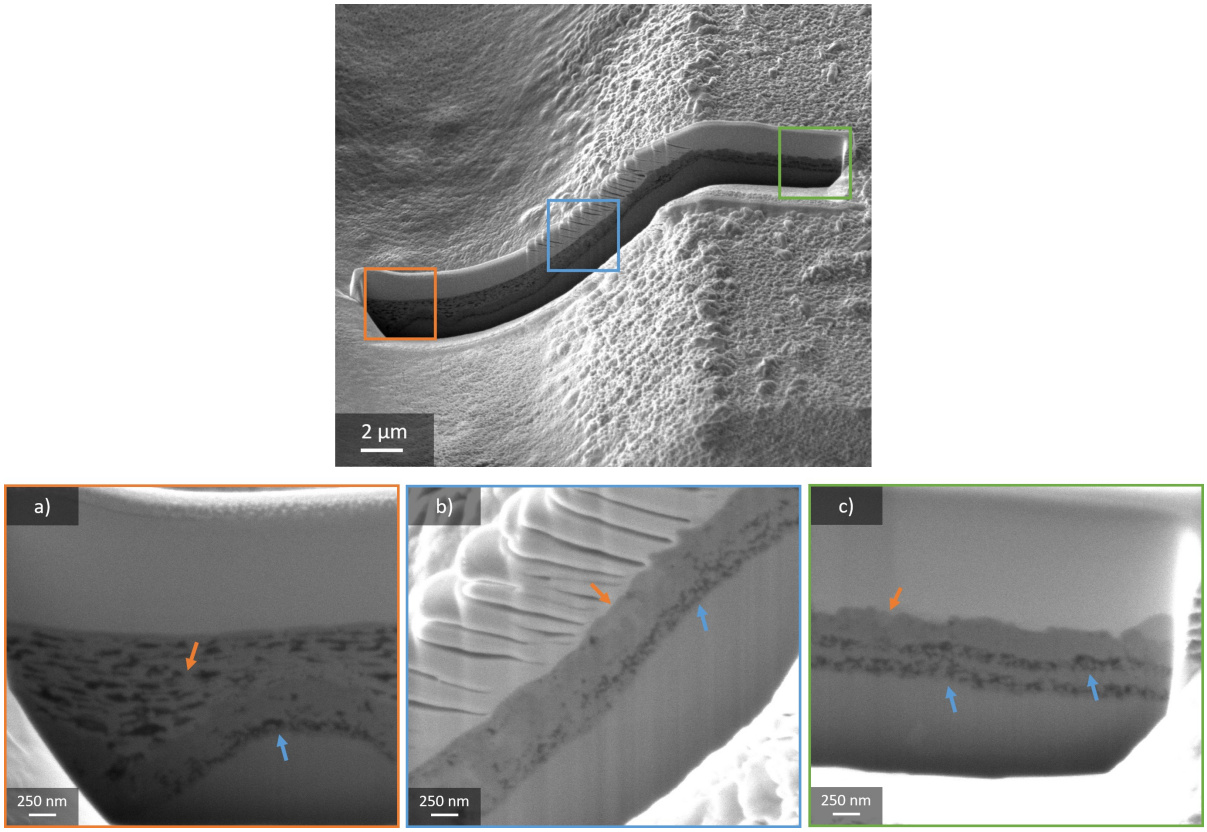

Figure 4.34: 5000X overview interface images of a grid-valley on sample G-3, along with images at 35000X of the areas indicated by the colored frames. The blue arrows point out porous features of the layers, while the orange arrows point at important features of the coating layer.

Texture group LG

Figure 4.35 shows surface images captured of flat areas on sample LG-3, outside (Figure 4.35a)) and inside (Figures 4.35b) and c)) of the textured area. As for all of the previous textures, the microstructure of the coating outside of the textured area resembles the microstructure of the coated R-3 sample, being mostly smooth, with some hills and ridges. Inside the coating area of sample LG-3, a periodic wavy pattern of ridges can be observed (Figure 4.35b)), and no clearly smooth areas can be observed between the ridges. Instead, both the ridges themselves, and the valleys between them, are subject to significant grain growth (Figure 4.35c)), with grains being spherical with a size of approximately 100 nm. For the flat surfaces on this sample, no pores can be observed, implying that the density of the coating is good. This is confirmed by looking into the cross-section images in Figure 4.36, which reveal that a dense coating is formed in the areas between the ridges on the nanotextured substrate. The appearance of the oxide layer varies significantly within the same cross-section, showing a periodic wavy pattern in Figure 4.36a), and a more even structure in Figure 4.36b). However, in both cases, a trail of pores is found along the oxide-substrate interface, as well some pores towards the higher parts of the oxide layer.

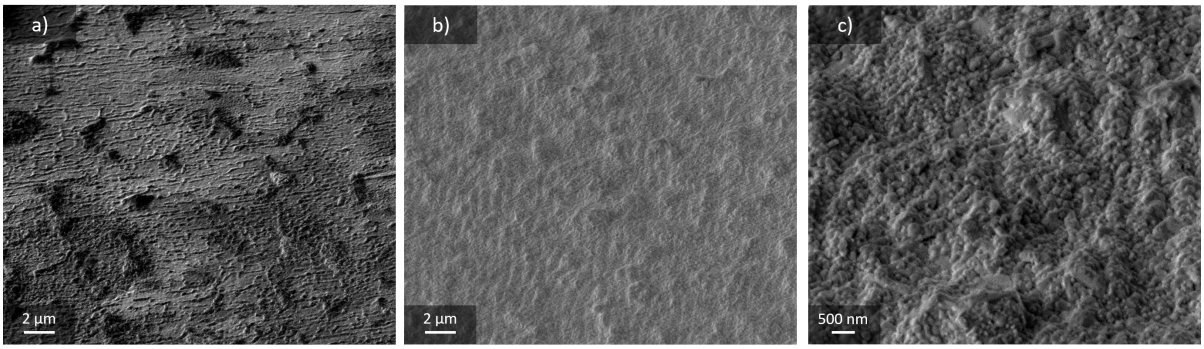

Figure 4.35: Surface image of a flat surface of sample LG-3 at a) 5000X outside of the textured area, b) 5000X inside of the textured area and b) 15000X inside of the textured area.

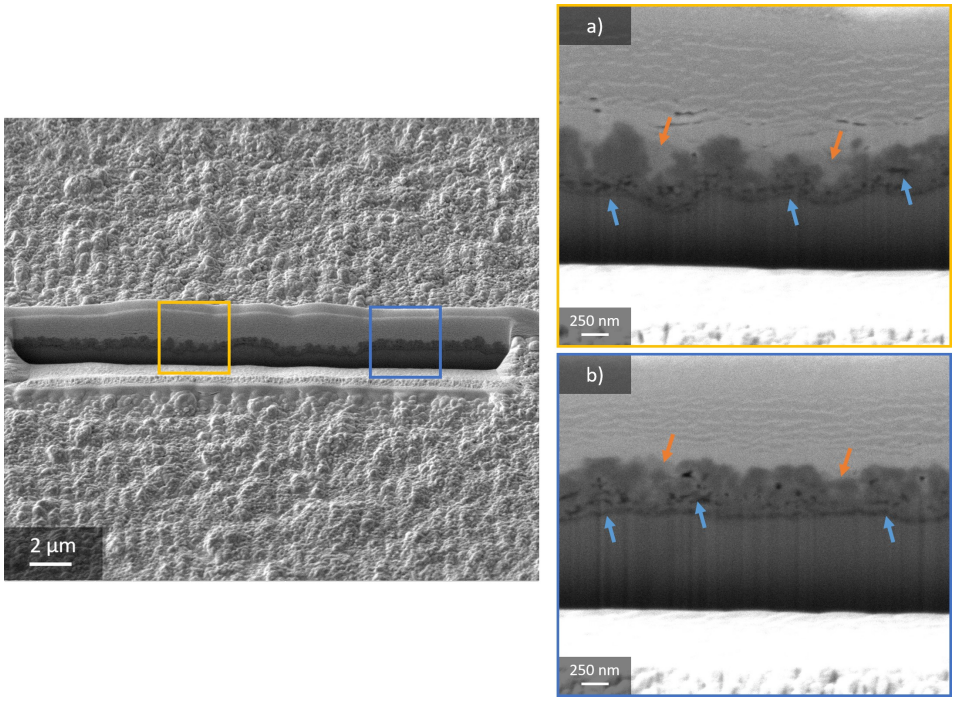

Figure 4.36: 5000X overview interface images of a flat surface on sample LG-3, along with images at 35000X of the areas indicated by the colored frames. The blue arrows point out porous features of the layers, while the orange arrows indicate that the coating has partially filled the area between the ridges.

The surface images of a grid-valley of sample LG-3 are shown in Figure 4.37, and mimic the trends of sample G-3: Towards the top of the valley (Figures 4.37a) and c)), the microstructure is similar to that of the flat surface, while the bottom of the valley (Figure 4.37b)) is highly porous. The differences in the coating layer between the bottom and the top of the valley are also obvious in Figure 4.38, where the coating is thick and porous at the bottom of the valley (Figure 4.38a)), thinner and denser half-way up the valley (Figure 4.38b)), and absent at the top of the valley (Figure 4.38c)). Note that also the valley of sample LG-3 has a wavy substrate surface, and that large pores in the coating layer appear to form at the dips in this wave-pattern. As for the other cases, the oxide layer is characterized by a trail of pores running along the oxide-substrate interface, and with some occasional pores towards the higher parts of the layer.

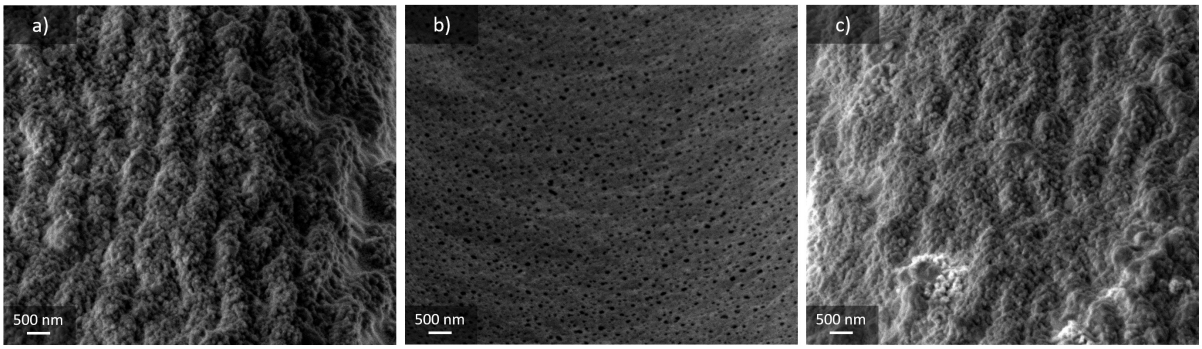

Figure 4.37: 15000X image of a grid-valley of sample LG-3: a) upper left edge of valley, b) bottom of valley, and c) upper right edge of valley.

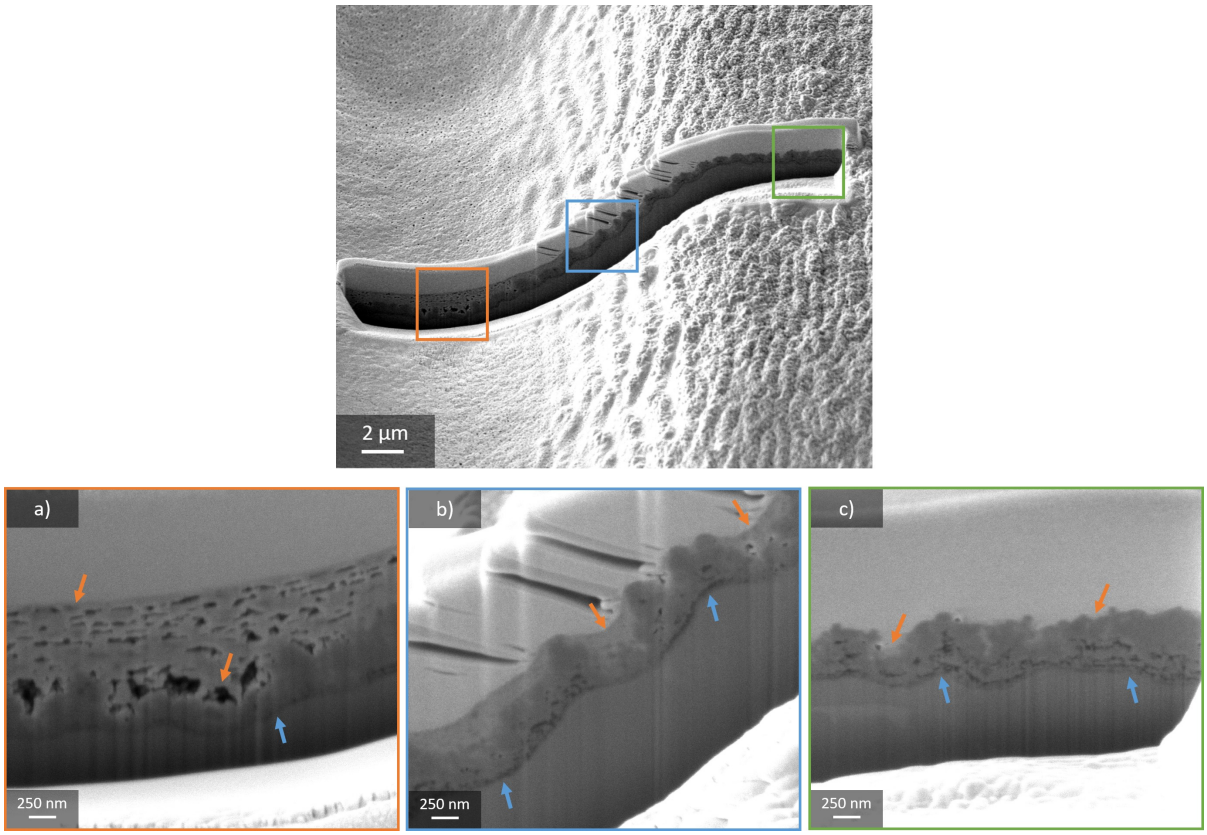

Figure 4.38: 5000X overview interface images of a grid-valley on sample LG-3, along with images at 35000X of the areas indicated by the colored frames. The blue arrows point out porous features of the layers, while the orange arrows point at important features of the coating layer.

4.3.4 Composition of coating-substrate interface

To supplement the information regarding phase purity of the coating, in addition to obtaining a better understanding of the chemical processes occurring at the coating-substrate interface, EDS was carried out on the coated, textured samples. Several samples were tested according to the procedure described in Section 3.2.3, but only a representative selection will be shown in the following. Figure 4.39 shows a grid-valley of sample LG-3, where the selected EDS line scan was performed in the area within the colored box.

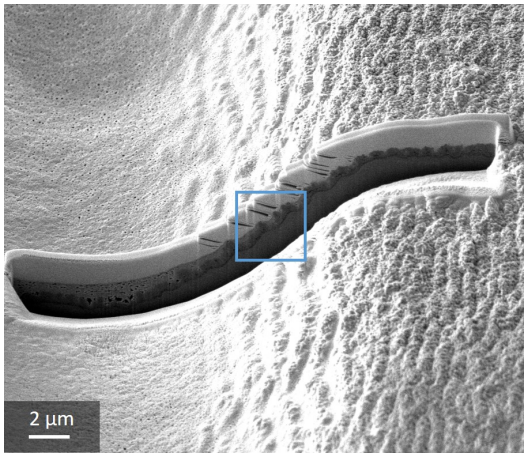

Figure 4.39: Overview of a grid-valley of sample LG-3, where the colored box indicates the position where the EDS line scan was performed.

Figure 4.40 displays the position of the line scan, indicated with the red line, as well as the results obtained from scanning along this line. As explained in Section 3.2.3, several elements were detected, but only the intensities of the relevant elements are plotted. Furthermore, the elemental intensity results are divided into two plots, as Ba and Ti have intensities so high that it would be difficult to obtain any detail in the lines of O, Al and V. From this figure, which also mimics the trends for the EDS line-scans shown in Appendix C, the intensity of Ba, Ti and V is seen to be increasing towards the substrate side of the interface, while that of O and Al is decreasing in the same direction.

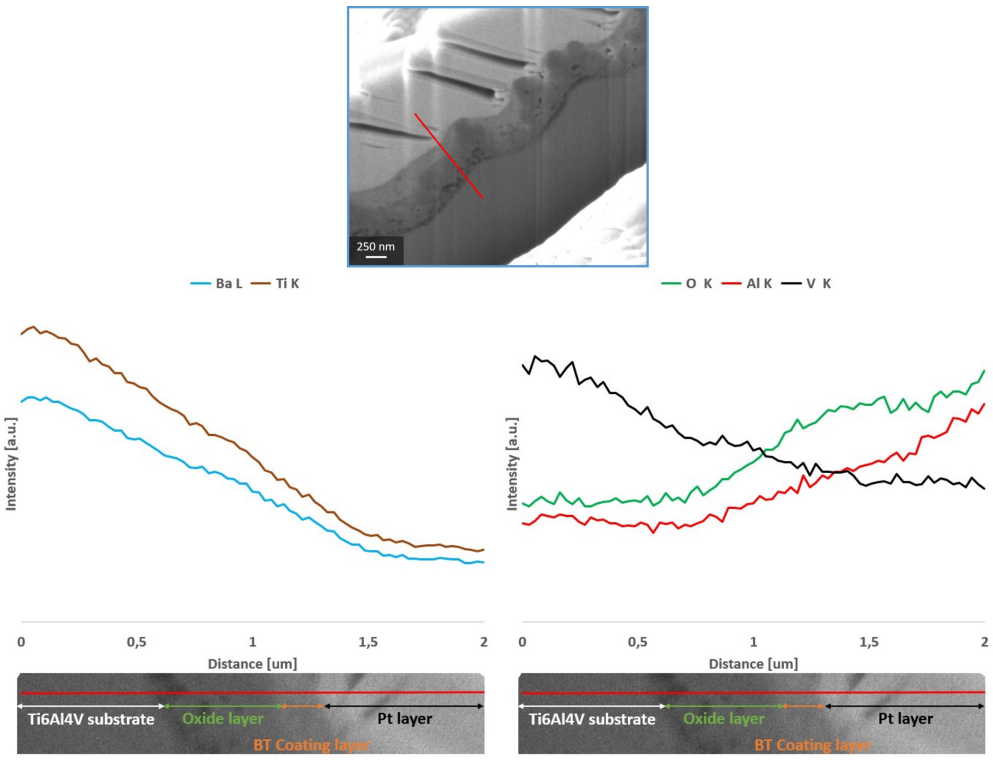

Figure 4.40: Results of EDS line scan half-way up a grid-valley on sample LG-3, along the indicated red line inside the colored frame. Note that scales of the y-axes on the plots are different, with the intensities of Ba and Ti far greater than those of O, Al, and V.

In general, it is difficult to distinguish Ba and Ti by EDS-analysis, due to the overlapping of the Ba L energy with the energy of Ti K, as shown in Table 3.10. This is also evident from the figure above, where the Ba and Ti lines follow the exact same trends, down to the smallest dips and bumps. Despite this, the variations in the layers should still in principle be judgeable by examining the behaviour the Al, V and O lines. However, during the line scanning, drifting of the images perpendicular to the cross-section region was observed, independently of how the samples were oriented. This causes large uncertainties in the measurements, and rules out further implementation of these results. Thus, the EDS results were not included in the final evaluation of the coated samples, and will not be discussed any further.

4.3.5 Testing of dielectric properties

As mentioned previously, it is the piezoelectric properties of the final bone replacement products that ultimately are believed to improve their bioactivity. Therefore, in order to assess which textures promoted the best properties, polarization curves were measured on the textured samples. These measurements were carried out top-to-top between two gold electrodes deposited on the coating surface as described in Section 3.2.3, with the film thickness assumed to be two times the total oxide and coating layer thickness obtained for heating program $H-2$ in 4.10. Figure 4.41 shows the results from the polarization measurements. The loops for samples R-2 and G-2 are quite narrow, indicating little leakage, while samples L-2 and especially LG-2 appear to be more leaky. Furthermore, the maximum polarization value for sample LG-2 is more than twice as high as for R-2 and G-2, with sample L-2 showing a value in-between these. However, all of the maximum values are less than $0.2\,\mu C\,cm^{-2}$, and none of them show the typical hysteresis loops expected for ferroelectric samples. It is also worth noticing that the curves are more or less symmetric, for all of the textures, indicating that the samples react identically to positively and negatively applied voltages.

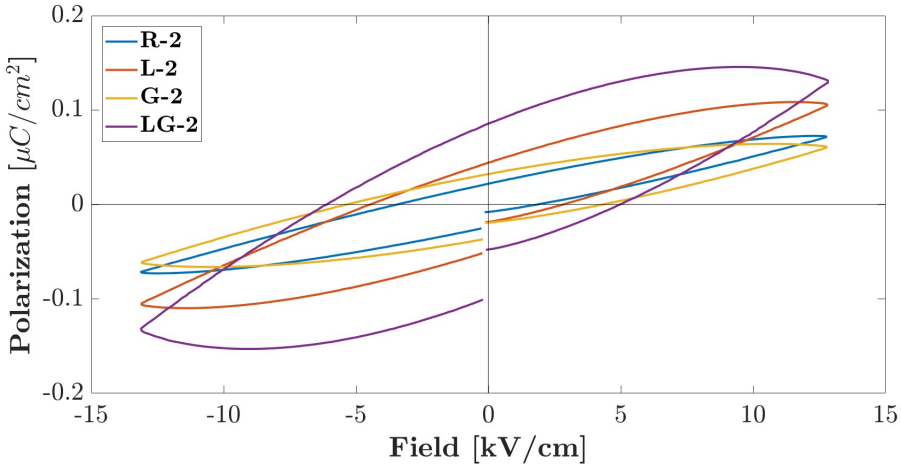

Figure 4.41: Polarization curves for coated, textured samples, measured top-to-top at 1 V and 100 Hz.

The polarization curves for the textured substrates were also measured top-to-bottom, between a gold electrode deposited on top of the coating and an exposed corner of the substrate, in order to examine whether or not charge injection might be a problem during

the dielectric testing of the samples. The results, displayed in Figure 4.42, resemble those of the top-to-top measurements in Figure 4.41 closely, once again with symmetric, but not ferroelectric curves. Samples G-2 and R-2 are most narrow with the lowest maximum polarization values, while samples L-2 and LG-2 are more leaky, with higher values for maximum polarization.

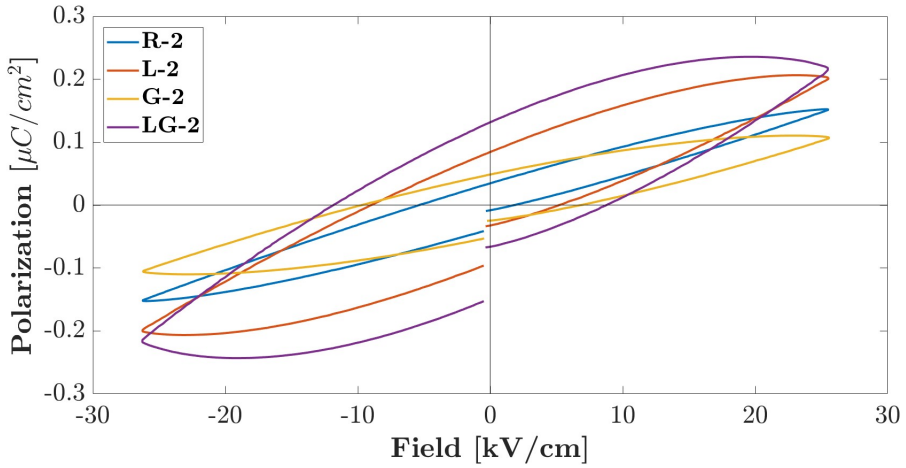

Figure 4.42: Polarization curves for coated, textured samples, measured top-to-bottom at 1 V and 100 Hz.

When calculating the electrical field for the polarization measurements in Figures 4.41 and 4.42, it was assumed that the total coating and oxide layer thickness was identical for each of the textured sample, with a value corresponding to that found for the oxide layer on sample P_{H-2}, shown in Figure 4.10. Based on the total thicknesses observed in the interface images of the textured samples in Section 4.3.3, this seems to be a reasonable assumption, and it is thus expected that the calculated developed electrical fields are more or less correct.

5 Discussion

5.1 Properties of uncoated substrates

5.1.1 Surface roughness and wetting of textured substrates

When comparing the topography height profiles of the textured, uncoated substrates in Figure 4.1 with the optical images of the same substrates in Figure 3.1, a mostly good resemblance can be found. For the reference sample (R), the major polishing stripes are clearly visible in the height profile, while the nanostructure pattern on the LIPSS-textured sample (L) also can be seen quite clearly in both of the images. Furthermore, the grid-lines for the Grid-textured (G) and LIPSS & Grid-textured (LG) samples are clearly visible both in the optical images and in the topography height profile. However, as these grid-lines are very deep compared to the polishing lines and nanotexturing on the flat surfaces, the topology height profile is unable to resolve the finer details on the flat surfaces properly. Thus, it seems like the obtained topography height profiles are not the best tools for visualizing the exact surface texture and roughness of samples with large size-differences of the roughness features, but they might still be useful for providing an overview of the main topographical features. To improve the resolution, an option could have been to capture additional optical images of the flat areas between the grid-lines, without actually imaging the grid-lines themselves, or to use scanning probe microscopy to reveal the more local structures of the substrates.

The average area surface roughness (Sa) measurements, carried out by the author at NTNU, on the uncoated, textured substrates, shown in Figure 4.2, reveal an Sa-development of $Sa_L < Sa_R << Sa_{LG} < Sa_G$. This seems to be a reasonable result, where the uneven polishing grooves on samples R and G make them more rough than their LIPSS-textured counterparts, and where the grid-lines of samples G and LG make these samples considerably more rough than samples R and L. However, measurements carried out on the same substrates at the University of Rostock (UoR), Germany, show that $Sa_R < Sa_L$, with the other relationships being the same, thus revealing a discrepancy between the measurements. For many reasons, it is difficult to determine which set of measurements is the most precise. Firstly, a confocal laser scanning microscope was used for the measurements carried out at UoR, while a regular optical microscope was used for the NTNU-measurements. The former, being a more advanced measurement technique is expected to give more accurate results, initially indicating that the UoR-results are more accurate. Furthermore, the UoR-results for each texture group are averages of measurements on three samples, where three measurements were carried out on each sample, while the corresponding NTNU-results are averages of measurements on four samples, where only one measurement was carried out on each sample. Based on this, the UoR-results are built on a larger data set, with nine measurements on each texture group, compared to four at NTNU, once again implying that the results from UoR are more accurate. However, large variations in the measurements are expected based on the selected area to investigate. This is especially true for samples R and G, where the flat surfaces are polished, but not textured in any other way. The different amount of polishing stripes in the imaged areas will have a direct effect on the results, and it is therefore important that a representative area of proper size is selected. Also on this point, there is a difference between the measurements at NTNU and UoR, where the area measured at NTNU is larger (408x408 µm) than that of UoR (256x256 µm), implying that the results

obtained at NTNU might be the most representative. A final observation to strengthen the case of the NTNU-measurements is the relationship between samples R and L, and between G and LG. In principle, samples R and G are equal, apart from the grid-lines on sample G, and the same is true for samples L and LG. As the grid-pattern on samples G and LG is made in the same way with the same depth, the difference in roughness between these samples should correspond to the differences on the flat surfaces, being either polished or LIPSS-textured. It is therefore expected that the difference between samples G and LG corresponds to the difference between samples R and L, which is only true for the NTNU-measurements. For this reason, the results from the measurements carried out at NTNU will be used in the further discussions related to area surface roughness.

The contact angle measurements carried out at NTNU on the uncoated, textured substrates before and after plasma cleaning are shown in Figure 4.3. Together with Figure 4.4, this figure implies a wetting relationship of $\theta_R < \theta_L << \theta_{LG} < \theta_G$ before plasma cleaning. However, the standard deviations in the measurements are large, and it can only be concluded that the wetting properties of samples R and L are better than those of samples G and LG. When comparing the contact angle measurements at NTNU with those of UoR, the observed differences are within the margins of error for all samples, except for texture group R. Interestingly, this is the same as for the area surface roughness measurements, shown in Figure 4.2 and discussed previously, where a large discrepancy in the Sa-value of texture group R was observed. This might imply that some changes to the surface of the R-samples have occurred during storing and transportation from UoR to NTNU. Exactly what is not possible to say with absolute certainty, but accidental scratching of the surface, surface oxidation, and pick-up of dust and other impurities are all events that might have influenced the surface properties. However, there is no reason for why these events should have happened to only one texture group, and not the others. Thus, a second, and perhaps more probable, explanation could be that only one measurement set simply was not accurate enough, and more sets should therefore have been measured to improve the reproducibility of the results.

As the processing parameters for the patterning processes often differ, or are not given at all, it is not straightforward to compare the surface area roughness- and contact angle values obtained in this work with those found for similar structures in the literature. In addition to this, it seems to be no standard set of parameters or methods to measure contact angles and area surface roughnesses, further complicating the issue. However, some comparisons of the trends in wetting behavior will be made with the literature, and the reader is directed to the respective articles for more detailed information on the respective systems. Firstly Martinez-Calderon et al. studied the wetting behavior of stainless steel patterned with combinations of ordered grid patterns and LIPSS [137]. Without the grid pattern, a contact angle of 75 ± 2.5° was observed for the non-treated surface, while it increased to 120 ± 2.5° when the LIPSS texture was introduced. The corresponding values with the grid pattern were 144 ± 2.5°, without LIPSS, and 156 ± 2.5°, with LIPSS. As the material used in this study is different than that of this thesis work, a direct comparison between the obtained contact angles is not suitable. However, the trends of how the texture affects the measurements can be compared. In both sets of measurements, the introduction of LIPSS texture increased the contact angle compared to an untreated-sample, and the introduction of a grid pattern further increased the observed contact angles. Additionally, Yang et al. observed a similar significant increase in contact angle after the introduction of a grid pattern on titanium

substrates [138], while Wu et al. found that LIPSS-textured stainless steel substrates resulted in higher contact angles than flat substrates [139], once again echoing the trends of the current thesis work.

It can clearly be seen from Figures 4.3 and 4.4 that the plasma cleaning process significantly improved the wetting of the samples. This corresponds well with results observed by Strohmeier when investigating the effect of plasma cleaning on aluminum foil [89], which, as titanium, spontaneously develops a thin oxide layer when exposed to air. The enhanced wetting can be explained by the removal of organic species and impurities during the plasma cleaning process, which allows the deposited droplets to spread more freely. Despite having a positive effect on the wetting for all of the texture groups, it is evident that the plasma cleaning had the most significant impact on samples G and LG, reducing their contact angles with nearly 30°. This can be explained by visual observations during the contact angle measurements: Before plasma cleaning, the contact angles of the droplets deposited on samples G and LG were in the proximity of 100°, and stably non-wetting in the time between droplet deposition and contact angle registration. After plasma cleaning, the droplet initially behaved in the same non-wetting way, before it suddenly spread out, resulting in the significantly reduced contact angle. This sudden spread is believed to represent the transition from a Cassie-Baxter regime, where the droplet was not able to wet the grid-valleys of samples G and LG [87], to a Wenzel regime, where the droplet is able to wet said valleys [85], as illustrated in Figure 5.1. A similar transition was observed by Murakami et al., when conducting high-resolution optical investigations of the wetting behavior of a fluorinated cycloolefin polymer substrate [140]. The surface of this substrate was highly textured, and covered by pillared lattices on the nano- to microscale. Directly after deposition, the water droplets in this study showed Cassie-Baxter behavior, not penetrating into the gaps between the pillars. However, within the matters of milliseconds, the droplets starts to penetrate into the grooves between the pillars, and complete wetting in the Wenzel regime occurred in a matter of seconds after deposition. This behavior was explained by sagging, i.e. downwards curving, of the base of the droplet when water started to evaporate, as explained by Papadopoulos et al. [141]. When this sagging reached a threshold value, the pressure created by the now curved water surface overcame the energy barrier for the transition from the metastable Cassie-Baxter state to the stable Wenzel state, resulting in complete wetting [140].

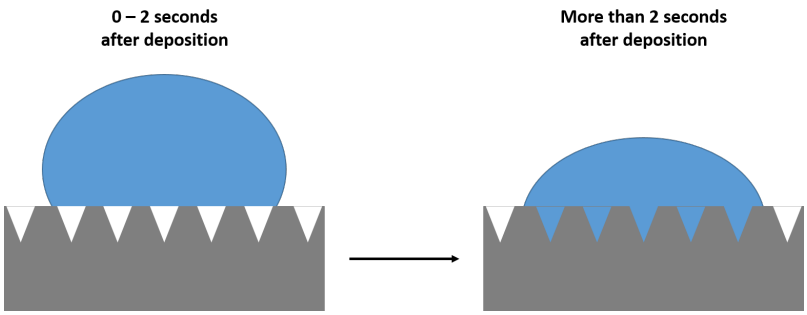

Figure 5.1: Illustration of assumed droplet behaviour on plasma cleaned samples with grid-textures (G and LG): Initially, the droplet does not wet the grid-valleys, resulting in a high contact angle, but after approximately two seconds, also the grid-valleys are wet, resulting in significantly reduced contact angle. This represents a transition from the Cassie-Baxter regime to the Wenzel regime.

As the described wetting transition only occurs after plasma cleaning, it is believed that dust particles, organics and other impurities in the grid-valleys contribute to the formation of a large energy barrier for the Cassie-Baxter to Wenzel transition. However, after removal of these impurities during plasma cleaning, this barrier is reduced significantly, thus allowing the transition to occur more rapidly. It is not know if the non-plasma cleaned substrates eventually would experience a similar transition, as the contact angles were recorded after only 4 s, and further studies should therefore investigate this. Interestingly, a similar transition after plasma cleaning was observed by Badge et al., when investigating how surface chemistry affected the wetting of gecko toe pads [142]. In this investigation, it was found that water droplets deposited on the untreated gecko toe pads behaved according to the Cassie-Baxter model, while droplets deposited on oxygen plasma cleaned toe pads showed Wenzel behaviour, explained by the removal of a surface layer of hydrophobic lipids. A transition in wetting state, as described above, also explains why the observed difference before and after plasma cleaning is less for samples R and L, as these have no such large valleys the droplet can penetrate into.

By comparing Figures 4.2 and 4.4, a clear relationship emerges: The samples with the poorest wetting (G and LG), are the ones with the highest average area surface roughness. This corresponds nicely with the observations made during this thesis' preceding project work [1], and with investigations done by Chen et al. on the effect of surface roughness on wettability for the deposition of Sn-Bi solders on Cu/Al_2O_3 substrates [143]. Despite this, the observations during this thesis work contradicts the Wenzel model outlined in Section 4.1.1, which says that if a smooth material is hydrophilic ($\theta < 90°$), the wetting should improve with increasing roughness. However, this can be explained if these two sample types instead follows the Cassie-Baxter model outlined in Section 4.1.1, which, as explained above, it seems like they do. As long as the droplets are unable to penetrate into the grid-valleys of the samples, the added roughness will not contribute to any enhancement of the wetting properties of the substrates, and a poorer wetting is expected. For samples R and L, both without the large grid-valleys, the relationship between wetting and roughness is as expected for the Wenzel model: Sample R, being the most rough of these two, also exhibits the best wetting properties.

5.1.2 Heat treatment of an uncoated, polished substrate

Images of the surface topography and the oxide-substrate interface of a polished, uncoated substrate treated with heating program $H-2$ are shown in Figure 4.5, and reveal the formation of a 700 nm thick oxide layer on the substrate surface. This seems to be consistent with observations by e.g. Lin et al. [67] and Kumar et al. [69], who both found that a thick oxide layer developed on Ti6Al4V when heated at high temperatures. The surface of this oxide layer seems uneven, with some porosity, similar to observations made by e.g. Frangini et al. [66] and Xu et al. [77] when studying the thermal oxidation of titanium substrates. From the interface image, some pores and cracks can be observed close to the interface layer, possibly resulting from stresses caused by thermal expansion mismatch, as discussed in Section 2.3.3. Additionally, dark speckles can be seen within the oxide layer, indicating the presence of a secondary phase, which also could contribute to the pore formation. A study by Frangini et al. on air oxidation of Ti6Al4V indicates that this secondary phase might be an alumina phase, originating from the oxidation of the aluminum in the substrate [66]. Based

on the findings of Frangini et al., oxidation of the vanadium is also expected to occur, but the resulting VO_2 phase will mostly be dissolved in the TiO_2 rutile phase, thus not appearing as a separate phase in the interface region.

The GI-XRD diffractograms of the heat treated substrates shown in Figure 4.6 identify the oxidation layer as one made up of TiO_2-phases, and do not show any sign of the secondary phase observed in Figure 4.5. Thus, it seems that the amount of secondary phase was too low to be detected, or that it was located too deep in the oxide layer, thus being completely concealed by the TiO_2-phases. Based on the location of the secondary phases in the oxide layer seen in Figure 4.5, it seems that the latter is true, which appears to contradict the findings of Frangini et al. [66]. This study found that the aluminum concentration in the oxide layer increased towards the oxide-air interface, but these tests were conducted over a significantly longer time scale (>100 h) than those carried out during this thesis work, which might explain the different observations. The diffractograms also show that temperature and duration of heating are significant factors for the development of the oxide layer. As the maximum temperature and the time spent at the elevated temperature is increased, more and sharper rutile peaks appear, indicating a more severe oxidation of the substrate. This corresponds well with the findings of Frangini et al. [66], Lin et al. [67] and Kumar et al. [69], who all found that the thickness of the TiO_2 oxide layer increased with increasing temperature. Furthermore, for all of the heat treated substrates, it is evident that the rutile phase is the dominating TiO_2-phase. This is comparable with the results from Feng et al., who found that heat treatment of a titanium sample to 600 °C converted the metastable anatase phase to the more stable rutile phase [65].

Figure 4.7 shows a representative example of a polarization curve measured on the polished Ti6Al4V substrate, heat treated with heating program $H-2$. It is evident that almost no polarization response was achieved, as the maximum polarization value was approximately $2 \cdot 10^{-4}\,\mu C\,cm^{-2}$. The recorded polarization is most likely an artefact caused by the currents flowing through the system, which, judging by the extremely small polarization value, also have to be very small. As expected, given that the space group of rutile is $P4_2/mnm$, being both tetragonal and centrosymmetric [144], no ferroelectric polarization response is recorded. Thus, any polarization response measured on the coated samples can be assumed to be a property of the coating layer, and not of the substrate.

5.2 Optimization of heating program

5.2.1 Substrate oxidation and phase purity of coated samples

When deciding what temperature programs to investigate for the calcination process, most weight was put on the limitation of substrate oxidation, while at the same time being able to produce a phase pure BT coating. The work of Bakken showed that it was possible to achieve phase pure BT above 600 °C [63], while Ræder et al. only achieved phase pure BT when the samples were calcined at 650 °C or above [16]. Both of these studies employed the same aqueous chemical solution deposition as the one used in this thesis work, thus providing a good foundation to build on. Based on their findings, temperature programs $H-1$ and $H-2$ were developed, consisting of heating each coating layer in air to a maximum temperature of 600 °C and 700 °C respectively, at which the samples were held for 6 min. Additionally, as it is known that the application of a coating might protect the substrates

against oxidation [145], it was decided to test temperature programs where the initial layers were calcined at 600 °C, while the remaining layers were calcined at 700 °C. This resulted in heating programs $H-3$ and $H-4$, where the first and the three first layers were calcined at 600 °C, respectively. For these two programs, it was believed that the low-temperature used for the initial heat treatment would result in calcined coating layers acting as oxidation protection for the substrate, while the higher temperature treatment for the last layers would ensure coatings with proper crystallinity. To investigate whether this was the case or not, GI-XRD measurements and FIB-imaging was carried out on the samples, and these results will be discussed in the following.

Based on the preliminary investigations into substrate oxidation, discussed in Section 5.1.2, it was expected that the selection of heating procedure would have an significant impact on the oxidation of the Ti6Al4V substrate. Indeed, Figure 4.8, showing the GI-XRD diffractograms of the coated, polished substrates treated with the four different heating procedures described above, reveals some important differences between the heating programs. Firstly, seen by the absence of most of the rutile peaks, it is clear that sample P_{H-1} has undergone less oxidation than the remaining three samples, where the rutile peaks are clearly present. This corresponds well with the discussions regarding the temperature dependence on oxide layer thickness in Section 5.1.2, where it was concluded that thicker layers corresponded to a more severe heat treatment. Furthermore, of the three remaining samples, sample P_{H-3} exhibits the sharpest rutile peaks, as well as the peak at $2\theta \approx 41°$, which is barely visible on the remaining samples, indicating that the oxidation was most severe on this sample. As the remaining samples, P_{H-2} and P_{H-4}, show more or less the same rutile peaks with the same sharpness, the degree of oxidation on these two samples seems indistinguishable. These indications are confirmed by the cross-section images of the coating-substrate interface regions of the samples, shown in Figure 4.9, and the measured layer thicknesses, shown in Figure 4.10, which reveal a thin oxide layer on sample P_{H-1}, slightly thicker oxide layers on samples P_{H-2} and P_{H-4}, and a thick and uneven oxide layer on sample P_{H-3}. However, all of the oxide layer thicknesses are significantly lower than that of the uncoated substrate treated with heating program $H-2$, discussed in section 5.1.2, indicating that the applied coating acted as a protection against oxidation during the calcining process. This corresponds well with findings of Yu et al., who found that the oxidation of Ti6Al4V in the temperature range of 600-700 °C was significantly lower when an amorphous SiO_2 film was applied to the substrate by the sol-gel method [145].

As mentioned, it was expected that the samples treated with heating programs $H-3$ and $H-4$ would result in less oxidation compared to the one treated with program $H-2$, as the inner layers of coating, processed at a lower temperature, were believed to act as a protection against substrate oxidation. However, both the GI-XRD results in Figure 4.8, and the oxide layer thicknesses obtained from Figures 4.9 and 4.10, showed that the oxide layer of sample P_{H-3} was significantly thicker than that of P_{H-2}, while the oxide layer of sample P_{H-4} was approximately as thick as the latter. The reason for this behaviour is not known for certain, but one hypothesis is related to the porosity of the oxide layer on sample P_{H-3}. This kind of porosity, with pores close to the metal-oxide interface, is similar to voids created by the Kirkendall effect, as a result of unbalanced ion diffusion rates at the interface [146]. Similar porous interface regions have also been observed by Poon between a Ti6Al4V substrate and a $CaTiO_3$ coating [147], by Mo et al. at the interface of stainless steel 316L and Ti6Al4V joined by diffusion bonding [148], and by El Mel et al. at the metal-oxide interface

of oxidized core-shell nanostructures [149]. These diffusion effects are typically more severe at higher temperatures, but in this case, the diffusion process seems to be activated by the heat treatment of the first deposited coating layer at a lower temperature of 600 °C. Thus, when heating the remaining eight layers at 700 °C, diffusion processes may happen readily, eventually creating a thick and porous oxide region. At the same time, it seems important that the innermost region of coating calcined at 600 °C is not too thick, as sample P_{H-4} does not experience the Kirkendall effect. This also seems reasonable, as it is known that diffusion processes are more rapid at shorter length scales. However, to make any conclusions on the exact origin of these pores, a more complete thermodynamic study or chemical analysis should be carried out on the system. This was attempted to do with EDS analysis of the interface region, but as the EDS investigations were inconclusive, no certain conclusion on the origin of the pores can be made.

Based on the thorough investigations on BT thin films produced by aqueous chemical solution deposition by Bakken [63], it was also expected that the differences in heating programs would affect the phase purity and crystallinity of the BT thin films. Once again, the GI-XRD diffractograms in Figure 4.8 make it possible to assess these properties of the coated samples. Firstly, it is evident that the sharpness of the BT peaks is highest for samples P_{H-2} and P_{H-3}, while samples P_{H-1} and P_{H-4} show broader and less evident peaks. This is a clear indication that heating of the samples at a maximum temperature of only 600 °C for 6 min is not sufficient to produce properly crystalline films, in accordance with the findings of Ræder et al. [16]. Additionally, it seems that the six calcinations at 700 °C was not sufficient to properly crystallize the three initial layers deposited at 600 °C, in addition to the remaining six layers at 700 °C, for sample P_{H-4}, although the crystallinity of this sample was better than that of sample P_{H-1}. Finally, it should be noted that the secondary phase phase observed in the cross-section image of the oxidized sample, shown in Figure 4.5, was not observed for the coated samples used in the heat treatment, neither in the electron microscopy images in Figure 4.9, nor in the GI-XRD diffractograms in Figure 4.8. Thus, it seems that the coating layer not only protects the substrate from severe oxidation, but also prevents the formation of secondary phases.

5.2.2 Substrate-coating interface

In order to assess the adhesion of the BT coating to the substrate, which is crucial for the intended application of the system, cross-sections revealing the coating-substrate interface were made and imaged by FIB. Representative images of this interface for the coated, polished samples treated with the different heating programs are shown in Figure 4.9, and reveal several important differences. Firstly, the coating layer of sample P_{H-1} appears smooth and dense, and only a thin oxidation layer has developed underneath it. Based on the interface, the adhesion of the coating appears mostly good, but with some longitudinal cracks (< 500 nm) at the coating-oxide interface. As outlined by Nix [99], and discussed in greater detail in Section 2.3.3, these cracks might be caused by thermal strains arising from the differences in thermal expansion coefficients during the coating calcination process. As BT has a greater thermal expansion coefficient than the Ti6Al4V substrate, the coating will be subject to tensile stresses during cooling, as shown in Section 2.3.3. Furthermore, as the coating undergoes densification during heating, while only thermal expansion occurs in the metal substrate, growth strains might also develop in the film [99]. Said growth strains

will be of the tensile type, thus making the coating prone to cracking during heating as well. These findings are similar to those of Wei et al., who investigated electrophoretically deposited hydroxyapatite coatings on Ti6Al4V substrates [72]. Hydroxyapatite, similarly to BT, has a larger thermal expansion coefficient than Ti6Al4V, and both growth strains during heating and thermal strains during cooling were identified as crack-forming mechanisms in this system. Furthermore the location of the cracks seen in sample P_{H-1} coincides with those found by Wei et al., who identified the coating-oxide interface and the oxide layer as weak links in the system. Similar cracking was also found on sample P_{H-4}, thus implying that also for this sample, the coating adhesion was slightly dissatisfying. For this sample, the cracks were wider and longer than those of P_{H-1}, which is believed to be a consequence of the increased heating temperature of sample P_{H-4} compared to P_{H-1}, which would enhance the crack-forming mechanisms discussed previously.

Similarly to the coating layers of samples P_{H-1} and P_{H-4}, the coating layers observed in Figure 4.9 for samples P_{H-2} and P_{H-3} appears dense and adhering to the substrate. Additionally, as can be seen in Figure 4.10, the coating layers for all of the samples have the same thickness ($\approx$120$\pm$20 nm), indicating a consistent coating procedure. This is slightly thinner than reported by Ræder et al. (180$\pm$6 nm for eight layers) [16], which can be explained by the increased spinning speed used in this thesis work. However, in contrast to the previously discussed samples, no longitudinal cracks at the coating-oxide interface can be observed for samples P_{H-2} and P_{H-3}. Instead, some pores (< 200 nm) can be observed, but these are not interconnected, and thus not expected to be immediately detrimental for the coating adhesion. These pores are believed to stem from local de-wetting of the substrate surface. This can be caused by imperfect polishing of the metal substrate, which can result in deep polishing grooves on a local scale. It is known that the size and shape of such defects is important for whether or not the solution will be able to fill the grooves [86], and if the solution is unable to do this, local de-wetting can occur, corresponding to a Cassie-Baxter regime as described in Section 2.4.2. Studies have also shown that the oxide layer that develops on the substrate surface during heating can be rough [77], which also is seen for the purely oxidized substrate in Figure 4.5. The local roughness variations of the oxide layer can contribute to the promotion of the Cassie-Baxter regime described above, thus enhancing the local de-wetting behavior. Similar partial de-wetting has also been observed by e.g. Zhang et al., who investigated spin-coated polyethylene thin films on rough silicon dioxide substrates [150]. A second possibility for the pore formation is that dust particles, or other organic impurities, have accumulated in the local rough features. During spin-coating, the coating layer will be placed on top of these impurities, which subsequently burn off during calcining, thus leaving behind a pore. However, as the samples were plasma cleaned before coating, and that the entire coating process was performed in a cleanroom, this explanation seems less plausible than the local de-wetting described above. Finally, the oxide layer of sample P_{H-3} is thick, having a highly porous oxide-substrate interface region. Based on the findings on Wei et al., this region is expected to be especially weak in terms of cracking [72], so even though the coating-oxide adhesion might be satisfying, the oxide-substrate adhesion might not be, thus ultimately reducing the final coating adhesion strength.

5.2.3 Scratch testing

To further investigate how the coating adhesion depended on the heating program, scratch tests were carried out on the coated, polished substrates. The average normal forces at failure for these samples, used to quantify the adhesion, are shown in Figure 4.11, and might indicate that heating programs $H-2$ and $H-4$ result in the best adhesion. Furthermore, heating program $H-1$ seems to result in the weakest adhesion, which is in accordance with the findings discussed in Section 5.2.2. However, there are several reasons to be cautious when drawing conclusions from the results concerning the normal force at coating failure. Firstly, the measured normal force at failure varied greatly from scratch to scratch on the same sample, as indicated by the large standard deviations of the measurements. Additionally, the recorded force-penetration depth curves showed a penetration depth that far exceeded the coating thickness, which is a clear indication that this scratch testing procedure is not suited for films with thicknesses in the nanometer range. Indeed, this type of scratch testing is mostly used for thick coatings in the micrometer range, as demonstrated by Kuo and Yen [104] and Nie et al. [105]. Furthermore, if the coating is not properly crystallized and hard, but instead amorphous and softer, scratch testing is not useful [151]. From the previous discussions regarding BT peak sharpness and phase purity in Section 5.2.1, the latter seems to be the case, thus making it very challenging to draw conclusions from the values on the average normal force at coating failure.

As the numerical results from the scratch tests were deemed inconclusive, it was decided to investigate the scratch marks with electron microscopy instead, in order to possibly find features and properties of the scratches that separated the different heating programs from each other. However, surface and interface images of the scratched samples in Figures 4.12-4.19, reveal only small differences between the samples. From the surface images captured at the beginning of the scratches, the coating of sample P_{H-1} appears mostly smooth with some cracks, while the surfaces of the remaining samples show no cracking. The cracking of the coating on sample P_{H-1} at an early point in the scratch path implies that a low force is required to cause coating failure, while the absence of cracks on the remaining three samples indicates a harder and stronger coating. This correlates well with the reflections made in Section 5.2.1, where it was found that the crystallinity of the coatings increased when increasing the maximum calcination temperature from 600 °C to 700 °C. However, the interface images of the samples reveal that coating delamination has not occurred at this point. From the same surface images, areas of surface discoloration can be observed early in the scratch path for samples P_{H-2}, P_{H-3}, and P_{H-4}. However, it seems that these darker areas are placed on top of the coating layer, thus probably being impurities on the indenter which was deposited onto the coating during scratching. This hypothesis is strengthened by the interface image of sample P_{H-3} in Figure 4.17a), which reveals a dark layer, with a color that corresponds to that of the oxide layer, which partially covers the coating.

When comparing all of the surface images captured at the end of the scratch path to images of wear traces on Ti6Al4V presented by Lin et al. [152], large similarities are seen: Both reveal a scratch with grooves and tears, and with the same alternating longitudinal lines of bright and dark color. Based on this, it is believed that all of the coating has delaminated at this point of the scratch. Indeed, the interface images of samples P_{H-2}, P_{H-3}, and P_{H-4} from the end of the scratch path reveal nothing but a bare substrate, where delamination of both coating and oxide layer has occurred. However, for sample P_{H-1}, some coating is embedded

in the substrate, as seen in Figure 4.13b). It is tempting to state that this is a sign of good coating adhesion, but upon closer investigation, several points contradicting this are found. Firstly, and perhaps most importantly, it is seen that the oxide layer has been removed from the substrate, which is impossible without removing the coating as well. Secondly, in the case of coating adhesion, the coating layer should be positioned on top of the substrate, and not be embedded within the substrate, as in this case. Therefore, it is more probable that the observed coating stems from an already scratched area of the sample that has been dragged along and pushed into the substrate by the indenter. A final point regarding the surface images of the scratch ends, is the absence of cracks running from the scratch towards the surrounding areas of coating. This indicates that the fracture toughness of the deposited BT coatings is good, which is important when bringing the coatings from the laboratory and into real-life applications.

Based on the discussion above, it appears to be difficult to draw any conclusions from the scratch images. All of the samples behave similarly, and the small differences between sample P_{H-1} and the remaining samples are not sufficient to directly assess the coating adhesion. It is not only challenging to accurately localize the point of coating delamination on the scratch trajectory, but also to determine where in the layered structure delamination occurs. This can happen at the coating-oxide interface or within the oxide layer itself, previously identified by Wei et al. as a weak link [72], or at the oxide-substrate interface. Closer investigations should therefore be carried out on this topic, as a knowledge of where in the system delamination occurs is important for improving the coating adhesion. However, this should not be done by conventional scratch testing, but instead by other techniques such as nanoscratch- and nanoindentation testing, which are frequently used when determining adhesion and mechanical properties of thin films [106][107][108][109]. From the discussion above, it is evident that neither numerical values for normal strength at coating failure nor captured images are conclusive in terms of adhesion, and the scratch tests were therefore disregarded in the final decision on the heating programs.

5.2.4 Testing of dielectric properties

The polarization curves for the samples treated with the different heating programs, which were used to determine the impact of heat treatment on the functional properties of the coatings, are shown in Figure 4.20. Large differences between the samples can be observed, where samples P_{H-1} and P_{H-4} display curves similar to those of a conductive material, where the polarization increases until the polarity of the electric field is inverted, and where the curves of samples P_{H-2} and P_{H-3} more closely resemble those of a lossy dielectric material. BT is expected to behave as a ferroelectric and with that dielectric material, but an explanation for the apparent conductive behaviour of samples P_{H-1} and P_{H-4} can be found in observations made during the measurements of these samples. Subsequently to the sputtering of the gold electrodes, it was observed that the edges of the electrodes deposited on samples P_{H-1} and P_{H-4} were more diffuse than those deposited on the two other samples. This might indicate that the mask used for the deposition of the gold electrodes was not completely tight, thus allowing a thin layer of gold to cover the entire surface of these samples. The gold layer would be conductive, thus explaining the unexpected conductive behaviour of samples P_{H-1} and P_{H-4}. This conductive behaviour is also the reason for why the maximum polarization values are so high for samples P_{H-1} and P_{H-4},

while the dielectric samples P_{H-2} and P_{H-3} show polarization values in a more reasonable order of magnitude. Despite exhibiting dielectric behaviour, the latter samples do not show the expected ferroelectric behaviour. However, this is in agreement with observations made by Bakken on 193 nm thick polycrystalline BT films, produced by the same aqueous chemical solution deposition method as in this thesis [63]. Based on the small grain size in her thin films, Bakken was able to explain this lack of ferroelectricity. It is known that with a reduction in grain size, the crystallographic distortion is reduced, which is associated with a loss of the ferroelectric response [57], and this seems fitting for the films produced during the current work as well.

The polarization curves for samples P_{H-2} and P_{H-3}, shown in Figure 4.20, are narrow, thereby indicating that the samples had a only low leakage current. This is a great advantage for the application of the films, and similar narrow curves were also measured on the films produced by Bakken [63]. This low amount of leakage indicates some unexpected current flowing through the dielectric coating, and might stem from the film itself, or from surface charges on the metal substrate. Additionally, impurities such as water on the sample surface might contribute to the leakage current, although this is unexpected. Finally, the wide and obviously leaky curves of samples P_{H-1} and P_{H-4}, are not due to any small or unexpected artefacts of the system. In this case, the apparently conductive surfaces of the samples actually allow current to flow, thus being the main reason for leakage.

As explained in greater detail in Section 4.2.4, dark brown/black spots appeared on sample P_{H-3}, and only this sample, when touched with the probe tips used when doing the dielectric measurements. These dark spots indicated that some kind of conduction process took place within the layered system, which might be detrimental for the functionality of the samples. Based on the type of observations, as well as the time between the observations, as outlined in Figure 4.22, it was initially believed that the spots were a result of a reversible reaction, allowed by an unknown factor that diminished with the time passed since sample production. One such unknown factor could have been the migration of oxygen vacancies upon the application of an external electric field. Such vacancies are among the most common defects in semiconducting metal oxides, and can be generated by the presence of impurities or dopants, and by heat treatment in oxygen-deficient atmospheres [135]. The latter is the case for the cooling-step during calcining of the coated samples in this work, while it is possible that impurities have been present in the chemicals and powders used for making the BT precursor solution. It is also known that the presence of oxygen vacancies can cause color changes from white to black [153][154][155], which corresponds nicely with the observations made when testing sample P_{H-3}. Studies have also found that this color change is reversible over time [136][154], which support the time-dependent hypothesis outlined for this work. As the sample was stored in ambient atmosphere, it is expected that any oxygen vacancies eventually would be annihilated by the oxygen in the air [136], which might explain why the spots no longer were observed when tested nearly four months after the coating of the sample, and over six weeks after the spots lastly were observed. It was therefore decided to anneal sample P_{H-3} in N_2 atmosphere at 400 °C for 4 h, to try to reintroduce the oxygen vacancies. However, when re-testing the dielectric properties of the sample, no spots were observed, neither was there any significant difference between the polarization curves before and after annealing in N_2 atmosphere, as shown in Figure 4.21. This indicates that either the annealing process was not carried out at sufficient temperature and duration, or that migration of oxygen vacancies is not the sole cause for

the spot formation. The former seems unlikely, as 400 °C has been reported to be sufficient for the creation of oxygen vacancies [136][156], and the oxygen migration hypothesis is thus weakened. Overall, the fact that the textured samples, albeit treated with program $H-2$ instead of $H-3$, showed no signs of spotting when tested only one week after the completed coating procedure, further weakens the general hypothesis regarding a time-dependent reaction.

A second hypothesis that might explain the formation of spots on the sample is charge injection, with associated reactions, at the different interfaces of the system. Whether or not this is possible depends on the type of electric contacts formed at the interfaces, as outlined in Section 2.6.2. In the Ti6Al4V - TiO_2 - BT - Au system of this thesis, there are three distinct interfaces, and each of their contact types must therefore be evaluated. Firstly, the bottom-most contact in this system is the Ti6Al4V-TiO_2-contact between the Ti6Al4V substrate and the TiO_2 oxidation layer on top of it. By carrying out ultraviolet photoemission spectroscopy, Kim and Rhee found the work functions, Φ, of Ti and TiO_2 to be 3.9 eV and 4.05 eV respectively [157]. No values have been found for the Ti6Al4V alloy, but it is expected to have a similar work function as the pure titanium metal. Furthermore, due to the presence of oxygen vacancies, TiO_2 is generally regarded as an n-type semiconductor with a wide band-gap [158][159]. Thus, as this contact consists of an n-type semiconductor with a larger work function than the metal, the contact is expected to show Ohmic or, as the difference in work functions is small, slightly Schottky type behaviour. As a consequence of this, no (or a very small) Schottky barrier is expected, and charge injection should be quite easy at this contact.

The second contact in this system is the TiO_2-BT-contact between the TiO_2 oxidation layer and the piezoelectric BT coating. Here, TiO_2 is still assumed to be an n-type semiconductor, while the semiconductor type of BT is more unclear. On one side, unintentional doping from impurity cations in the raw materials might result in a p-type semiconductor. These cations typically have a lower valency than the host cations they replace and contain less oxygen per cation, and are therefore acceptor impurities. These acceptor impurities create negatively charged acceptor sites, which must be compensated by oxygen vacancies, as given by

$$\text{(e.g.) } Fe_2O_3 \xrightarrow{2\,TiO_2} 2\,Fe'_{Ti} + 3\,O^X_O + V^{\cdot\cdot}_O \cdot \qquad \{4\}$$

The resulting oxygen vacancies represent sites where new oxygen can be incorporated, making it possible to obtain a stoichiometric excess of oxygen in the material, which results in p-type conduction [160]. However, on the other side, a deficiency of oxygen would result in n-type conduction [160]. This situation might occur if the temperature treatment of the BT layer has been carried out in an oxygen-deficient atmosphere [135], which partly is the case for the BT coatings in question. After being heated to maximum temperature, the samples were cooled in N_2-gas, allowing the following reaction to take place:

$$O^X_O \longrightarrow \frac{1}{2}O_{2\,(g)} + V^{\cdot\cdot}_O + 2\,e', \qquad \{5\}$$

where the resulting electrons give rise to n-type conductivity. As parts of the thermal processing were carried out in an oxygen-deficient atmosphere, and as the purity of precursors was high, it is assumed that the BT layer is in an oxygen-deficient state, thus being n-type.

From the literature, a work function, Φ, of approximately 4.0 eV has been found for BT [161], while the corresponding value for TiO_2 is still assumed to be 4.05 eV [157]. Due to

the similarity in work functions, little band bending is expected to occur, and no injection barrier of significant size should develop between the two layers. Thus, the contact is assumed to be Ohmic-type, and charge injection should be easy at this interface.

Finally, the upper-most contact in this system is the BT-Au-contact between the BT layer and the top gold electrode. Kim and Rhee reported a work function, Φ, of 4.85 eV for gold [157], while the corresponding value for BT is approximately 4.0 eV [161]. Zhang et al. have also reported an electron affinity, χ, of 3.9 eV for BT [162]. It is still assumed that BT acts as an n-type semiconductor, meaning that the BT-Au-contact now consists of an n-type semiconductor with a work function that is significantly smaller than the work function of the metal. This results in a Schottky-type contact, and from Equation 2.4, the large difference in metal work function and semiconductor electron affinity results in a correspondingly large Schottky barrier. Thus, charge injection at this contact is expected to be difficult. To summarize the discussions above, Table 5.1 provides an overview of the different contacts, and whether or not charge injection is expected to be easy.

Table 5.1: An overview of the contacts and contact types in the Ti6Al4V - TiO_2 - BT - Au system.

Contact	Work functions	Contact type	Charge injection
Ti6Al4V-TiO_2	Similar	Ohmic	Easy
TiO_2-BT	Similar	Ohmic	Easy
BT-Au	$\Phi_{Au} > \Phi_{BT}$	Schottky	Hard

Based on the information in Table 5.1, charge injection should be easy at all interfaces, except from the interface between BT and the gold electrodes. This also strengthens the theory of conduction processes occurring in the system, which might counteract the build-up of surface charges, and contribute to the oppression of ferroelectricity discussed previously in this section. Such a charge injection can cause local changes in the oxidation number of titanium, and with this change, a change in color is also expected. However, as all of the samples have the same contact types, but only sample P_{H-3} showed spotting when tested, charge injection alone is not a sufficient explanation for the spots. As the observations are not reproducible, it is therefore believed that one or more accidental or random artefacts, in cooperation with the charge injection, causes the spotting of sample P_{H-3}. One such artefact might be the introduction of some kind of impurity during the spin-coating process, which disappears over time, thus also explaining the time-dependent behavior of when the spots were observed. Trapped water or moisture is therefore a likely candidate impurity, as it might evaporate and dry out over time, thus only allowing spots to be observed before it is evaporated.

5.3 Properties of coated textured substrates

5.3.1 Surface roughness and texture

When comparing the area surface roughness values of the textured samples before and after coating, as shown in Figure 4.23, the coating process appears to have resulted in a slight decrease of surface roughness for all texture groups, except for L. This slight decrease can be explained by coating partially filling dips and valleys on the substrates, and is therefore

expected. Furthermore, visual observations of sample group L revealed a significant amount of macro-scale blisters, which would artificially increase the roughness value for this texture group, and explain its discrepancy in roughness behaviour. However, as all changes in area surface roughness values are small, it seems that the substrate texture is mostly retained after coating. This is also confirmed by the topography height profiles in Figure 4.24 and the electron microscope images in Figure 4.26, both giving overviews of the coated, textured samples. From these figures, it is clear that the polishing stripes on the reference substrates are present, as are the grid lines on samples G-3 and LG-3, and the nanotextured pattern on sample L-3. This strongly implies that spin-coating is a highly suitable procedure for producing coated implants where the initial texture of the substrates is retained after coating, which is important for bone fixation, as well as cell adhesion, proliferation, differentiation and detachment strength [81][82][83]. However, the same figure reveals that the polishing stripes on the flat surfaces of sample G-3, which are clearly visible in the example images of the uncoated samples in Figures 3.1 and 4.1, have been filled and concealed. This also fits well with the observations from the example topography height profile of a sample from texture group G, as shown in Figure 4.24. Thus, it seems that surface features must have a topographical size above a given threshold value in order to not be concealed, which fits well with the findings of e.g. Stillwagon et al. [90] and Gu et al. [163], who both investigated planarization of spin-coated substrates with topography. Furthermore, as the substrate texture is mostly retained, it seems that the spinning speed was sufficiently high, that the concentration of the BT precursor solution was sufficiently low, and that the time spent between completed spinning and start of curing was suitable, as discussed in Section 2.4.3. However, as seen in the interface images of samples G-3 and LG-3 in Figures 4.34 and 4.38 respectively, the coating layer was obviously thicker in the bottom of the grid-valley compared to on the flat surface. Thus, it is clear that the processing parameters can be refined further, to get an even better retention of the surface texture.

5.3.2 Phase purity

From the GI-XRD diffractograms of the coated, textured substrates, shown in Figure 4.25, it is difficult to draw any clear conclusions regarding phase purity and crystallinity of the coatings. All of the texture groups show the most important peaks for BT, rutile and the substrate, with some differences in intensity and sharpness. It seems that sample R-1 is the most crystalline, as indicated by the sharpness of the BT peaks, while sample L-1 is the most oxidized, judged by the rutile peaks. However, peak broadening is a common phenomenon when dealing with grains and crystals on the nanoscale [164], meaning that even the broad BT peaks observed for samples G-1 and LG-1 might correspond to a highly crystalline material, but with small crystallite sizes. Precisely this is confirmed when investigating the surface images of said samples, shown in Figures 4.31 and 4.35, which reveal substantial growth of small grains on the sample surfaces. Due to this, it is not straightforward to draw any conclusions regarding crystallinity solely based on peak sharpness. Furthermore, as mentioned previously, caution must be taken when comparing GI-XRD diffractograms carried out on samples with different topographies. The texture on the substrates itself might interact with the incident beam, especially in GI-XRD where the incident angle is low, thus resulting in uncertainty of the measurements.

In addition to the BT, rutile and substrate peaks, as mentioned earlier, indications of an anatase minority peak can be seen for all of the samples. This corresponds well with the observations made for the uncoated sample treated with heating program $H-2$, as seen in Figure 4.6 and discussed in Section 5.1.2. Furthermore, a peak corresponding to a secondary phase is observed on all of the samples in texture group G, but not on any of the other samples. This peak fits well with that recorded for barium aluminium titanium oxide in the PDF- 4+ database. How this phase is formed is not known for certain, but a possibility is that that the deposited BT precursor solution reacts with the aluminum oxide in the substrate oxide layer, ultimately resulting in some sort of aluminum-enriched barium titanate. Interestingly, the appearance of this secondary phase coincides with observations on Figures 3.1 and 4.26, where the center areas of the flat surfaces of sample group G appear darker than the areas closer to the grid lines, whereas the color of the other texture groups is homogeneous. Furthermore, the tetragonal shape of the crystals on this sample, seen in Figure 4.31, deviates greatly from the spherical grains observed for the other texture groups. This might be a consequence of preferential growth, possibly resulting from local orientation of the metal grains, but as this effect is only observed on this texture group, it seems unlikely. Therefore, it is more plausible that the differences are related to the observed color differences on substrates of texture group G. It is known that laser-patterning can result in structural and chemical changes on the metal substrates [165][166][167], and these changes might therefore have promoted the formation of a secondary phase with the tetragonal crystal structure.

5.3.3 Coating microstructure and substrate-coating interface

For the heat treatment of the textured films, heating program $H-2$ was used, for reasons discussed in Section 5.2. This heating program employed a heating rate in air of $1.67\,^{\circ}\mathrm{C\,s^{-1}}$ to a maximum temperature of 700 °C, where the temperature was held constant for 6 min, which is similar to the heating program Bakken used to produce polycrystalline thin films on smooth substrates of substrates of $SrTiO_3$ and platinized silica [63]. It was therefore expected that the microstructure of the coatings deposited on the smoothly-polished reference samples (R) would resemble the structure of small spherical grains with some porosity in-between the grains in the films created by Bakken. However, this is not entirely the case, as can be seen in Figure 4.27. Some spherical grains can be observed, as in the case of Bakken, but these are mostly present on the hills and ridges of the surface. Contrary to Bakken, smooth areas with no apparent grain growth are present on the reference samples, and these smooth areas are instead highly porous, perhaps indicating that the coating here is somewhat amorphous. This is most likely caused by the features of the substrate itself, where the polishing process has resulted in an uneven surface with grooves and ridges. In the seconds between spin-coating end and curing start, gravitational and capillary forces will pull solution from the areas of higher altitude and into the polishing grooves [90], resulting in a thicker layer of solution in the grooves, and a thinner layer on the hills and ridges, as illustrated in Figure 5.2a). In the areas where the solution layer is thin, the reactions involving decomposition, burn-off of organics, and BT nucleation and growth, as described in Section 2.3.2, can happen easily, resulting in areas with distinct BT grains. However, in the areas where the solution layer is thicker, the time spent at maximum temperature might not be sufficient for a complete conversion of solution to crystalline BT. This can eventually result in the areas of a smooth and highly porous coating, seen in

Figure 4.27. Likewise, the pores observed at the surface of these areas are most likely a consequence of the thick layer of solution, where gaseous species forming at the lower areas of the solution layer moves through the upper areas of the film, which due to their position are more readily exposed to the heat and thus firmer, ultimately resulting in pores at the gas exit positions. Several studies regarding the effect of coating thickness on crystallinity can be found in the literature, as exemplified by a study by Dutta et al., who investigated the deposition of ZnO thin films on glass substrates by sol-gel drain coating [168]. Contrary to what was found in this thesis work, this study found that the crystallinity increased with increasing concentration, and thus thickness, of the coating solution, echoing the findings of several other studies found in the literature [169][170]. This strengthens the hypothesis suggested for this thesis, that the observed poor crystallinity in the areas of a thicker coating layer is a consequence of insufficient calcining duration or temperature, and not an inherent property of the coating system itself.

A similar reasoning relating to the thickness can be used to describe the microstructure of the remaining textured samples. For sample L, a LIPSS-pattern has been applied to the polished substrate, and the resulting surface texture of the uncoated substrate, revealed in Figures 3.1 and 4.1, consists of a periodic pattern of ridges and valleys. In the time between spinning stop and curing start, gravitational and capillary forces are able to pull solution from the ridges and into the valleys, ultimately resulting in a thicker solution layer in valleys compared to on the ridges. This situation is directly comparable to that discussed for sample R, and results in a smooth, porous coating in the lower-lying areas, while a crystalline coating of spherical grains is found at the ridge areas, where the solution layer was thinner, as seen in Figure 4.29. Samples G and LG, with flat surfaces identical to those of R and L respectively, seems to behave in the exact same way, but with one important difference, namely the grid lines. Now, instead of accumulating in the small valleys between the surface features, excess solution will be drained into the deeper valleys of the grid lines, resulting in an overall thinner coating layer on the flat surfaces, as shown in Figure 5.2b). As discussed before, this is believed to allow for a more complete reaction with accompanying grain growth, and can explain why the entire flat surface is dominated of grains, without smooth and porous areas. This can be seen in Figures 4.31 and 4.35 for sample G and LG respectively, and is similar to what Bakken found on her smooth substrates [63]. In the deeper grid-valleys, however, where all of the excess solution has been drained, the solution layer prior to calcining will be thick. Therefore, as described before, these areas will appear smooth and highly porous, which indeed can be seen in Figures 4.33 and 4.37 for samples G and LG respectively. It should be noted that the reflections regarding varying thickness on the flat surfaces compared to the grid-valleys is not only hypothetical, but are largely confirmed by Figures 4.34 and 4.38, which clearly reveal a thick and porous coating layer at the bottom of the grid-valleys, which densifies and becomes thinner towards the top of the valleys.

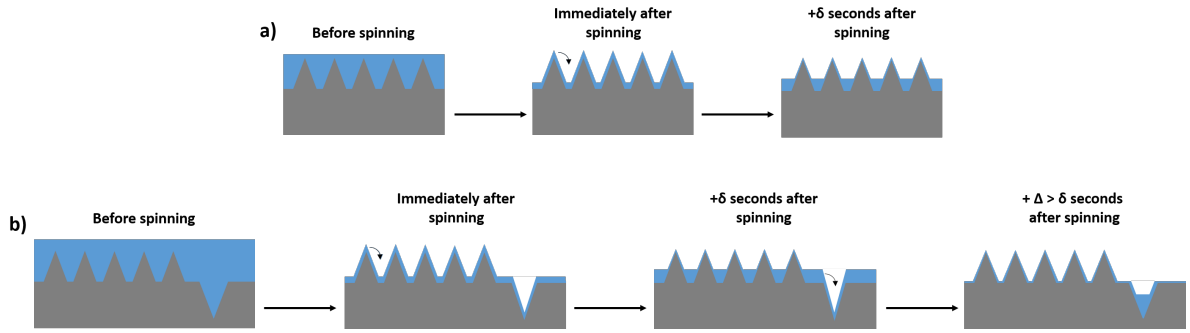

Figure 5.2: Illustration of distribution of solution for samples a) R and L, where the solution drains into local grooves and small valleys, and b) G and LG, where the solution ultimately drains into the deep grid-valleys, resulting in a thin, even layer. δ and Δ are time-parameters, and will depend on factors like solution viscosity, concentration, curing parameters, and more. It should be noted that the dimensions of the grid-valley in reality far out-scales the dimensions of the surface ridges, being a more effective "drainer" than what the sketch shows.

As for the samples tested during the determination of the heat treatment, the adhesion of the coating to the textured samples was qualitatively determined by assessing the interface region. For this determination, both the oxide-substrate interface and the coating-oxide interface were important, as delamination in any of these regions would result in the removal of the coating layer. Investigating the oxide-substrate interface first, Figures 4.28, 4.30, 4.32, 4.34, 4.36, and 4.38 reveal a highly porous oxide-substrate interface for all of the texture groups. As discussed in Section 5.2.1, this porous region is most likely created by the Kirkendall effect, which is related to differences in diffusion rates across the interface. It is known that such porous regions are weaker than the dense material [41][72], and limit the adhesion during loading. The total thickness of the oxide layer appears similar for all texture groups, but from the aforementioned figures, it seems that the porous interface region itself is less prominent for samples L and LG compared to the remaining samples. This might relate to the local heating and ablation processes during laser-patterning of the LIPSS-texture, which are known to cause structural and compositional changes to the substrate regions to be patterned [165][166][167]. Thus, it seems that the oxide-substrate interfaces of samples L and LG are stronger than those of R and G, possibly resulting in a higher load required for delamination.

From all of the interface images, it is clear that the coating thickness and appearance is not homogeneous, but that it varies greatly from position to position on the same sample. Figure 4.28 of the reference sample illustrates this especially well, where the coating layer appears smooth and dense in one of the cross-sections, while the coating and oxide layers are more interlocked with each other in the other cross-section. This indicates that the coating appearance and behavior is heavily dependent on the local topography of the sample, and not only the overall sample texture. Nevertheless, for both of the interfaces, no cracking can be observed at the coating-oxide interface, thus indicating that the adhesion here is good. Furthermore, it can be argued that the local adhesion in Figure 4.28b) is better than that in Figure 4.28a), as the intermixing of coating and oxide layers generates a larger coating-oxide interface, thus requiring more energy for delamination, as explained by Xu et al. when investigating hydroxyapatite/TiO_2 coatings deposited on titanium substrates [77]. Also the interfaces of texture group L, shown in Figure 4.30, display satisfying coating-oxide interfaces, with no signs of cracking and pores. From this figure, it is clear that the coating

fills the nanosized, periodic valleys on the surface nicely, providing mechanical interlocking between the coating and the underlying oxide layer. This, combined with the increased area of the coating-oxide interface provided by the wave-structure, is expected to result in an especially good adhesion between the coating and the oxide.

For the coating-oxide interface of texture group G, large differences can be observed between the flat surfaces and the grid-valleys. For the flat surfaces, shown in Figure 4.32, almost no bright coating layer can be observed. Instead, the images reveal a darker region close to to the platinum layer, which can not be seen for any of the other samples. This seems to fit well with the observations made in Section 5.3.2, where the presence of a secondary phase with a tetragonal crystal structure was discussed. The lack of any bright coating layer on the surface might imply that the wetting has been poor, resulting in the spin-off of all of the solution. However, the GI-XRD results in Figure 4.25 confirm the existence of a BT phase on this sample group, implying that the wetting must have been at least acceptable. Furthermore, no cracks or pores in the upper layer of the flat surfaces of sample G are observed, implying a good adhesion. This is also true for the grid-valleys of sample G, as can be seen in Figure 4.34. Even though the thickness and the porosity of the coating layer varies through the valley, the quality of the coating-oxide interface seems good at all positions, thus implying good adhesion. Finally, the flat surfaces of texture group LG, shown in Figure 4.36, show large similarities to those of group L. Also in this case, no cracks or pores can be observed at the coating-oxide interface, and the presence of coating in the valleys of the periodic wave-structure provides means for mechanical interlocking between the coating and the oxide layer. Thus the coating adhesion on the flat surfaces of texture group LG is expected to be stronger than that of sample G, in the same way sample group L is expected to have a better adhesion than sample group R. For the grid-valleys of sample LG, shown in Figure 4.38, the appearance of the coating-oxide interface looks mostly good, with correspondingly good adhesion, except from in the bottom of the valley. Here, large pores can be observed at the coating-oxide interface, which ultimately are expected to weaken the adhesion strength.

The absence of pores at the coating-oxide interfaces is a clear indication that the wetting properties of the textured substrates after plasma cleaning, as shown in Figures 4.3 and 4.4, were sufficient to get complete wetting of the surface. This seems to be true for all samples, except for in the grid-valleys of texture group LG, where large pores were observed at the coating-oxide interface. These pores seem reminiscent to what is observed for Cassie-Baxter behavior, as discussed in Section 2.4.2, and might indicate that the wetting at this point was poor. This poor wetting seems to be a result of the combination of both the nanosized features of the LIPSS-pattern and the more macroscopic grid-pattern, as neither texture groups L or G experience this problem. However, when moving up towards the top of the valley, the interface pores disappear, implying a better wetting. Based on this, it is hypothesized that the wetting shows Wenzel behavior with respect to the larger grid-valleys, while it shows partially Cassie-Baxter behavior with respect to the LIPSS-texture within the grid-valleys. These regimes counteract each other, as complete wetting of the grid-valleys is desired for the Wenzel regime, while de-wetting of the wave-pattern in the bottom of the grid-valleys is desired for the Cassie-Baxter regime, and an equilibrium state similar to that shown in Figure 5.3 is therefore expected to arise. A possible explanation for this behaviour is that the plasma cleaning, which in principle should remove all hydrophobic organic impurities [89][142], has not succeeded in cleaning the bottom of the grid-valley sufficiently. This might happen if dust and impurities are more strongly trapped in the bottom of

the valleys compared to towards the flat surfaces, or if the combination of nanotexture and grid-texture prevents the oxygen-plasma from properly reaching the bottom of the grid-valleys. Alternatively, the pores can be explained in terms of the transition from a Cassie-Baxter regime to a Wenzel regime, as discussed in Section 5.1.1: If the solution is cured more rapidly than the time it takes for the transition to occur, non-wetting behavior is expected in the bottom of the LIPSS-textured grid-valleys. A third possible explanation for the interface pores, which is not based on wetting properties, is related to the thickness of the solution layer prior to calcination. As described previously, solution is expected to accumulate in the bottom of the valleys, resulting in a thick layer. Upon calcination, pores might form in the coating layers as gaseous species exit, and these pores might propagate into new layers of coating. However, as the interface pores are not seen for texture group G, which also experience solution accumulation, this explanation seems unlikely.

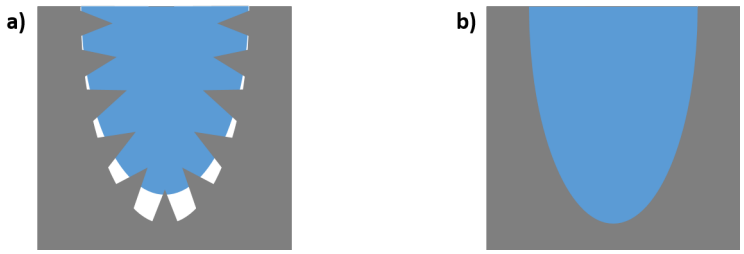

Figure 5.3: Hypothesized wetting behavior within the grid-valleys of samples a) LG, showing partially Cassie-Baxter behavior, and b) G, showing Wenzel behavior.

5.3.4 Testing of dielectric properties

Top-to-top measurements

As seen in Figure 4.41, similar polarization responses were generated for all of the coated, textured samples, when measured top-to-top. The cigar-shaped polarization curves reveal that the coatings were dielectric, as expected, but no ferroelectric response can be observed. This echos the curves produced for the samples made with the different heating programs, discussed in Section 5.2.4, and also resembles measurements made by Bakken of polycrystalline BT thin films spin-coated onto substrates of $SrTiO_3$ and platinized silica [63]. As for the differently heat treated samples, it is believed that this lack of ferroelectric response stems from the small grain size of the samples, revealed in the microstructure images in Section 4.3.3, which is known to suppress ferroelectric behaviour [57].

By comparing the polarization responses of the textured samples in Figure 4.41 to that of the uncoated, oxidized sample in Figure 4.7, it is evident that the BT coating has improved the polarization response by several orders of magnitude. This also reflects the fact that BT, having a non-centrosymmetric crystal structure, is expected to generate a polarization when exposed to a electric field, as opposed to TiO_2, which is centrosymmetric. Finally, some leakage was observed for all of the textured samples, with samples L-2 and LG-2 suffering most from this phenomenon. Such leakage is not uncommon, and might be a result from the quality of the film itself, or from surface charges on the metal substrate. In addition to this, surface impurities such as water might contribute to the leakage current, but this is not expected to be a problem in this case. Also poor electrode deposition can cause leakage currents, as seen for samples P_{H-1} and P_{H-4}, and discussed in Section 5.2.4. However, as

the electrode deposition method was more successful for the preparation of the textured samples, evidenced by the observation of sharp and distinct electrodes, also this problem was eliminated.

Top-to-bottom measurements

During the investigations on the observations of dark spots on sample P_{H-3}, described in more detail in Sections 4.2.4 and 5.2.4, a deep-dive was made into the different types of the electric junctions and contacts in layered system. Hoping to gain more knowledge about the system in question, it was therefore decided to do tests to investigate this more closely on the textured substrates. However, due to electrons flowing through the interfaces in both directions at the same time for the standard top-to-top measurements, as shown in Figure 5.4a), it was decided that the measurements should be conducted top-to-bottom instead. Thus, as shown in Figure 5.4b), the electron flow across the junctions would be in only one direction for the forward bias, and the other direction for reverse bias. In that way, it should have been possible to detect any differences between the forward and the reverse bias response.

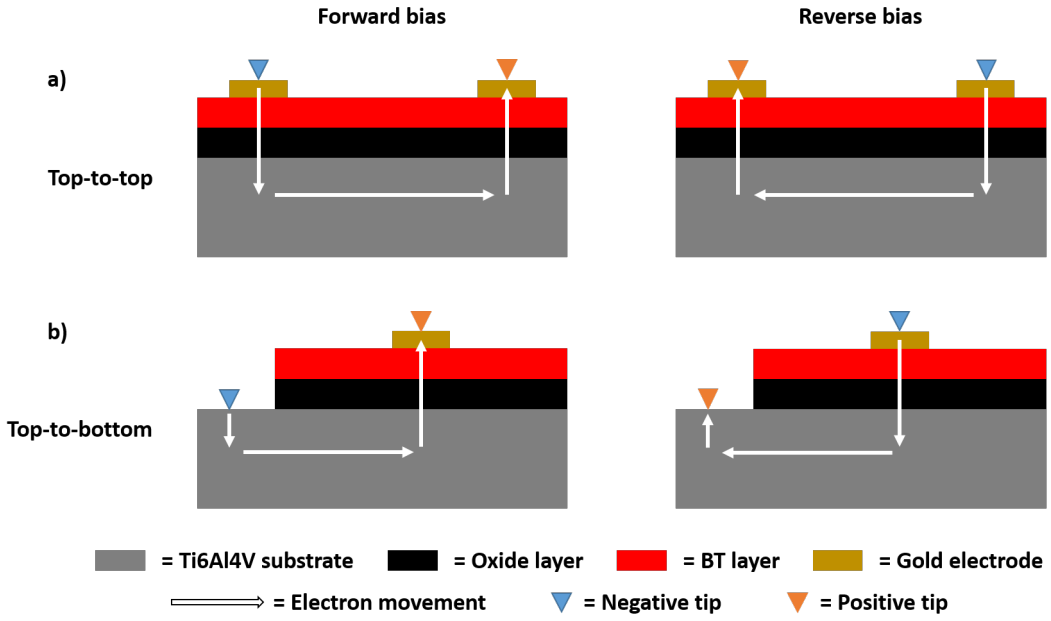

Figure 5.4: Schematic illustrating electron movement during dielectric testing during forward and reverse biases in the top-to-top and top-to-bottom measurement regimes.

As the contact between the gold electrode and the BT layer should be of the Schottky type, as shown in Table 5.1, a Schottky barrier is expected to develop here, which in turn should cause detectable differences between the forward and reverse bias regimes. However, as seen in Figure 4.42, the measured polarization curves are still symmetric, thus contradicting this expectation. A possible explanation for this is that the applied voltage provides sufficient energy for the electrons to overcome the Schottky barrier, in principle rendering it Ohmic. Therefore, based on these measurements, it is difficult to draw any conclusions regarding the contact types in the system.

Several studies have shown that the use of asymmetric electrodes, i.e. electrodes of different materials, might cause shifting of the ferroelectric hysteresis loops [171][172][173]. According to Lee et al., who did physical modelling of an asymmetric electrode setup, this shifting is explained by the difference in work functions of the electrodes [171]. This difference generates internal electrical fields in the system, thus favoring one of the polarization directions over the other. Similar shifting was found by Umeno et al., who made *ab initio* calculations on $PbTiO_3$ with symmetric and asymmetric electrode combinations of Pt and $SrRuO_3$ [172]. This effect has also been found in experimental work, e.g. for polarization measurements of BT thin films deposited on a metallic $La_{2/3}Sr_{1/3}MnO_3$ (LSMO) bottom electrode on a $SrTiO_3$ (STO) substrate by Liu et al. [173]. When measuring between a Pt top electrode and the bottom LSMO electrode, one of the polarization directions were favoured, resulting in asymmetrical polarization curves. As an asymmetric electrode setup was used for the top-to-bottom measurements in this thesis work, a similar shifting effect of the polarization curves was expected. However, as can be seen in Figure 4.42, no such distinct shifting is observed, when compared to the top-to-top measurements in Figure 4.41. One possible explanation for this is that the BT coatings in this work are not ferroelectric, as discussed previously, contrary to those of the aforementioned studies. Furthermore, the electric field calculations in this thesis are based on approximations of the coating thicknesses, and any errors in these approximations might conceal a shifting effect.

6 Conclusion

In this work, polycrystalline $BaTiO_3$ thin films have successfully been deposited on Ti6Al4V substrates by means of aqueous chemical solution deposition and spin-coating. The work showed that it was possible to use spin-coating to coat laser-patterned substrates with a wide range of surface textures, and still have a retention of the surface textures after coating.

Among the tested heating programs, preliminary investigations of substrate oxidation, $BaTiO_3$ phase purity and crystallinity, coating adhesion, and polarization curves showed that heating of each deposited coating layer to a maximum temperature of 700 °C in air resulted in the best coating properties. After dwelling at maximum temperature, it is recommended to cool the samples in oxygen-free atmosphere, in order to limit substrate oxidation. As it significantly improved the wetting properties of the substrates, converting them from non-wetting to wetting, plasma cleaning prior to spin-coating was deemed essential for the final coating quality.

GI-XRD investigations revealed few differences between the phases on the texture groups, with $BaTiO_3$, rutile, and substrate peaks dominating the diffraction patterns. However, signs of an unknown secondary phase, hypothesized to originate from the reaction between the precursor solution and aluminum in the substrate, was found for texture group G, but not for the other samples. This was to a large degree confirmed by electron imaging of the coated samples, which revealed unexpected tetragonal crystals on sample G. It is believed that this secondary phase is formed as a consequence of structural and compositional changes on the substrate surface during laser-patterning, but more investigations must be done to reveal its exact origin.

Upon microstructural investigations, a clear correlation between coating thickness and grain growth was observed, where areas with a thin coating layer clearly displayed grain growth, and where areas where the coating was thicker appeared smooth and porous. It is believed that the thickness inhomogeneities result from differences in surface topography, where in the time between spinning stop and curing start, deposited solution flows from higher- to lower-lying areas. The grid-pattern on samples G and LG seems to drain solution from the flat surfaces and into the valleys, resulting in significant grain growth on the former, and a smooth and porous surface in the latter. To improve the thickness homogeneity, it is recommended to use a more viscous solution, or to adapt a system that allows for curing initiation slightly before the spinning procedure is completed.

In general, investigations of cross-sections made in the coating by FIB reveal than none of the samples show any cracking at the coating-oxide interface, indicating that the adhesion between these layers is quite good for all textures. Due to their LIPSS-texture, samples L and LG experience a larger coating-oxide interface area, as well as mechanical interlocking between coating and oxide layer, and are therefore expected to show improved adhesion at this interface compared to their polished counterparts. Texture groups L and LG also showed a less porous oxide-substrate interface region than samples R and G, implying that the coating adhesion of samples L and LG is better at this interface as well. The large pores observed at the coating-oxide interface in the bottom of the LG grid-valleys might prove detrimental to the final adhesion strength of texture group LG, whereas no pore-related adhesion problems are expected for the coating-oxide adhesion of the other samples. However, without doing proper nanoscratch or nanoindentation tests, it is difficult to draw conclusions regarding the coating adhesion strength of the differently textured samples.

Finally, dielectric measurements of the textured samples revealed slightly leaky cigar-shaped polarization loops, with low values for maximum polarization, but not the ferroelectric response expected for a $BaTiO_3$-coating. The lack of ferroelectricity was explained by the small grain size of the films, which is known to suppress ferroelectricity. As the piezoelectric properties of the coatings are essential for their final applications, more work should be carried out to improve the coating quality with regards to this.

7 Further work

Due to the outbreak of the CoViD-19 pandemic, and its following strict restrictions, it was not possible to carry out neither nanoindentation tests, nanoscratch tests, nor proper EDS-mapping of the substrate-coating interface in the FIB. Future work should therefore firstly focus on getting more accurate measures of the coating adhesion and strength by carrying out nanoindentation and nanoscratch tests, and on doing more accurate EDS-mapping to get a more complete understanding of the reactions happening at the substrate-coating interface. For the elemental analysis, test methods such as Wavelength-Dispersive X-Ray Spectroscopy (WDX), Glow Discharge Optical Emission Spectrometry (GD-OES), Secondary Ion Mass Spectrometry (SIMS), and Atom Probe Tomography (APT) should also be considered. The latter three of these processes are destructive, meaning that they permanently harm the surface, but they can be used to get a better overview of which elements are present, at which levels of concentration, and at which depth regions.

Furthermore, more detailed experiments should be carried out in terms of temperature programs and sequences, in order to achieve coatings with high crystallinity, while at the same time keeping the substrate oxidation sufficiently low. This Master's thesis' focus has been to keep the temperatures as low as possible, only testing up to a maximum temperature of 700 °C for a maximum of 6 min dwell time, so new studies should focus on temperatures and dwell times above this. Additionally, during this Master's thesis and its preceding project work [1], only atmospheres of N_2-gas and air were tested. The former was quickly eliminated, as an additional reoxidation step was needed, and that the resulting product consisted of multiple nitrogen-containing secondary phases. However, it would have been interesting to investigate how an initial thermal processing step in e.g. argon, followed by a reoxidation step in air, affected the coating quality. Argon, being a noble gas, should not produce any undesired secondary phases, neither should it cause substantial oxidation of the substrate, and upon reoxidation, the coating layers would have been expected to protect the substrate. Thus, this might be an even better way of making these BT-coatings on Ti6Al4V-substrates than what was done in this Master's thesis. It would also be interesting to investigate factors such as precursor solution concentration and spinning rate, and how they affect the coating of textured substrates. Also, as some planarization of the substrate texture was observed, it would be interesting to look into factors preventing this, in order to retain more of the substrate surface texture. For this, solutions with higher viscosity, and a more advanced curing system, perhaps with curing starting in the spin-down phase of the process, should be investigated.

When the coating procedure has been optimized in terms of adhesion, crystallinity and substrate oxidation, tests mimicking the human body conditions should be carried out. This includes immersion testing to ensure that the coating can withstand its intended environment, in addition to testing of both cyclic and static mechanical load strength, to ensure that the coating can endure the stresses developed when used as a bone implant. Finally, in vitro cell testing should be done, which makes it possible to see if the piezoelectric properties of the coating actually enhance bone growth. Additionally, this test would reveal whether there is a direct relationship between surface roughness and cell growth, or if this is more dependent on the surface texture itself, and not the roughness value.

During the ferroelectric testing of coatings, dark brown/black spots were observed at some of the electrodes for some of the samples. However, when re-measured several weeks later, no such spots appeared, and all attempts on reproducing the results were failed. These spots, and their seemingly strange behaviour, could not be properly explained by the author of this Master's thesis, nor by any others that were contacted regarding this. It would therefore be highly interesting to do more research into this phenomenon, in order to understand its causes. This would in turn lead to a better insight in the chemical and electrical reactions happening in the layered structure, which can be used when selecting and designing other piezoelectric systems. During the discussions on these spots, it was found that the contacts between the different layers of the system were Ohmic, meaning that charge injection can happen readily. It should therefore be considered to apply a thin layer of a different material, with a work function that resulted in the development of a Schottky barrier, between the BT layer and the oxide layer. In that way, charge injection can be prevented, and the piezoelectric properties of the samples might be better retained. Additionally, as the measurements carried out with gold electrodes resulted in far from ideal hysteresis loops, electrodes of e.g. Pt should be tested, and possibly also with the interdigitated electrode setup as described by Ræder et al. [16]. Finally, in order to get an even more accurate impression of the piezoelectric properties of the coating, more advanced piezoelectric testing, e.g. by piezoelectric force microscopy (PFM), should be carried out.

Bibliography

[1] M. O. H. Solum. Development of piezoeletric coatings on metal substrates for biomedical applications. Specialization project report in TMT4500, Department of Materials Science and Engineering – Norwegian University of Science and Technology, December 2019.

[2] M. Niinomi. Metallic biomaterials. *Journal of Artificial Organs*, 11(3):105, October 2008.

[3] D. F. Williams. On the nature of biomaterials. *Biomaterials*, 30(30):5897–5909, October 2009.

[4] T. Kokubo, H.-M. Kim, and M. Kawashita. Novel bioactive materials with different mechanical properties. *Focus on Biomaterials Science in Asia*, 24(13):2161–2175, June 2003.

[5] M. Cerruti, G. Magnacca, V. Bolis, and C. Morterra. Characterization of sol–gel bioglasses with the use of simple model systems: a surface-chemistry approach. *Journal of Materials Chemistry*, 13(6):1279–1286, 2003.

[6] L. L. Hench. Bioceramics. *Journal of the American Ceramic Society*, 81(7):1705–1728, July 1998.

[7] R. H. Daffner S. P. Patterson and R. A. Gallo. Electrochemical corrosion of metal implants. *Am. J. Roentgenol.*, 184(4):1219–1222, 2005.

[8] E. Ingham and J. Fisher. Biological reactions to wear debris in total joint replacement. *Proceedings of the Institution of Mechanical Engineers, Part H: Journal of Engineering in Medicine*, 214(1):21–37, 2000.

[9] G. Ryan, A. Pandit, and D. P. Apatsidis. Fabrication methods of porous metals for use in orthopaedic applications. *Biomaterials*, 27(13):2651–2670, May 2006.

[10] A. H. Rajabi, M. Jaffe, and T. L. Arinzeh. Piezoelectric materials for tissue regeneration: A review. *Acta Biomaterialia*, 24:12–23, September 2015.

[11] F. R. Baxter, C. R. Bowen, I. G. Turner, and A. C. E. Dent. Electrically Active Bioceramics: A Review of Interfacial Responses. *Annals of Biomedical Engineering*, 38(6):2079–2092, June 2010.

[12] S. R. Paital and N. B. Dahotre. Calcium phosphate coatings for bio-implant applications: Materials, performance factors, and methodologies. *Materials Science and Engineering: R: Reports*, 66(1):1–70, August 2009.

[13] J. Y. Lim and H. J. Donahue. Cell Sensing and Response to Micro- and Nanostructured Surfaces Produced by Chemical and Topographic Patterning. *Tissue Engineering*, 13(8):1879–1891, June 2007.

[14] Y. Li, C. Yang, H. Zhao, S. Qu, X. Li, and Y. Li. New Developments of Ti-Based Alloys for Biomedical Applications. *Materials*, 7(3):1709–1800, March 2014.

[15] H. Kienapfel, C. Sprey, A. Wilke, and P. Griss. Implant fixation by bone ingrowth. *The Journal of Arthroplasty*, 14(3):355–368, April 1999.

[16] T. M. Raeder, K. Bakken, J. Glaum, M.-A. Einarsrud, and T. Grande. Enhanced in-plane ferroelectricity in $BaTiO_3$ thin films fabricated by aqueous chemical solution deposition. *AIP Advances*, 8(10):105228, October 2018.

[17] R. J. D. Tilley. *Understanding Solids: The Science of Materials*. John Wiley & Sons Inc, Chichester England, 2nd ed. edition, 2013.

[18] A. R. West. *Solid state chemistry and its applications*. Wiley, Chichester, 2nd ed., student ed. edition, 2014.

[19] J. Rödel, W. Jo, K. T. P. Seifert, E.-M. Anton, T. Granzow, and D. Damjanovic. Perspective on the Development of Lead-free Piezoceramics. *Journal of the American Ceramic Society*, 92(6):1153–1177, 2009.

[20] R. E. Cohen. Origin of Ferroelectricity in Perovskite Oxides. *Nature*, 358(6382):136–138, July 1992.

[21] V. M. Goldschmidt. Die Gesetze der Krystallochemie. *Naturwissenschaften*, 14(21):477–485, May 1926.

[22] J. Valasek. Piezo-Electric and Allied Phenomena in Rochelle Salt. *Physical Review*, 17(4):475–481, April 1921.

[23] S. Horiuchi and Y. Tokura. Organic ferroelectrics. *Nature Materials*, 7(5):357–366, May 2008.

[24] E. Fukada and I. Yasuda. On the Piezoelectric Effect of Bone. *Journal of the Physical Society of Japan*, 12 (10):1158–1162, 1957.

[25] E. Fukada and I. Yasuda. Piezoelectric Effects in Collagen. *Japanese Journal of Applied Physics*, 3(2):117, February 1964.

[26] H. Kawai. The Piezoelectricity of Poly(vinylidene fluoride). *Japanese Journal of Applied Physics*, 8(7):975, July 1969.

[27] E. Fukada. History and recent progress in piezoelectric polymers. *IEEE transactions on ultrasonics, ferroelectrics, and frequency control*, 47(6):1277–1290, 2000.

[28] J. Wolff. *Das Gesetz der Transformation der Knochen*. A. Hirschwald, Berlin, 1., edition, 1892.

[29] R. L. Duncan and C. H. Turner. Mechanotransduction and the functional response of bone to mechanical strain. *Calcified Tissue International*, 57(5):344–358, November 1995.

[30] V. I. Sikavitsas, J. S. Temenoff, and A. G. Mikos. Biomaterials and bone mechanotransduction. *Biomaterials*, 22(19):2581–2593, October 2001.

[31] R. A. Salzstein, S. R. Pollack, A. F.T. Mak, and N. Petrov. Electromechanical potentials in cortical bone—I. A continuum approach. *Journal of Biomechanics*, 20(3):261–270, January 1987.

[32] S. Weiner and H. D. Wagner. The material bone: Structure-Mechanical Function Relations. *Annual Review of Materials Science*, 28(1):271–298, August 1998.

[33] D. W. Hutmacher, J. T. Schantz, C. X. F. Lam, K. C. Tan, and T. C. Lim. State of the art and future directions of scaffold-based bone engineering from a biomaterials perspective. *Journal of Tissue Engineering and Regenerative Medicine*, 1(4):245–260, July 2007.

[34] Encyclopedia Britannica. Bone remodeling | physiology, 2010. URL `https://www.britannica.com/science/bone-remodeling`. Last retrieved 19 June 2020.

[35] M. Long and H. J. Rack. Titanium alloys in total joint replacement—a materials science perspective. *Biomaterials*, 19(18):1621–1639, 1998.

[36] T. Albrektsson, P.-I. Brånemark, H.-A. Hansson, and J. Lindström. Osseointegrated Titanium Implants:Requirements for Ensuring a Long-Lasting, Direct Bone-to-Implant Anchorage in Man. *Acta Orthopaedica Scandinavica*, 52(2):155–170, 1981.

[37] G. Wang and H. Zreiqat. Functional Coatings or Films for Hard-Tissue Applications. *Materials*, 3(7): 3994–4050, 2010.

[38] AZoM. Properties: Titanium Alloys - Ti6Al4V Grade 5, 2002. URL `https://www.azom.com/properties.aspx?ArticleID=1547`. Last retrieved 19 June 2020.

[39] C. Oldani and A. Dominguez. Titanium as a Biomaterial for Implants. In Samo K. Fokter, editor, *Recent Advances in Arthroplasty*, chapter 9. IntechOpen, January 2012.

[40] X. Li, C. Wang, W. Zhang, and Y. Li. Fabrication and characterization of porous Ti6Al4V parts for biomedical applications using electron beam melting process. *Materials Letters*, 63(3):403–405, February 2009.

[41] D. W. Richerson. *Modern Ceramic Engineering: Properties, Processing, and Use in Design*. Materials engineering. CRC Press, Boca Raton, Fla, 4th ed. edition, 2018.

[42] M. B. Smith, K. Page, T. Siegrist, P. L. Redmond, E. C. Walter, R. Seshadri, L. E. Brus, and M. L. Steigerwald. Crystal Structure and the Paraelectric-to-Ferroelectric Phase Transition of Nanoscale $BaTiO_3$. *Journal of the American Chemical Society*, 130(22):6955–6963, June 2008.

[43] M. Acosta, N. Novak, V. Rojas, S. Patel, R. Vaish, J. Koruza, G. A. Rossetti, and J. Rödel. $BaTiO_3$-based piezoelectrics: Fundamentals, current status, and perspectives. *Applied Physics Reviews*, 4(4):041305, December 2017.

[44] H. Jaffe. Piezoelectric Ceramics. *Journal of the American Ceramic Society*, 41(11):494–498, November 1958.

[45] B. Jaffe, W. R. Cook, and H. Jaffe. Chapter 5 - Barium Titanate. In *Piezoelectric Ceramics*, pages 53–114. Academic Press, January 1971.

[46] F. R. Baxter, I. G. Turner, C. R. Bowen, J. P. Gittings, and J. B. Chaudhuri. An in vitro study of electrically active hydroxyapatite-barium titanate ceramics using Saos-2 cells. *Journal of Materials Science: Materials in Medicine*, 20(8):1697–1708, August 2009.

[47] D. F. Williams. On the mechanisms of biocompatibility. *Biomaterials*, 29(20):2941–2953, July 2008.

[48] J. B. Park, A. F. Von Recum, G. H. Kenner, B. J. Kelly, W. W. Coffeen, and M. F. Grether. Piezoelectric ceramic implants: A feasibility study. *Journal of Biomedical Materials Research*, 14(3):269–277, 1980.

[49] J. B. Park, B. J. Kelly, G. H. Kenner, A. F. Von Recum, M. F. Grether, and W. W. Coffeen. Piezoelectric ceramic implants: In vivo results. *Journal of Biomedical Materials Research*, 15(1):103–110, 1981.

[50] J. Feng, Y. Huipin, and Z. Xingdong. Promotion of osteogenesis by a piezoelectric biological ceramic. *Biomaterials*, 18(23):1531–1534, December 1997.

[51] L. C. Klein. III-4 - Sol-Gel Coatings. In J. L. Vossen and W. Kern, editors, *Thin Film Processes*, pages 501–522. Academic Press, San Diego, January 1991.

[52] M. P. Pechini. Method of preparing lead and alkaline earth titanates and niobates and coating method using the same to form a capacitor, July 1967. Patent number US3330697A.

[53] T. O. L. Sunde, T. Grande, and M.-A. Einarsrud. Modified Pechini Synthesis of Oxide Powders and Thin Films. In L. Klein, M. Aparicio, and A. Jitianu, editors, *Handbook of Sol-Gel Science and Technology*, pages 1–30. Springer International Publishing, Cham, 2016.

[54] J.-D. Tsay, T.-T. Fang, T. A. Gubiotti, and J. Y. Ying. Evolution of the formation of barium titanate in the citrate process: The effect of the pH and the molar ratio of barium ion and citric acid. *Journal of Materials Science*, 33(14):3721–3727, July 1998.

[55] G. Cao and Y. Wang. *Nanostructures and Nanomaterials*, volume Volume 2. World Scientific, January 2011.

[56] D. B. Hall, P. Underhill, and J. M. Torkelson. Spin coating of thin and ultrathin polymer films. *Polymer Engineering & Science*, 38(12):2039–2045, 1998.

[57] R. W. Schwartz, T. Schneller, and R. Waser. Chemical solution deposition of electronic oxide films. *Comptes Rendus Chimie*, 7(5):433–461, May 2004.

[58] K. D. Budd, S. Dey, and D. A. Payne. Sol-Gel Processing of $PbTiO_3$, $PbZrO_3$, PZT, and PLZT Thin Films. *British Ceramic Proceedings*, 36:107–121, 01 1985.

[59] C. D. E. Lakeman and D. A. Payne. Processing Effects in the Sol-Gel Preparation of PZT Dried Gels, Powders, and Ferroelectric Thin-Layers. *Journal of the American Ceramic Society*, 75(11):3091–3096, November 1992.

[60] Y. L. Tu, M. L. Calzada, N. J. Phillips, and S. J. Milne. Synthesis and electrical characterization of thin films of PT and PZT made from a diol-based sol-gel route. *Journal of the American Ceramic Society*, 79 (2):441–448, February 1996.

[61] M. N. Kamalasanan, S. Chandra, P. C. Joshi, and A. Mansingh. Structural and optical properties of sol-gel-processed $BaTiO_3$ ferroelectric thin films. *Applied Physics Letters*, 59(27):3547–3549, December 1991.

[62] T. Hayashi, N. Oji, and H. Maiwa. Film Thickness Dependence of Dielectric Properties of $BaTiO_3$ Thin Films Prepared by Sol-Gel Method. *Japanese Journal of Applied Physics*, 33(Part 1, No. 9B):5277–5280, September 1994.

[63] K. Bakken. *In situ Characterization of Ferroelectric Oxide Thin Films during Aqueous Chemical Solution Deposition*. NTNU, 2020.

[64] F. F. Craig. *The reservoir engineering aspects of waterflooding*, volume vol. 3 of *Henry L. Doherty series*. Henry L. Doherty Memorial Fund of AIME, New York, 1971.

[65] B. Feng, J. Weng, B. C. Yang, J. Y. Chen, J. Z. Zhao, L. He, S. K. Qi, and X. D. Zhang. Surface characterization of titanium and adsorption of bovine serum albumin. *Materials Characterization*, 49(2):129–137, September 2002.

[66] S. Frangini, A. Mignone, and F. de Riccardis. Various aspects of the air oxidation behaviour of a Ti6Al4V alloy at temperatures in the range 600–700 °C. *Journal of Materials Science*, 29(3):714–720, February 1994.

[67] N. Lin, P. Zhou, Y. Wang, J. Zou, Y. Ma, Z. Wang, W. Tian, X. Yao, and B. Tang. Thermal Oxidation of Ti6Al4V Alloy with Enhanced Wear and Corrosion Resistance for Oil and Gas Application: Effect of Temperature. *Surface Review and Letters*, 22(03):1550033, February 2015.

[68] Y. Luo, W. Chen, M. Tian, and S. Teng. Thermal oxidation of Ti6Al4V alloy and its biotribological properties under serum lubrication. *Tribology International*, 89:67–71, September 2015.

[69] S. Kumar, T. S. N. S. Narayanan, S. G. S. Raman, and S. K. Seshadri. Thermal oxidation of Ti6Al4V alloy: Microstructural and electrochemical characterization. *Materials Chemistry and Physics*, 119(1):337–346, January 2010.

[70] V. Ischenko, J. Woltersdorf, E. Pippel, R. Köferstein, and H.-P. Abicht. Formation of metastable calcite-type barium carbonate during low-temperature decomposition of (Ba,Ti)-precursor complexes. *Solid State Sciences*, 9(3):303–309, March 2007.

[71] V. Ischenko, E. Pippel, R. Köferstein, H.-P. Abicht, and J. Woltersdorf. Barium titanate via thermal decomposition of Ba,Ti-precursor complexes: The nature of the intermediate phases. *Solid State Sciences*, 9(1):21–26, January 2007.

[72] M. Wei, A. J. Ruys, B. K. Milthorpe, C. C. Sorrell, and J. H. Evans. Electrophoretic Deposition of Hydroxyapatite Coatings on Metal Substrates: A Nanoparticulate Dual-Coating Approach. *Journal of Sol-Gel Science and Technology; New York*, 21(1-2):39–48, June 2001.

[73] D. M. Mattox. *Handbook of Physical Vapor Deposition (PVD) Processing*. Elsevier Science, 2007.

[74] J. W. Hutchinson, M. D. Thouless, and E. G. Liniger. Growth and configurational stability of circular, buckling-driven film delaminations. *Acta Metallurgica et Materialia*, 40(2):295–308, February 1992.

[75] H.-H. Yu, M. Y. He, and J. W. Hutchinson. Edge effects in thin film delamination. *Acta Materialia*, 49(1): 93–107, January 2001.

[76] H. H. Yu and J. W. Hutchinson. Influence of substrate compliance on buckling delamination of thin films. *International Journal of Fracture*, 113(1):39–55, January 2002.

[77] W. Xu, W. Hu, M Li, and C. Wen. Sol–gel derived hydroxyapatite/titania biocoatings on titanium substrate. *Materials Letters*, 60(13):1575–1578, June 2006.

[78] B. Ben-Nissan, A. H. Choi, R. Roest, B. A. Latella, and A. Bendavid. 2 - Adhesion of hydroxyapatite on titanium medical implants. In Michael Mucalo, editor, *Hydroxyapatite (Hap) for Biomedical Applications*, Woodhead Publishing Series in Biomaterials, pages 21–51. Woodhead Publishing, January 2015.

[79] D. Buser, R. K. Schenk, S. Steinemann, J. P. Fiorellini, C. H. Fox, and H. Stich. Influence of surface characteristics on bone integration of titanium implants. A histomorphometric study in miniature pigs. *Journal of Biomedical Materials Research*, 25(7):889–902, July 1991.

[80] K. T. Bowers, J. C. Keller, B. A. Randolph, D. G. Wick, and C. M. Michaels. Optimization of surface micromorphology for enhanced osteoblast responses in vitro. *The International Journal of Oral & Maxillofacial Implants*, 7(3):302–310, 1992.

[81] J. Y. Martin, Z. Schwartz, T. W. Hummert, D. M. Schraub, J. Simpson, J. Lankford, D. D. Dean, D. L. Cochran, and B. D. Boyan. Effect of Titanium Surface-Roughness on Proliferation, Differentiation, and Protein-Synthesis of Human Osteoblast-Like Cells (mg63). *Journal of Biomedical Materials Research*, 29 (3):389–401, March 1995.

[82] D. D. Deligianni, N. Katsala, S. Ladas, D. Sotiropoulou, J. Amedee, and Y. F. Missirlis. Effect of surface roughness of the titanium alloy Ti-6Al-4V on human bone marrow cell response and on protein adsorption. *Biomaterials*, 22(11):1241–1251, June 2001.

[83] D. D. Deligianni, N. D. Katsala, P. G. Koutsoukos, and Y. F. Missirlis. Effect of surface roughness of hydroxyapatite on human bone marrow cell adhesion, proliferation, differentiation and detachment strength. *Biomaterials*, 22(1):87–96, January 2001.

[84] M. P. Groover. *Fundamentals of Modern Manufacturing: Materials, Processes, and Systems*. John Wiley & Sons, January 2010.

[85] R. N. Wenzel. Surface Roughness and Contact Angle. *Journal of Physical and Colloid Chemistry*, 53(9): 1466–1467, 1949.

[86] D. Quere. Wetting and roughness. In *Annual Review of Materials Research*, volume 38, pages 71–99. Annual Reviews, Palo Alto, 2008.

[87] A. B. D. Cassie and S. Baxter. Wettability of porous surfaces. *Transactions of the Faraday Society*, 40(0): 546–551, January 1944.

[88] A. J. B. Milne and A. Amirfazli. The Cassie equation: How it is meant to be used. *Advances in Colloid and Interface Science*, 170(1-2):48–55, January 2012.

[89] B. R. Strohmeier. The effects of O_2 plasma treatments on the surface composition and wettability of cold-rolled aluminum foil. *Journal of Vacuum Science & Technology A: Vacuum, Surfaces, and Films*, 7 (6):3238–3245, November 1989.

[90] L. E. Stillwagon, R. G. Larson, and G. N. Taylor. Planarization of Substrate Topography by Spin Coating. *Journal of The Electrochemical Society*, 134(8):2030, August 1987.

[91] L. M. Peurrung and D. B. Graves. Film Thickness Profiles over Topography in Spin Coating. *Journal of The Electrochemical Society*, 138(7):2115–2124, January 1991.

[92] S. A. Gupta and R. K. Gupta. A Parametric Study of Spin Coating over Topography. *Industrial & Engineering Chemistry Research*, 37(6):2223–2227, June 1998.

[93] L.-D. Piveteau, B. Gasser, and L. Schlapbach. Evaluating mechanical adhesion of sol–gel titanium dioxide coatings containing calcium phosphate for metal implant application. *Biomaterials*, 21(21):2193–2201, November 2000.

[94] L. Le Guéhennec, A. Soueidan, P. Layrolle, and Y. Amouriq. Surface treatments of titanium dental implants for rapid osseointegration. *Dental Materials: Official Publication of the Academy of Dental Materials*, 23(7):844–854, July 2007.

[95] J. Meijer, K. Du, A. Gillner, D. Hoffmann, V. S. Kovalenko, T. Masuzawa, A. Ostendorf, R. Poprawe, and W. Schulz. Laser Machining by short and ultrashort pulses, state of the art and new opportunities in the age of the photons. *CIRP Annals*, 51(2):531–550, January 2002.

[96] Anatoliy Y. Vorobyev and Chunlei Guo. Direct femtosecond laser surface nano/microstructuring and its applications. *Laser & Photonics Reviews*, 7(3):385–407, 2013.

[97] G. Schnell, S. Staehlke, U. Duenow, J. B. Nebe, and H. Seitz. Femtosecond Laser Nano/Micro Textured Ti6Al4V Surfaces-Effect on Wetting and MG-63 Cell Adhesion. *Materials (Basel, Switzerland)*, 12(13), July 2019.

[98] G. Schnell, C. Jagow, A. Springer, M. Frank, and H. Seitz. Time-Dependent Anisotropic Wetting Behavior of Deterministic Structures of Different Strut Widths on Ti6Al4V. *Metals*, 9(9):938, September 2019.

[99] W. D. Nix. Mechanical properties of thin films. *Metallurgical Transactions A*, 20(11):2217, November 1989.

[100] D. R. Mumm, A. G. Evans, and I. T. Spitsberg. Characterization of a cyclic displacement instability for a thermally grown oxide in a thermal barrier system. *Acta Materialia*, 49(12):2329–2340, July 2001.

[101] G. Liu, Q. Lei, M. A. Wolak, Q. Li, L.-Q. Chen, C. Winkler, J. Sloppy, M. L. Taheri, and X. Xi. Epitaxial strain and its relaxation at the $LaAlO_3/SrTiO_3$ interface. *Journal of Applied Physics*, 120(8):085302, August 2016.

[102] A. A Volinsky, N. R Moody, and W. W Gerberich. Interfacial toughness measurements for thin films on substrates. *Acta Materialia*, 50(3):441–466, February 2002.

[103] P. S. Alexopoulos and T. C. O'Sullivan. Mechanical Properties of Thin Films. *Annual Review of Materials Science*, 20(1):391–420, 1990.

[104] M. C. Kuo and S. K. Yen. The process of electrochemical deposited hydroxyapatite coatings on biomedical titanium at room temperature. *Materials Science & Engineering C-Biomimetic and Supramolecular Systems*, 20(1-2):153–160, May 2002.

[105] X. Nie, A. Leyland, and A. Matthews. Deposition of layered bioceramic hydroxyapatite/TiO_2 coatings on titanium alloys using a hybrid technique of micro-arc oxidation and electrophoresis. *Surface and Coatings Technology*, 125(1):407–414, March 2000.

[106] B. D. Beake, A. J. Harris, and T. W. Liskiewicz. Review of recent progress in nanoscratch testing. *Tribology - Materials, Surfaces & Interfaces*, 7(2):87–96, June 2013.

[107] T. G. Nieh, A. F. Jankowski, and J. Koike. Processing and characterization of hydroxyapatite coatings on titanium produced by magnetron sputtering. *Journal of Materials Research*, 16(11):3238–3245, November 2001.

[108] A. Dey, A. K. Mukhopadhyay, S. Gangadharan, M. K. Sinha, and D. Basu. Characterization of Microplasma Sprayed Hydroxyapatite Coating. *Journal of Thermal Spray Technology*, 18(4):578–592, December 2009.

[109] I. Jouanny, S. Labdi, P. Aubert, C. Buscema, O. Maciejak, M. H. Berger, V. Guipont, and M. Jeandin. Structural and mechanical properties of titanium oxide thin films for biomedical application. *Thin Solid Films*, 518(12):3212–3217, April 2010.

[110] W. C. Oliver and G. M. Pharr. An improved technique for determining hardness and elastic modulus using load and displacement sensing indentation experiments. *Journal of Materials Research*, 7(6):1564–1583, June 1992.

[111] J. Musil and M. Jirout. Toughness of hard nanostructured ceramic thin films. *Surface and Coatings Technology*, 201(9):5148–5152, February 2007.

[112] G. Perumal, M. Geetha, R. Asokamani, and N. Alagumurthi. Wear studies on plasma sprayed Al2O3–40wt% 8YSZ composite ceramic coating on Ti–6Al–4V alloy used for biomedical applications. *Wear*, 311(1):101–113, March 2014.

[113] L. Qian, M. Li, Z. Zhou, H. Yang, and X. Shi. Comparison of nano-indentation hardness to microhardness. *Surface and Coatings Technology*, 195(2):264–271, May 2005.

[114] B.-D. Hahn, J.-M. Lee, D.-S. Park, J.-J. Choi, J. Ryu, W.-H. Yoon, B.-K. Lee, D.-S. Shin, and H.-E. Kim. Mechanical and in vitro biological performances of hydroxyapatite–carbon nanotube composite coatings deposited on Ti by aerosol deposition. *Acta Biomaterialia*, 5(8):3205–3214, October 2009.

[115] Y. Fan, K. Duan, and R. Wang. A composite coating by electrolysis-induced collagen self-assembly and calcium phosphate mineralization. *Biomaterials*, 26(14):1623–1632, May 2005.

[116] Q. Zhang, S. Corkovic, C. P. Shaw, Z. Huang, and R. W. Whatmore. Effect of porosity on the ferroelectric properties of sol–gel prepared lead zirconate titanate thin films. *Thin Solid Films*, 488(1):258–264, September 2005.

[117] V. Stancu, M. Lisca, I. Boerasu, L. Pintilie, and M. Kosec. Effects of porosity on ferroelectric properties of $Pb(Zr_{0.2}Ti_{0.8})O_3$ films. *Thin Solid Films*, 515(16):6557–6561, June 2007.

[118] Q. M. Zhang, Haisheng Xu, Fei Fang, Z.-Y. Cheng, Feng Xia, and H. You. Critical thickness of crystallization and discontinuous change in ferroelectric behavior with thickness in ferroelectric polymer thin films. *Journal of Applied Physics*, 89(5):2613–2616, February 2001.

[119] R. Thomas, S. Mochizuki, T. Mihara, and T. Ishida. Influence of Sputtering and Annealing Conditions on the Structure and Ferroelectric Properties of $Pb(Zr,Ti)O_3$ Thin Films Prepared by RF Magnetron Sputtering. *Japanese Journal of Applied Physics*, 40:5511, August 2001.

[120] S. M. Sze. *Physics of semiconductor devices*. Wiley-Interscience, Hoboken, N.J, 3rd ed. edition, 2007.

[121] Robert F. Pierret. *Semiconductor device fundamentals*. Addison-Wesley, Reading, Mass, 1996.

[122] D. Stanescu, H. Magnan, B. Sarpi, M. Rioult, T. Aghavnian, J.-B. Moussy, C. L. Rountree, and A. Barbier. Electrostriction, Electroresistance, and Electromigration in Epitaxial $BaTiO_3$-Based Heterostructures: Role of Interfaces and Electric Poling. *ACS Applied Nano Materials*, 2(6):3556–3569, June 2019.

[123] K.-I. Park, S. Xu, Y. Liu, G.-T. Hwang, S.-J. L. Kang, Z. L. Wang, and K. J. Lee. Piezoelectric $BaTiO_3$ Thin Film Nanogenerator on Plastic Substrates. *Nano Letters*, 10(12):4939–4943, December 2010.

[124] C.-G. Duan, S. S. Jaswal, and E. Y. Tsymbal. Predicted Magnetoelectric Effect in $Fe/BaTiO_3$ Multilayers: Ferroelectric Control of Magnetism. *Physical Review Letters*, 97(4):047201, July 2006.

[125] D. Liu. Insulation Resistance Degradation in Ni-$BaTiO_3$ Multilayer Ceramic Capacitors. *IEEE Transactions on Components Packaging and Manufacturing Technology*, 5(1), January 2015.

[126] K. Abe, S. Komatsu, N. Yanase, K. Sano, and T. Kawakubo. Asymmetric Ferroelectricity and Anomalous Current Conduction in Heteroepitaxial $BaTiO_3$ Thin Films. *Japanese Journal of Applied Physics*, 36(9S): 5846, September 1997.

[127] M. Stengel, D. Vanderbilt, and N. A. Spaldin. Enhancement of ferroelectricity at metal–oxide interfaces. *Nature Materials*, 8(5):392–397, May 2009.

[128] Y. A. Park, K. D. Sung, C. J. Won, J. H. Jung, and N. Hur. Bipolar resistance switching and photocurrent in a $BaTiO_{3-\delta}$ thin film. *Journal of Applied Physics*, 114(9):094101, September 2013.

[129] K. Kaemmer, H. Huetz, B. Holzapfel, W. Haessler, and L. Schultz. Electrode influence on the polarization properties of $BaTiO_3$ thin films prepared by off-axis laser deposition. *Journal of Physics D-Applied Physics*, 30(4):522–526, February 1997.

[130] J. Lienig and M. Thiele. Fundamentals of Electromigration. In *Fundamentals of Electromigration-Aware Integrated Circuit Design*, pages 13–60. Springer International Publishing, Cham, 2018.

[131] D. G. Pierce and P. G. Brusius. Electromigration: A review. *Microelectronics Reliability*, 37(7):1053–1072, July 1997.

[132] S. J. Krumbein. Metallic electromigration phenomena. *IEEE Transactions on Components, Hybrids, and Manufacturing Technology*, 11(1):5–15, March 1988.

[133] G. Y. Yang, G. D. Lian, E. C. Dickey, C. A. Randall, D. E. Barber, P. Pinceloup, M. A. Henderson, R. A. Hill, J. J. Beeson, and D. J. Skamser. Oxygen nonstoichiometry and dielectric evolution of $BaTiO_3$. Part II—insulation resistance degradation under applied dc bias. *Journal of Applied Physics*, 96(12): 7500–7508, December 2004.

[134] C. A. Randall, R. Maier, W. Qu, K. Kobayashi, K. Morita, Y. Mizuno, N. Inoue, and T. Oguni. Improved reliability predictions in high permittivity dielectric oxide capacitors under high dc electric fields with oxygen vacancy induced electromigration. *Journal of Applied Physics*, 113(1):014101, January 2013.

[135] A. Sarkar and G. G. Khan. The formation and detection techniques of oxygen vacancies in titanium oxide-based nanostructures. *Nanoscale*, 11(8):3414–3444, February 2019.

[136] Q. Wu, Q. Zheng, and R. van de Krol. Creating Oxygen Vacancies as a Novel Strategy To Form Tetrahedrally Coordinated Ti^{4+} in Fe/TiO_2 Nanoparticles. *The Journal of Physical Chemistry C*, 116(12): 7219–7226, March 2012.

[137] M. Martínez-Calderon, A. Rodríguez, A. Dias-Ponte, M. C. Morant-Miñana, M. Gómez-Aranzadi, and S. M. Olaizola. Femtosecond laser fabrication of highly hydrophobic stainless steel surface with hierarchical structures fabricated by combining ordered microstructures and LIPSS. *Applied Surface Science*, 374:81–89, June 2016.

[138] C.-J. Yang, X.-S. Mei, Y.-L. Tian, D.-W. Zhang, Y. Li, and X.-P. Liu. Modification of wettability property of titanium by laser texturing. *The International Journal of Advanced Manufacturing Technology*, 87(5): 1663–1670, November 2016.

[139] B. Wu, M. Zhou, J. Li, X. Ye, G. Li, and L. Cai. Superhydrophobic surfaces fabricated by microstructuring of stainless steel using a femtosecond laser. *Applied Surface Science*, 256(1):61–66, October 2009.

[140] D. Murakami, H. Jinnai, and A. Takahara. Wetting Transition from the Cassie–Baxter State to the Wenzel State on Textured Polymer Surfaces. *Langmuir*, 30(8):2061–2067, March 2014.

[141] P. Papadopoulos, L. Mammen, X. Deng, D. Vollmer, and H.-J. Butt. How superhydrophobicity breaks down. *Proceedings of the National Academy of Sciences of the United States of America*, 110(9):3254–3258, February 2013.

[142] I. Badge, A. Y. Stark, E. L. Paoloni, P. H. Niewiarowski, and A. Dhinojwala. The Role of Surface Chemistry in Adhesion and Wetting of Gecko Toe Pads. *Scientific Reports*, 4, October 2014.

[143] Y.-Y. Chen, J.-G. Duh, and B.-S. Chiou. The effect of substrate surface roughness on the wettability of Sn-Bi solders. *Journal of Materials Science: Materials in Electronics*, 11(4):279–283, June 2000.

[144] C. J. Howard, T. M. Sabine, and F. Dickson. Structural and thermal parameters for rutile and anatase. *Acta Crystallographica Section B*, pages 462–468, August 1991.

[145] C. Yu, S. Zhu, D. Wei, and F. Wang. Amorphous sol–gel SiO2 film for protection of Ti6al4v alloy against high temperature oxidation. *Surface and Coatings Technology*, 201(12):5967–5972, 2007.

[146] A. Paul, T. Laurila, V. Vuorinen, and S. V. Divinski. *Thermodynamics, Diffusion and the Kirkendall Effect in Solids*. Springer International Publishing : Imprint: Springer, Cham, 1st ed. 2014. edition, 2014.

[147] K. K. Poon. *Development of Piezoelectric BCZT Ceramics as Electroactive Bone Implant Material*. NTNU, 2020.

[148] D.-F. Mo, T.-F. Song, Y.-J. Fang, X.-S. Jiang, C. Q. Luo, M. D. Simpson, and Z.-P. Luo. A Review on Diffusion Bonding between Titanium Alloys and Stainless Steels. *Advances in Materials Science and Engineering*, September 2018.

[149] A.-A. El Mel, R. Nakamura, and C. Bittencourt. The Kirkendall effect and nanoscience: hollow nanospheres and nanotubes. *Beilstein Journal of Nanotechnology*, 6(1):1348–1361, June 2015.

[150] F. Zhang, G. Baralia, A. Boborodea, C. Bailly, B. Nysten, and A. M. Jonas. Partial Dewetting of Polyethylene Thin Films on Rough Silicon Dioxide Surfaces. *Langmuir*, 21(16):7427–7432, August 2005.

[151] J. Chen and S. J. Bull. Approaches to investigate delamination and interfacial toughness in coated systems: an overview. *Journal of Physics D: Applied Physics*, 44(3):34001, January 2011.

[152] N. Lin, Q. Liu, J. Zou, D. Li, S. Yuan, Z. Wang, and B. Tang. Surface damage mitigation of Ti6Al4V alloy via thermal oxidation for oil and gas exploitation application: characterization of the microstructure and evaluation of the surface performance. *RSC Advances*, 7(22):13517–13535, 2017.

[153] X. Chen, L. Liu, and F. Huang. Black titanium dioxide (TiO_2) nanomaterials. *Chemical Society Reviews*, 44(7):1861–1885, March 2015.

[154] T. Close, G. Tulsyan, C. A. Diaz, S. J. Weinstein, and C. Richter. Reversible oxygen scavenging at room temperature using electrochemically reduced titanium oxide nanotubes. *Nature Nanotechnology*, 10(5): 418–422, May 2015.

[155] F. Teng, M. Li, C. Gao, G. Zhang, P. Zhang, Y. Wang, L. Chen, and E. Xie. Preparation of black TiO_2 by hydrogen plasma assisted chemical vapor deposition and its photocatalytic activity. *Applied Catalysis B: Environmental*, 148-149:339–343, April 2014.

[156] O. Carp, C. L. Huisman, and A. Reller. Photoinduced reactivity of titanium dioxide. *Progress in Solid State Chemistry*, 32(1):33–177, January 2004.

[157] W.-G. Kim and S.-W. Rhee. Effect of the top electrode material on the resistive switching of TiO_2 thin film. *Microelectronic Engineering*, 87(2):98–103, February 2010.

[158] B. J. Choi, D. S. Jeong, S. K. Kim, C. Rohde, S. Choi, J. H. Oh, H. J. Kim, C. S. Hwang, K. Szot, R. Waser, B. Reichenberg, and S. Tiedke. Resistive switching mechanism of TiO_2 thin films grown by atomic-layer deposition. *Journal of Applied Physics*, 98(3):033715, August 2005.

[159] E. Dorjpalam, M. Takahashi, Y. Tokuda, and T. Yoko. Controlling carrier density and its effect on I–V characteristics of the anatase–TiO_2 thin films prepared by a sputter deposition method. *Thin Solid Films*, 483(1):147–151, July 2005.

[160] M. V. Raymond and D. M. Smyth. Defects and charge transport in perovskite ferroelectrics. *Journal of Physics and Chemistry of Solids*, 57(10):1507–1511, October 1996.

[161] M. Liu, H. Zhu, Y. Zhang, C. Xue, and J. Ouyang. Energy Storage Characteristics of $BiFeO_3/BaTiO_3$ Bi-Layers Integrated on Si. *Materials*, 9(11), November 2016.

[162] T. J. Zhang, R. K. Pan, Z. J. Ma, M. G. Duan, D. F. Wang, and M. He. Large rectifying leakage current in $Pt/BaTiO_3/Nb:SrTiO_3/Pt$ structure. *Applied Physics Letters*, 99(18):182106, October 2011.

[163] J. Gu, M. D. Bullwinkel, and G. A. Campbell. Spin Coating on Substrate with Topography. *Journal of The Electrochemical Society*, 142(3):907, March 1995.

[164] C. F. Holder and R. E. Schaak. Tutorial on Powder X-ray Diffraction for Characterizing Nanoscale Materials. *ACS Nano*, 13(7):7359–7365, July 2019.

[165] R. Jagdheesh, M. Diaz, S. Marimuthu, and J. L. Ocaña. Chemical analysis on laser processed Ultrahydrophobic Ti-6Al-4V surface by high vacuum Process. *Data in Brief*, 22:954–959, February 2019.

[166] R. Jagdheesh, M. Diaz, S. Marimuthu, and J. L. Ocaña. Hybrid laser and vacuum process for rapid ultrahydrophobic Ti-6Al-4V surface formation. *Applied Surface Science*, 471:759–766, March 2019.

[167] D. Huerta-Murillo, A. García-Girón, J. M. Romano, J. T. Cardoso, F. Cordovilla, M. Walker, S. S. Dimov, and J. L. Ocaña. Wettability modification of laser-fabricated hierarchical surface structures in Ti-6Al-4V titanium alloy. *Applied Surface Science*, 463:838–846, January 2019.

[168] M. Dutta, S. Mridha, and D. Basak. Effect of sol concentration on the properties of ZnO thin films prepared by sol–gel technique. *Applied Surface Science*, 254(9):2743–2747, February 2008.

[169] H. C. F. Martens, R. Vlutters, and J. C. Prangsma. Thickness dependent crystallization speed in thin phase change layers used for optical recording. *Journal of Applied Physics*, 95(8):3977–3983, March 2004.

[170] V. Ion, F. Craciun, N. D. Scarisoreanu, A. Moldovan, A. Andrei, R. Birjega, C. Ghica, F. Di Pietrantonio, D. Cannata, M. Benetti, and M. Dinescu. Impact of thickness variation on structural, dielectric and piezoelectric properties of (Ba,Ca)(Ti,Zr)O_3 epitaxial thin films. *Scientific Reports*, 8(1):2056, December 2018.

[171] K.-W. Lee, Y.-I. Kim, and W.-J. Lee. Physical Modeling of the Effect of the Asymmetric Electrode Configuration on the Hysteresis Curves of Ferroelectric Film Capacitors. *Ferroelectrics*, 271(1):179–185, January 2002.

[172] Y. Umeno, J. M. Albina, B. Meyer, and C. Elsässer. Ab initio calculations of ferroelectric instability in $PbTiO_3$ capacitors with symmetric and asymmetric electrode layers. *Physical Review B*, 80(20):205122, November 2009.

[173] F. Liu, I. Fina, R. Bertacco, and J. Fontcuberta. Unravelling and controlling hidden imprint fields in ferroelectric capacitors. *Scientific Reports*, 6(1):25028, April 2016.

Appendix

A Area surface roughness measurements

Table A.1 shows the measured surface area roughness vales for the uncoated, textured samples produced by Hermann Seitz' Microfluidics group at the University of Rostock, Germany. Additionally, Table A.2 shows the corresponding values for the coated, textured samples. The values were found using an Alicona InfiniteFocus microscope, using a 50X magnifying objective lens. In order to obtain the values, 3D data sets of the surface topography in a 408x408 µm square were collected in a focus range of ± 40 µm from the point where the sample surface was in focus.

Table A.1: Measured surface area roughness, *Sa* of uncoated, textured samples: Reference (R), Grid (G), LIPSS (L), LIPSS & Grid (LG).

	$\mathbf{Sa_R}$[nm]	$\mathbf{Sa_G}$[nm]	$\mathbf{Sa_L}$[nm]	$\mathbf{Sa_{LG}}$[nm]
#1	118.0	3459.2	94.9	3149.1
#2	192.9	3464.2	87.4	3144.2
#3	175.4	3455.2	95.8	3176.0
#4	274.4	3599.2	89.8	3156.2
Average	190.2	3494.5	92.0	3156.4
Standard deviation	56.0	60.6	34.9	12.1

Table A.2: Measured surface area roughness, *Sa* of coated, textured samples: Reference (R), Grid (G), LIPSS (L), LIPSS & Grid (LG).

	$\mathbf{Sa_R}$[nm]	$\mathbf{Sa_G}$[nm]	$\mathbf{Sa_L}$[nm]	$\mathbf{Sa_{LG}}$[nm]
#1	105.8	3129.1	215.0	3115.3
#2	97.8	3081.9	97.4	3039.2
#3	98.9	3060.4	136.4	3054.3
Average	100.8	3090.4	149.6	3069.6
Standard deviation	3.5	28.7	48.9	32.9

B Contact angle measurements

The contact angle measurements carried out on the uncoated textured samples before plasma cleaning are shown in Tables B.1, B.2, B.3, B.4, for the reference sample (R), the Grid-textured sample (G), the LIPSS-textured sample (L), and the LIPSS & Grid-textured sample (LG), respectively. These measurements were carried out with a Krüss DSA100 Drop Shape Analyzer, and a 5 µL drop of distilled water was deposited with a deposition rate of $1\,\mu L\,s^{-1}$ for each test. The contact angle was determined 4 s after drop deposition, and the samples were patted dry with a light-duty tissue wiper and placed in a sample box for 20 min before the next drop deposition. In total 5 drops were deposited on different positions on each sample, one in the middle (#1), one towards the top (#2), one towards the left (#3), one towards the bottom (#4), and one towards the right (#5) of the sample. Tables B.5, B.6, B.7, B.8, show the corresponding values for the same samples after plasma cleaning.

Before plasma cleaning

Table B.1: Measured contact angles on a reference sample (R) before plasma cleaning.

	$\theta_{\mathbf{R-1}}[^\circ]$	$\theta_{\mathbf{R-2}}[^\circ]$	$\theta_{\mathbf{R-3}}[^\circ]$	$\theta_{\mathbf{R-4}}[^\circ]$
#1	71.0	67.1	68.4	60.7
#2	74.6	70.6	69.7	68.0
#3	76.0	69.3	71.7	72.1
#4	76.5	69.7	67.3	68.0
#5	74.0	73.6	69.9	64.7
Average	74.4	70.0	69.4	66.7
Standard deviation	1.9	2.1	1.5	3.8

Table B.2: Measured contact angles on a Grid-textured sample (G) before plasma cleaning.

	$\theta_{\mathbf{G-1}}[^\circ]$	$\theta_{\mathbf{G-2}}[^\circ]$	$\theta_{\mathbf{G-3}}[^\circ]$	$\theta_{\mathbf{G-4}}[^\circ]$
#1	101.5	107.3	110.0	110.1
#2	81.0	109.9	96.5	99.9
#3	93.3	103.8	101.0	109.8
#4	87.0	105.0	105.7	105.4
#5	103.7	112.5	106.4	120.0
Average	93.3	107.7	103.9	109.0
Standard deviation	8.5	3.2	4.7	6.6

Table B.3: Measured contact angles on a LIPSS-textured sample (L) before plasma cleaning.

	$\theta_{\mathbf{L-1}}[^\circ]$	$\theta_{\mathbf{L-2}}[^\circ]$	$\theta_{\mathbf{L-3}}[^\circ]$	$\theta_{\mathbf{L-4}}[^\circ]$
#1	92.3	85.8	95.4	59.0
#2	88.1	82.9	79.0	60.0
#3	90.7	85.0	62.0	64.7
#4	71.7	86.2	72.6	74.5
#5	87.1	79.6	84.1	67.2
Average	86.0	83.9	78.6	65.1
Standard deviation	7.4	2.4	11.2	5.6

Table B.4: Measured contact angles on a LIPSS & Grid-textured sample (LG) before plasma cleaning.

	$\theta_{\mathbf{LG-1}}[^\circ]$	$\theta_{\mathbf{LG-2}}[^\circ]$	$\theta_{\mathbf{LG-3}}[^\circ]$	$\theta_{\mathbf{LG-4}}[^\circ]$
#1	115.7	113.8	109.5	100.0
#2	110.5	99.2	90.0	81.0
#3	94.3	97.9	98.3	99.2
#4	96.3	88.3	110.9	84.2
#5	102.0	89.0	100.2	88.4
Average	103.8	97.6	101.8	90.5
Standard deviation	8.2	9.2	7.7	7.7

After plasma cleaning

Table B.5: Measured contact angles on a reference sample (R) after plasma cleaning.

	$\theta_{\mathbf{R-1}}[^\circ]$	$\theta_{\mathbf{R-2}}[^\circ]$	$\theta_{\mathbf{R-3}}[^\circ]$	$\theta_{\mathbf{R-4}}[^\circ]$
#1	60.5	62.0	59.0	39.5
#2	63.3	60.2	55.2	66.4
#3	63.9	63.7	59.3	70.7
#4	69.6	63.7	57.5	67.6
#5	62.8	64.0	54.3	71.0
Average	64.0	62.7	57.0	63.0
Standard deviation	3.0	1.5	2.0	11.9

Table B.6: Measured contact angles on a Grid-textured sample (G) after plasma cleaning.

	$\theta_{\mathbf{G-1}}[^\circ]$	$\theta_{\mathbf{G-2}}[^\circ]$	$\theta_{\mathbf{G-3}}[^\circ]$	$\theta_{\mathbf{G-4}}[^\circ]$
#1	82.8	68.4	75.5	78.3
#2	85.6	61.7	56.3	55.0
#3	77.4	82.1	61.4	66.4
#4	86.8	70.0	68.2	66.6
#5	76.1	93.3	83.2	72.3
Average	81.7	75.1	68.9	67.7
Standard deviation	4.3	11.2	9.6	7.7

Table B.7: Measured contact angles on a LIPSS-textured sample (L) after plasma cleaning.

	$\theta_{\mathbf{L-1}}[^\circ]$	$\theta_{\mathbf{L-2}}[^\circ]$	$\theta_{\mathbf{L-3}}[^\circ]$	$\theta_{\mathbf{L-4}}[^\circ]$
#1	64.4	38.5	41.3	57.8
#2	59.4	52.7	71.6	53.6
#3	64.2	67.3	71.1	66.7
#4	81.3	72.8	68.3	55.1
#5	76.7	77.9	73.3	80.0
Average	69.2	61.8	65.1	62.6
Standard deviation	8.3	14.4	12.0	9.8

Table B.8: Measured contact angles on a LIPSS & Grid-textured sample (LG) after plasma cleaning.

	$\theta_{\mathbf{LG-1}}[^\circ]$	$\theta_{\mathbf{LG-2}}[^\circ]$	$\theta_{\mathbf{LG-3}}[^\circ]$	$\theta_{\mathbf{LG-4}}[^\circ]$
#1	37.1	49.3	70.8	73.5
#2	59.4	44.6	65.0	92.5
#3	51.0	61.3	84.1	99.3
#4	71.5	72.6	73.4	97.8
#5	59.0	55.6	75.0	105.5
Average	55.6	56.7	73.7	93.7
Standard deviation	11.3	9.7	6.2	10.9

C Energy-dispersive X-ray Spectroscopy

The results of the EDS line-scans carried out in the colored frames in Figure C.1 are shown in Figures C.2 and C.3. These measurements were carried out with a Zeiss Supra 55VP LVFESEM instrument, with instrumental parameters as shown in Table C.1.

Table C.1: Parameters for the EDS analysis of the coating-substrate interface.

Parameter	Value
Acceleration voltage	10 kV
Tilt angle	48°
Frames (scan repeats)	32
Resolution	27 nm
Dwell time	200 s

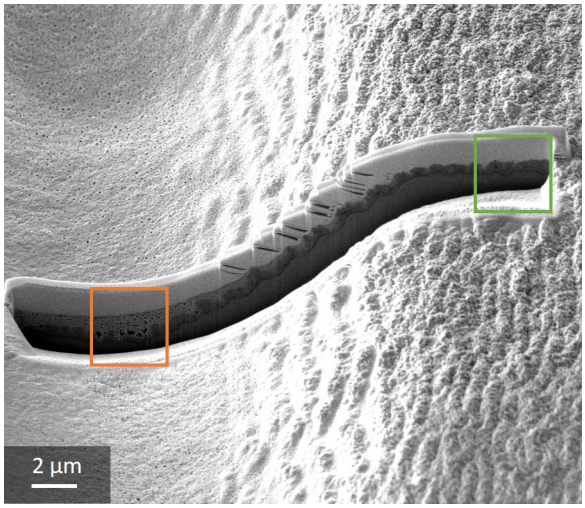

Figure C.1: Overview of a grid-valley of sample LG-3, where the colored boxes indicate positions where EDS line scans were performed.

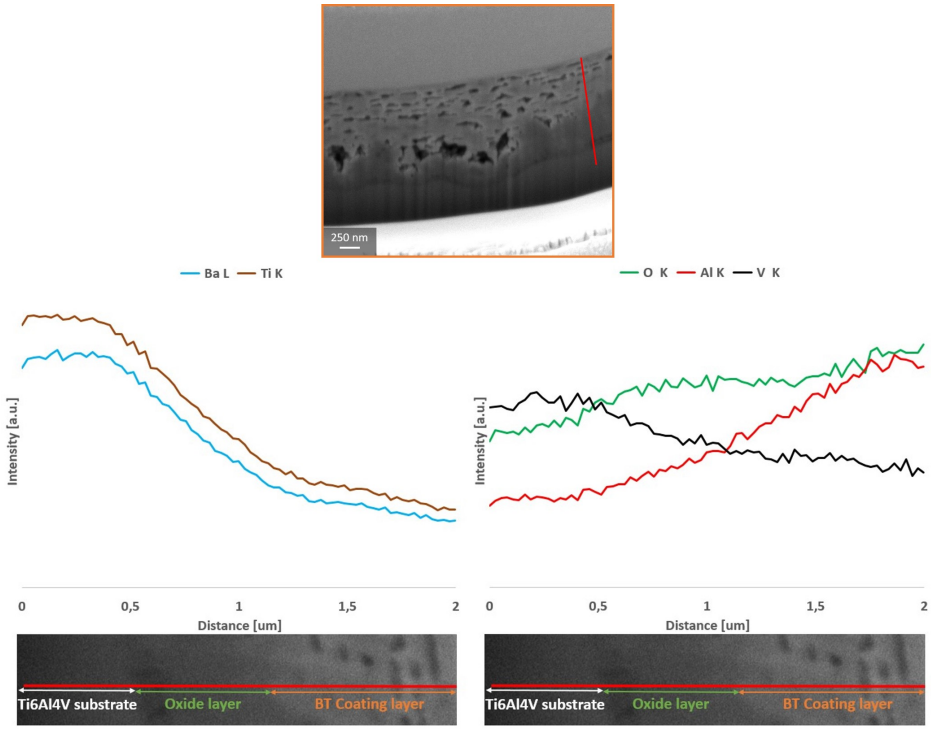

Figure C.2: Results of EDS line scan in the bottom of a grid-valley on sample LG-3, along the indicated red line inside the colored frame. Note that scales of the y-axes on the plots are different, with the intensities of Ba and Ti far greater than those of O, Al, and V.

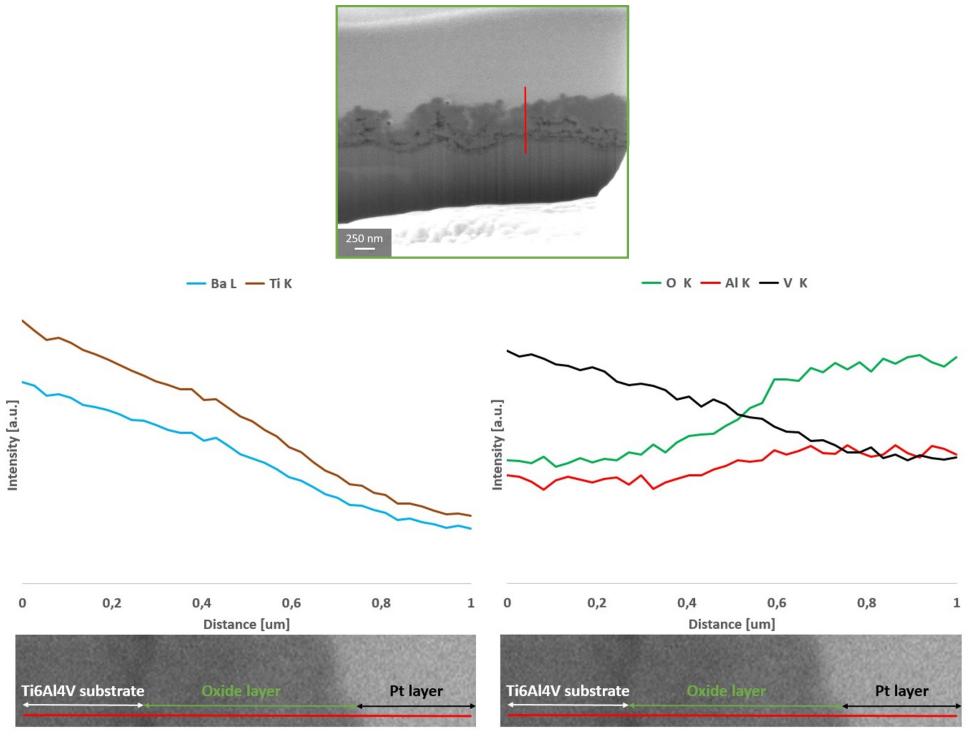

Figure C.3: Results of EDS line scan at the top of a grid-valley on sample LG-3, along the indicated red line inside the colored frame. Note that scales of the y-axes on the plots are different, with the intensities of Ba and Ti far greater than those of O, Al, and V.

Marcus Oskar Heggen Solum

Development of piezoelectric coatings on metal substrates for biomedical applications

NTNU
Norwegian University of
Science and Technology